Probing the structure of the extracellular matrix using gold nanoparticle based single molecule microscopy

Thesis submitted in accordance with the requirements of the University of Liverpool for the degree of Doctor in Philosophy

By

Daniel James Nieves

September 2013

«Quid refert,» inquit «procures, qua scilicet arte

Quoque modo tacitae pateant enigmata sortis?»

Alexandreis, Liber II

Declaration

I hereby declare that the work contained within this thesis is my own and has not been submitted for any other degree at any University. The work of other is acknowledged as appropriate. Ruoyan Xu, Changye Sun and Yong Li from the University of Liverpool provided fibroblast growth factor proteins used throughout the thesis. Nina Azmi, University of Liverpool, provided Maleimide functionalised heparin-derived oligosaccharides used in Chapter 4. Yassir Ahmed, from the University Liverpool, provided the other oligosaccharides used in Chapter 5. Bahram Ibrahimi (University of Liverpool) provided the MDCK cells used in Chapter 5.

Acknowledgements

I would like to extend my thanks and gratitude to those who have helped me both in terms of guidance and advice, but also support and friendship.

Firstly, I would like to express my sincere thanks to both Prof. Dave Fernig and Dr. Raphäel Lévy as the work here would not have been possible without their knowledge and experience. They have provided great support in my pursuit of this PhD, and have also been kind enough to offer advice on matters that extend further than the confines of academia. I would also like to thank them for a considerable contribution to a two hundred dollar bar tab run up in Chijmes, Singapore, that if unpaid may have seriously hampered me leaving the bar.

I would also like to thank the dozens of people who I have met and worked with during my time at Liverpool, especially those in Lab D. Without their friendship this experience would not have been as enjoyable. They too have offered a variety of useful advice during the much more informal 'lab meetings' held on Friday evenings.

Finally, I would like to thank those who have supported me much longer than the duration of the PhD, namely my parents, Gillian and Jose. They have given me all the support that I have required throughout my life and I hope that this goes someway to paying back their faith.

Table of contents

Abstract ..... **vii**

List of abbreviations ..... **viii**

Chapter 1 Introduction **1**

1.1 Single molecule microscopy **1**

1.1.1 Single Particle and Single Molecule Tracking 1

1.1.2 Correlation Spectroscopy 4

1.2 An example of molecular heterogeneity: fibroblast growth factor diffusion and signalling **5**

1.2.1 FGFR 5

1.2.2 Heparan Sulphate 6

1.3 Functions of the interactions of HS with FGFs **8**

1.3.1 Activation of FGFR 8

1.3.2 Non-signalling functions of interactions with HS 10

1.3.3 Differential roles of HS in the pericellular matrix 12

1.4 Aims **13**

Chapter 2 Methods and Materials **15**

2.1 Buffers **15**

2.2 Cell culture – Rama 27 fibroblast cells **16**

2.3 Sample Chamber **16**

2.4 Nanoparticle synthesis **17**

2.4.1 Mix-Matrix Nanoparticle preparation (for 1 mL AuNPs) 17

2.4.2 G-25 chromatography: removal of excess ligand 17

2.4.3 Functionalised nanoparticles 18

2.4.4 Biotin functionalised nanoparticles 18

2.4.5 Mono-functionalised Tris-NTA nanoparticles 18

2.4.6 Mono-functional FGF-2 nanoparticles 19

2.5 Single nanoparticle standards: Sample preparation **20**

2.5.1 Poly-L-lysine immobilised nanoparticles 20

2.5.2 Streptavidin immobilised nanoparticles 20

2.5.3 Gelatin immobilized nanoparticles....20
2.6 Ligand exchange in the presence of DTT....20
2.7 UV-visible spectrometry....21
2.7.1 Calculation of the stability parameter....21
2.8 Photothermal imaging set-up....22
2.9 Characterisation of the confocal volume....23
2.10 Photothermal ACS acquisition....23
2.11 Photothermal RICS acquisition....24
2.12 Transmission electron microscopy....24
2.13 Incubation of Rama 27 cells with FGF proteins labelled with gold nanoparticles for photothermal imaging....24
2.14 Analysis of imaging and spectroscopy data....25
2.14.1 Single nanoparticle photothermal image analysis....25
2.14.2 TEM image analysis....25
2.14.3 Diameter and photothermal signal distributions....25
2.14.4 Analysis of PhACS autocorrelation spectra....26
2.14.5 Analysis of PhRICS data....26
Chapter 3 Photothermal microscopy: detecting and probing the dynamics of single gold nanoparticles....27
3.1 Optical properties of gold nanoparticles – Scattering and absorption nanolabels....28
3.2 The development of photothermal microscopy....33
3.3 Photothermal detection and imaging set-up at Liverpool....35
3.4 Photothermal imaging of single gold nanoparticles....38
3.5 Photothermally induced heating around a gold nanoparticle: Considerations of local heating for biological applications....40
3.6 Correlation Spectroscopy of gold nanoparticles....43
3.6.1 Autocorrelation Spectroscopy....45
3.6.2 Characterisation of the confocal detection volume....47
3.7 Probing the diffusion of nanoparticles in solution: Photothermal autocorrelation spectroscopy....52
3.8 Raster image correlation spectroscopy....58
3.9 Photothermal raster imaging correlation spectroscopy....63
3.10 Conclusions from Chapter 3....70

Chapter 4 Biological Stabilisation and Functionalisation of Gold Nanoparticles for Imaging Biomolecules and Probing Biological Interactions 73

4.1. Disulphide ligand shells for gold nanoparticles: A "one-step" route to imparting maleimide functionality 76

4.1.1 Synthesis and stability of the D-PEG ligand shell 81

4.1.2 Michael addition of biomolecules to maleimide and thiol functionalised D-PEG nanoparticles 84

4.1.3 "Age-related" adsorption of D-PEG nanoparticles to DEAE-Sepharose 90

4.2. Copper-free click chemistry route to maleimide functionality: Versatile labelling of biological molecules with gold nanoparticles 92

4.2.1 Stable azide functionalised gold nanoparticles: A template for copper-free click chemistry 94

4.2.2 Monovalent maleimide gold nanoparticles via copper-free click chemistry ..97

4.2.3 Conjugation of biomolecules to monovalent maleimide nanoparticles via Michael addition reactions 100

4.3. Covalent biomolecule-nanoparticle conjugates for single molecule biophysics experiments 104

4.3.1 Cell Imaging with DIBO-FGF-2 nanoparticle 104

4.4. Conclusions from Chapter 4 107

Chapter 5 Probing the organization of the extracellular matrix with FGF nanoparticle conjugates at the single molecule level 109

5.1 Binding of FGF-2 to oligosaccharides in solution: Is there evidence for cooperativity? 110

5.2 Photothermal imaging of live cells: Label-free imaging of mitochondria .. 120

5.3 Single molecule imaging of FGF-1 in the extracellular matrix of Rama 27 fibroblast cells 123

5.4 Diffusion dynamics of FGF-2 in the extracellular matrix via PhRICS 129

5.5 Conclusions from Chapter 5 135

Chapter 6 Conclusions and future perspectives 137

Appendices 145

Bibliography 146

Abstract

The observation of single biomolecules *via* optical microscopy eliminates all the implicit averaging of ensemble techniques and thereby provides access to the heterogeneity of molecular systems that will be the key to at least some biological functions. The implementation of photothermal microscopy at the University of Liverpool to achieve the detection of single gold nanoparticles over long times at high signal-to-noise-ratio is presented here, along with the development of Photothermal Raster Image Correlation Spectroscopy, PhRICS. PhRICS was shown to be equally effective as Photothermal Absorption Correlation Spectroscopy, PhACS, in the determination of the hydrodynamic diameter of colloidal gold nanoparticles in solution.

The use of gold nanoparticles as labels for biomolecules has been of great interest due to their favorable optical properties and surface chemistry. The development of a new strategy for the covalent biofunctionalisation of gold nanoparticles with a single maleimide group is described. Nanoparticles functionalised this way were used to label FGF-2 protein and heparin-derived oligosaccharides.

Both the PhRICS and the new nanoparticles developed in this thesis are combined to investigate the heterogeneity of FGF binding to heparin-derived oligosaccharides and to HS in the pericellular matrix of Rama 27 fibroblasts. The cooperativity of the interaction of FGF-2 with a dodecasaccharide is investigated. Although oligomerization of FGF-2 on the dodecasaccharide is observed, it is not cooperative. The first photothermal imaging of FGF-1 in the pericellular matrix of Rama 27 fibroblasts reveals that its diffusion is quite different from FGF-2. Imaging of FGF-2 on live cells is also revisited and probed with PhRICS. In comparison to photothermal tracking, PhRICS indicates that FGF-2 diffuses faster than first thought, and that the pericellular matrix is remodeling at timescales much shorter than previously observed.

List of abbreviations

AuNP	Gold nanoparticle
BSA	Bovine serum albumin
a.u.	Arbitrary units
ACS	Autocorrelation spectroscopy
AMPA	α-amino-3-hydroxy-5-methyl-4-isoxazolepropionic acid
AOM	Acousto optic modulator
CHO	Chinese hamster ovary cells
D-Mal NP	Nanoparticles capped with disulphide ligand shell and maleimide functional ligand
D-PEG NP	Nanoparticles capped with disulphide ligand
DEAE	Diethylaminoethanol
DIBO	Dibenzocylooctyne
DMEM	Dulbecco's modified eagle medium
DSC	Differential Scanning Calorimetry
DSF	Differential Scanning Fluorometry
DTT	Dithiothreitol
EB3	End-binding protein 3
ECM	Extracellular matrix
EG	Ethylene glycol
FBS	Fetal bovine serum
FCS	Fluorescence correlation spectroscopy
FGF	Fibroblast growth factor
FGF-NP	Nanoparticle conjugated to fibroblast growth factor protein
FGFR	Fibroblast growth factor receptor

FWHM	Full width at half maximum
GFP	Green fluorescent protein
He-Ne	Helium-Neon
HS	Heparan sulfate
HSPG	Heparan sulfate proteoglycan
MDCK	Madine-Darby canine kidney cells
mEGFP	Monomeric enhanced green fluorescent protein
MS	Mass spectrometry
NA	Numerical Aperture
NMR	Nuclear magnetic resonance
NTA	Nitrilotriacetic acid
PBS	Phosphate buffered saline
PEG	Polyethylene glycol
PhACS	Photothermal autocorrelation spectroscopy
PHI	Photothermal Heterodyne Imaging
PhRICS	Photothermal raster imaging correlation spectroscopy
PIC	Photothermal Interference Contrast
PSF	Point spread function
QD	Quantum dot
Rama 27	Rat mammary fibroblast
RI	Refractive index
RICS	Raster imaging correlation spectroscopy
SH NP	Thiol functionalised nanoparticle
SMT	Single molecule tracking
SNR	Signal-to-noise ratio
SPT	Single particle tracking

TBS	Tris Buffered Saline
TEM	Transmission electron microscopy
UV-vis	Ultraviolet-visible

1. Introduction

1.1 Single molecule microscopy

The direct observation of individual molecules by optical microscopy ("Special issue," 1999) in media as complex as living cells (Sako *et al.*, 2000; Schutz *et al.*, 2000; Harms *et al.*, 2001; Iino *et al.*, 2001; Seisenberger *et al.*, 2001) is an important development. The selection of a single molecule at a time allows the elimination of all the implicit averages of conventional optical observations. This in turn allows access to heterogeneity, dynamical fluctuations, colocalization, and conformational changes at the molecular level, all of which are critical features of molecular function. Examples where single molecule microscopy has radically changed our understanding of biological processes include the dynamics of the plasma membrane (Kusumi *et al.*, 1993; Ike *et al.*, 2003; Kusumi *et al.*, 2005; Ritchie *et al.*, 2005; Umemura *et al.*, 2008), growth factor receptors (Sako *et al.*, 2000), cell adhesion complexes (Rossier *et al.*, 2012), enzyme catalysis (Lu *et al.*, 1998), transcription (Elf *et al.*, 2007; Xie *et al.*, 2008) and morphogen gradients (Yu *et al.*, 2009; Duchesne *et al.*, 2012). Different approaches that analyse single labelled biomolecules have been developed; single particle tracking, single molecule tracking and correlation spectroscopies. Each has distinct advantages and limitations that provide different insights into a particular biological problem, which will be discussed below.

1.1.1 Single Particle and Single Molecule Tracking

Single particle tracking (SPT) yields data on the spatiotemporal position of biomolecules labelled with a particle or nanoparticle over very long times and

distances at potentially fast acquisition speeds. The tracks garnered allow access to a broad range of diffusion modes/coefficients a single molecule can experience, which can give much insight into the heterogeneity of the molecules' environment and interactions. For example, pioneering work using SPT investigated the lateral diffusion of proteins in the membrane, leading to the concept that membrane proteins are in corrals formed, in part, by the sub-plasma membrane cytoskeleton (Kusumi *et al.*, 1993; Sako & Kusumi, 1994). Labels used for such work were large and non-fluorescent, and exploited light scattering for detection. However, the drawback of such approaches was often the label itself. The requisite to generate a scattering signal greater than the cell background meant that the labels had a diameter of 40 nm or more (Sako & Kusumi, 1994), and thus would constrain the labelled molecule's movement as a result of steric interaction of the label with the environment. Moreover, the controlled functionalisation of such labels is challenging and generally leads to multivalency (i.e., several biomolecule binding sites per particle) of the particles. Thus, they will bind to more than one biomolecule, induce cross-linking, which may not only alter the movements of the conjugated biomolecule, but may also alter their activity, since oligomerisation is a major theme in molecular activation (Sako & Kusumi, 1994). In order for a single molecule experiment to be carried out strict control over the stoichiometry of label to biomolecule is absolutely required.

Over the last decade the use of gold nanoparticles as labels has yielded substantial advances in the study of single molecules. Gold nanoparticles, due to their exceptional light absorbing properties can be exploited to generate a stable optical signal due to the photothermal effect. This signal is completely stable over time, i.e., resistant to photobleaching. Coupled with this, substantial progress has been made in the stabilisation and controlled functionalisation of gold nanoparticles. Thus, the

development of ligand shells that allow stoichiometric functionalisation using a genetically encoded tag on the protein ensures that each nanoparticle corresponds to one biomolecule and that the probe cannot cross-link its target molecules. The development of photothermal microscopy overcomes some of the limitations of single particle tracking. Gold nanoparticles of sizes comparable to proteins (1.4 nm to 10 nm) can be detected by this technique. This is discussed in detail in the introductions to Chapters 3 and 4.

Single molecule tracking employs fluorescent labels that are much smaller and can be conjugated stoichiometrically to the protein of interest, such as fluorescent proteins. Fluorescent proteins, e.g., green fluorescent protein, can be genetically encoded with the protein of interest; therefore, the issue of stoichiometry is resolved. This approach has been applied to observe the diffusion and interaction of proteins in living cells; however, such labels bleach under continuous excitation. Thus, photobleaching dramatically decreases the observation time for a single molecule experiment to a maximum of ~ 10 s (often ~ 1 s) in an oxygen containing atmosphere. Progress has been made with the use of quantum dots such as CdSe/ZnS (Dahan *et al.*, 2003). They are more photostable than organic dyes and fluorescent proteins, and have proven to be valuable tools for extended observation in biological systems. The advances in gold nanoparticle stabilisation and stoichiometric functionalisation (introduced in Chapter 4) are now being extended to QDs (Wilson, PhD Thesis, University of Liverpool). However, their luminescence is subject to blinking at all time scales and they eventually go dark (Shimizu *et al.*, 2001), which renders observations of the time evolution of certain biological processes very difficult.

1.1.2 Correlation Spectroscopy

Typically, correlation spectroscopy experiments consist of the acquisition of a fluctuating signal that corresponds to molecules passing through a detection volume due to Brownian motion. Light required to excite the label is focused into the sample and the detection volume is the product of the point spread function (PSF) of that light in the imaging system, ~ λ/2. The fluctuating signal can be captured in a variety of ways, e.g., signal time trace or image, and the data are then correlated. This approach is extensively used in the field of fluorescence imaging to determine the diffusion coefficients of labelled biological molecules *in vitro* and *in vivo* (Crick *et al.*, 2006; Yu *et al.*, 2009). This has led to the development of a number of related, but not necessarily equivalent, correlation spectroscopy techniques including the most widely used; fluorescence correlation spectroscopy (FCS). Although FCS can be used to measure a wide range of diffusion speeds, it suffers from the instability of fluorescent labels, i.e., they photobleach under long periods of excitation. Thus, any relatively immobile molecules within the volume will be bleached. Therefore, either these molecules will be lost from the analysis or will bleach within the volume, thus appearing to have left the detection volume. This will lead to an inaccurate representation of the biological system, with an over representation of fast moving molecules. Moreover, FCS only samples the confocal volume. Thus, even multiple repeat measurements across, for example, a single cell, will interrogate only a fraction of the biological system. Thus, one assumption underlying this approach is that the biological system is spatially homogenous. This contrasts with the SPT and SMT approaches, which notably reveal a great deal of spatial inhomogeneity, e.g., the corral/fence explanation for inhomogeneity of membrane protein movement (Kusumi *et al.*, 1993).

Recently, equivalent methods to FCS have been developed for photothermal microscopy. Exploitation of the exceptional photostability of the photothermal signal has allowed the observation of nanoparticles, and the molecules they label, without bleaching, so giving access to slower events than FCS. Photothermal microscopy is an essential component of this thesis as described in Chapters 3 & 5 in detail. The biological context of the work is the heterogeneity of the interactions of fibroblast growth factors (FGFs) with their cell surface co-receptor heparan sulfate.

1.2 An example of molecular heterogeneity: fibroblast growth factor diffusion and signalling

The fibroblast growth factors (FGFs), their heparan sulfate (HS) co-receptor and their signalling receptor tyrosine kinases (FGFRs) form a molecular regulatory system that displays extreme heterogeneity. Since the discovery of the first FGF (Gospodarowicz, 1974), the family has expanded to include 22 different *fgf* genes encoding over 30 FGF proteins in humans (Itoh & Ornitz, 2010). The ligands are separated into different subfamilies, which are the consequence of past genome duplications followed by natural selection. The subfamilies have been shown to possess distinct, though overlapping FGFR binding specificity (Ornitz *et al.*, 1996; Zhang, 2006) and more recently, their HS binding specificity has been suggested to also follow the evolutionary relationships (i.e., division into subfamilies) of the FGFs (Xu *et al.*, 2012).

1.2.1 FGFR

The tyrosine kinase FGFR proteins, encoded by 4 genes (1 through 4), possess a common molecular architecture: three extracellular immunoglobin domains (Ig loops, numbered D1 to D3 from the N-terminal extremity to the membrane), a

transmembrane helix, and the intracellular domain, where the tyrosine kinase is situated. Alternative splicing results in over 100 receptor isoforms (Itoh & Ornitz, 2010). The main ones, from the perspective of the extracellular interactions of the FGFR, are the omission of the first Ig loop (D1) to form 2-loop receptors and the a, b, c isoforms of Ig loop III (D3). The a isoforms are not attached to the membrane; the b and c isoforms exhibit quite distinct FGF ligand binding specificity (Zhang *et al.*, 2006). For example, FGF-1 is the only "universal" ligand, as it binds to all receptor isoforms (Beenken *et al.*, 2012). In contrast, FGF-2 binds preferentially to the c isoforms of FGFR1 and FGFR2 (FGFR1c and FGFR2c). The FGF-7 subfamily has the most restricted binding specificity, with FGF-7 only binding FGFR2b and the other members of the subfamily (Ornitz *et al.*, 1996; Zhang *et al.*, 2006; Xu *et al.*, 2012).

1.2.2 Heparan Sulfate

Substantial complexity arises from the interactions of FGFs and FGFRs with other extracellular constituents, the most notable of which is the heparan sulfate (HS) co-receptor. HS is composed of sugar chains that bear a variable sulfated domain structure. The HS chain is formed from a repeating disaccharide unit (1-4 linked pyranosyluronic acid and 2-amino-2-deoxyglucopyranose residues). The initial product of biosynthesis is a polymer of glucuronic acid and N-acetyl glucosamine (Figure 1.1A) of 50-150 disaccharides (approximately 50-150 nm in length) (Esko & Lindahl, 2001; Thompson *et al.*, 2010). This polymer is then acted on sequentially by a set of modification enzymes, the first of which are the N-deacetylases/N-sulfotransferases that convert N-acetylglucosamine to N-sulfo-glucosamine. These dual action enzymes act on clusters of N-acetylglucosamines along the polysaccharide chain. The presence of N-sulfated glucosamine directs the action of the subsequent

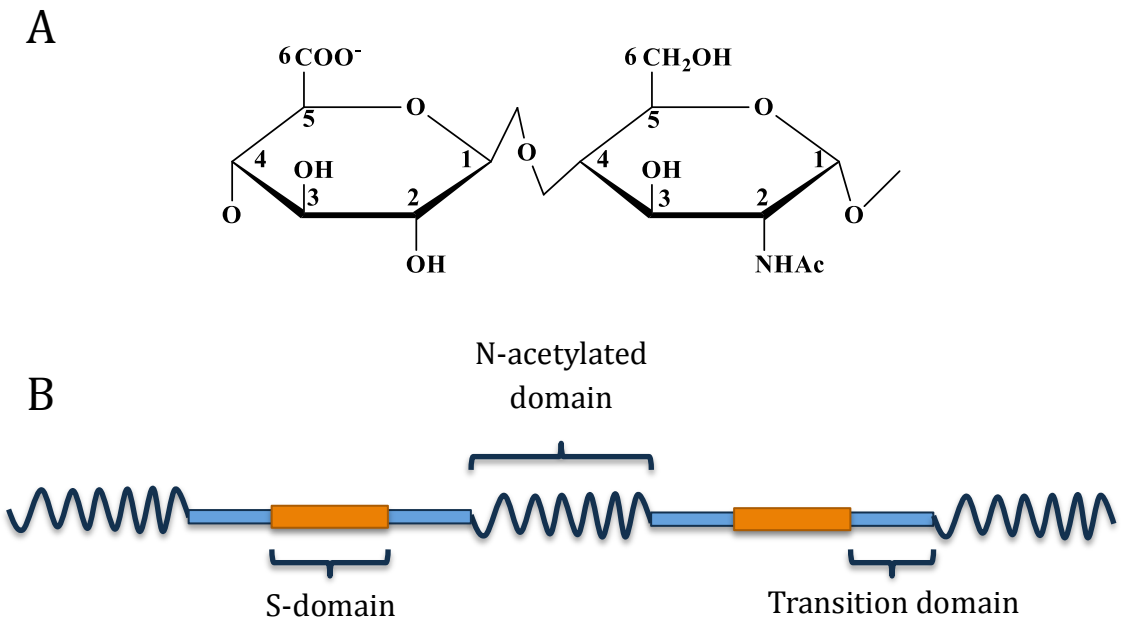

Figure 1.1. The chemical and macromolecular structure of HS. (A) Disaccharide unit of heparan sulfate comprising of D-glucuronic acid linked to N-acetyl glucosamine. (B) Representation of the modular structure of HS

modification enzymes to the glucosamine itself and neighbouring sugars. These modifications are mediated by an epimerase, which converts glucoronic acid to its epimer iduronic acid, a sugar with greater conformational versatility and O-sulphotranferases, acting on C_6 and C_3 of the glucosamine and C_2 of iduronic acid (Esko & Lindahl, 2001; Gallagher, 2001; Ori *et al.*, 2008). The end product of biosynthesis is a HS chain with characteristic domains: S-domains, in which every glucosamine is N-sulfated, flanked by transition domains where N-sulfated and N-acetylated glucosamine alternate. These regions are separated by tracts of disaccharides containing N-acetyl glucosamine and consequently, glucuronic acid (Murphy *et al.*, 2004). This domain structure is quite variable. Figures often represent chains as simple alternative units of domains (Figure 1.1B), but it is clear from the analysis of oligosaccharides isolated from HS that there is a great variety of size of each domain in at least a population of chains (Murphy *et al.*, 2004). Indeed analysis of HS from rat liver suggests an average architecture of a long initial NA domain of around 20 disaccharides and a large (~ 60% of the chain) domain that bears more resemblance to heparin than an S domain from HS (Lyon *et al.*, 1994).

1.3 Functions of the interactions of HS with FGFs

1.3.1 Activation of FGFR

Interaction of FGF with HS is essential for the formation and stabilisation of the FGF:FGFR signalling complex (Rapraeger *et al.*, 1991; Yayon *et al.*, 1991). However, binding of FGF by HS occurs when FGF ligand is not bound to FGFR, e.g., the sequestration of FGF in the extracellular matrix (Vlodavsky *et al.*, 1991). Interaction of HS with the FGFR can also occur in the absence of FGF ligand, and can lead to the stabilisation of FGFR signalling in non-canonical signalling complexes (Polanska *et al.*, 2009). It should also be noted that HS does not solely interact with

the constituents of the FGF signalling family, but has a diverse and complex interactome (Ori *et al.*, 2008; Ori *et al.*, 2011). This could mean FGF ligand and FGFR do not interact exclusively with each other when bound to HS, but that HS brings them together with other HS-dependant signalling platforms.

The stabilisation of the FGF:FGFR complex by HS gives increased signalling by FGF and has also been implicated in aiding dimerization of FGFR monomers (Ruoslahti & Yamaguchi, 1991; Guimond & Turnbull, 1999; Ornitz, 2000). At present there is no definitive model or stoichiometry for the formation of the FGF:FGFR:HS signalling complex. An early attempt to resolve the stoichiometry of the complex was made by Springer *et al. via* site-directed mutagenesis of the FGF-2 ligand and FGFR1. This revealed two FGFR binding sites in the ligand, one high affinity and the other low affinity. It was demonstrated that heparin could stabilise the lower affinity site allowing a second receptor molecule to bind and form a dimer (Pantoliano *et al.*, 1994). This model is supported by biochemical evidence, which shows that the FGF-2 dose response and certain aspects of FGFR signalling follow a bell curve (Ostrovsky *et al.*, 2002; Zhu *et al.*, 2010) and biochemical analysis of FGF-7 complexes with FGFR-2b (Sher *et al.*, 1999). Later, two different stoichiometries were proposed on the basis of co-crystal structures. One, proposed by Pellegrini *et al.*, suggested the signalling complex constitutes a heteropentameric complex (2FGF:2FGFR:heparin), referred to as the "asymmetric model". The asymmetry refers to the presence of one heparin molecule around which the complex is assembled. The heparin interacts with both FGF ligands, but only one of the receptor molecules. The flexibility of heparin plays a large part in the formation of this receptor complex, by its positioning and binding of FGF ligand, and suggests a key regulatory function, whereby heparin conformation can manipulate receptor function.

Another model for the FGF:FGFR signalling complex was derived by Schlessinger *et al.*, known as the "symmetric two-end model". The stoichiometry of the complex suggested is 2FGF:2FGFR:2heparin, and the two sugar chains run in opposite polarities such that their non-reducing ends point towards each other. Here the heparin contacts both FGF and FGFR to form a FGF:FGFR:heparin complex. The receptor dimer, and hence the 2:2:2 stoichiometry, arises from direct FGFR:FGFR contacts, augmented by heparin, allowing secondary interactions between opposing FGF ligand and FGFR. It is possible that all of the above arrangements of the FGF:FGFR:heparin signalling complex exist at any one time in solution *in vitro*, and at the cell surface (with HS) *in vivo*. In addition to the above, it has been proposed that HS does not act solely as a co-receptor, but may potentiate FGF signalling by the formation of oligomerized ligand (Ruoslahti & Yamaguchi, 1991). Such a process would allow ligand to be concentrated in proximity to signalling receptors, as oligomerization of chemokines has been observed in the presence of HS (Proudfoot *et al.*, 2003). Thus, an important question arises as to whether these complexes do indeed exist *in vivo*, and to what extent does HS govern the complexes formed.

1.3.2 Non-signalling functions of interactions with HS

There are far more binding sites on HS than there are FGFR on cells, at least where this has been measured (Fernig *et al.*, 1992; Fernig & Gallagher, 1994; Allen *et al.*, 2001; Duchesne *et al.*, 2012). Moreover, HS in the pericellular matrix can sequester and store FGFs from the culture medium, which was suggested to relate to the need for sustained (> 14 hours) signalling to trigger a cellular growth response (Flaumenhaft *et al.*, 1989; Presta *et al.*, 1989; Vlodavsky *et al.*, 1991; Fernig *et al.*, 1992). Thus, loading the pericellular matrix for 90 min with FGF-2 and then washing the cells still results in a strong growth response 18 h later. It is clear that only some

FGFs associated with the cell surface will be actively signalling, and most will be involved in interactions with just HS. One idea that emerges from the above and related work is that HS structure may be involved in the partitioning of its protein partners between different functional interactions and control their movement in the matrix (Rahmoune *et al.*, 1998).

The binding of FGF ligands by HS does not always lead a cellular response (Vlodavsky *et al.*, 1991). Sequestration of FGF ligand from the cell surface is thought to be fundamental for the processes of wound healing and blood vessel formation. This positioning of the FGF ligand, away from FGFR at the cell surface, in this case leads to the regulation of the aforementioned processes (Vlodavsky *et al.*, 1991). These stores may be mobilised by the cleavage of the HS chains to which the FGF is bound by heparanase or by cleavage of the HS proteoglycan core protein (Vlodavsky *et al.*, 1991; Polanska *et al.*, 2009). The positioning of FGF ligand is also a requirement in the formation of FGF ligand morphogen gradients (e.g., embryogenesis). The gradients, and movement of morphogen required, cannot be generated by simple diffusion alone, and, therefore, other mechanisms must be responsible (Kerszberg & Wolpert, 1998). It has been proposed that cell surface HS can influence molecular diffusion, *via* decreasing diffusion through the ECM (Lander, 1998; Lander, 2007). Such a mechanism would be concurrent with increased binding of effectors by HS. It is evident that the functions of the interaction of HS with FGFs is far more complex than just a ligand:co-receptor interaction, and that HS binding is fundamental to the positioning of FGF ligand in the ECM.

1.3.3 The differential roles of HS in the pericellular matrix

A likely constituent in all of the complexes previously mentioned is HS, and the great diversity in HS structure allows such complexes to form. The number of extracellular proteins that are known to interact with HS continues to grow (published 450 proteins, current catalogue >650 proteins, Nunes and Fernig, unpublished), and a key question is how HS is able to interact with some degree of specificity with this number of protein species of diverse function (Ori *et al.*, 2011). The interactome encompasses; growth factors (like the FGFs, bone morphogenic proteins), matrix proteins (e.g., fibronectin) and cell surface proteins (e.g., neuropilin, FGFR) (Ori *et al.*, 2011). The wealth of protein binding by HS arises from its highly variable sequence structure and the many modifications that can be made to the HS chain (Gallagher, 2001; Skidmore *et al.*, 2008b). The modifications present can affect the affinity with which HS is bound, and, therefore, facilitate protein function. The type and pattern of modifications can vary greatly from chain to chain, or domain to domain (Gallagher, 2001). Regulation of the expression of different HS structure has been observed *in vitro* (Thompson *et al.*, 2011), for example, changes in structure in response to extracellular effectors and in the course of lung development. Therefore, HS may act as a multifunctional regulator of cell surface interactions (Lander, 1998). The ability of HS sequences to allow distinct, but overlapping binding of diverse ECM proteins, coupled with inherent length and flexibility of the chain, is likely to allow to formation of most (or more) of the complexes described. This, coupled with the recent discovery that HS governs the diffusion of FGF-2 in the matrix (Duchesne *et al.*, 2012), means the role of HS does indeed involve more than the regulation of the formation of receptor complexes involved in signalling.

1.4 Aims

The aim of the thesis is to develop photothermal microscopy capable of observing single FGF proteins labelled with gold nanoparticles. The instrument must be able to detect single gold nanoparticles at high signal-to-noise ratio, and allow the implementation of photothermal imaging and related techniques, such as photothermal autocorrelation spectroscopy. These techniques will provide a platform for the investigation of FGF binding to oligosaccharides in solution in an attempt to resolve the stoichiometry of binding, and whether there is evidence for cooperativity. The observation of single FGF-1 and -2 on live cells is also a goal, and imaging coupled with correlation spectroscopy will be used to probe their movement in the extracellular matrix as a result of binding to HS. Alongside, new methods for coupling biomolecules stoichiometrically to gold nanoparticles will be explored, as the current approach uses a non-covalent interaction (Duchesne *et al.*, 2008; Duchesne *et al.*, 2012), which may in certain circumstances be prone to exchange reactions.

Chapter 1

2. Methods and Materials

2.1 BUFFERS

10xPBS (pH 7.4)

- 1.4 M NaCl
- 27 mM KCl
- 81 mM Na_2PO_4
- 12 mM KH_2PO_4

10xTBS (pH 7.6)

- 200 mM Tris base
- 1.5 M NaCl

Krebs Ringer (pH 7.4, acquisition buffer)

- 10 mM HEPES
- 140 mM NaCl
- 5 mM KCl
- 2 mM Ca_2Cl
- 2 mM MgCl
- 11 mM Glucose

100 mM Phosphate Buffer (pH 7.4)

- 22 mM $NaH_2PO_4.H_20$
- 78 mM $Na_2HPO_4.7H_20$

2.2 Cell Culture – Rama 27 fibroblast cells

Rat mammary (Rama 27) fibroblast cells were cultured on plastic in Dulbecco's modified Eagle's medium (DMEM) supplemented with 10 % (v/v) fetal calf serum, 50 ng/mL insulin, 50 ng/mL hydrocortisone and 0.05 % (v/v) sodium bicarbonate at 37°C in 10 % (v/v) CO_2 (Rudland *et al.*, 1984). When required for photothermal imaging, cells were seeded onto a rectangular coverslip (22 x 44 mm, Leica Surgipath) and left overnight. The cells were then incubated for 2 hours in step-down medium (DMEM with 250 µg/mL bovine serum albumin (BSA, Sigma Aldrich, cat no. 9048-46-8) and the used for live cell experiments.

2.3 Sample chamber

Parafilm strips (~ 2 mm in width) were placed on a rectangular coverslip (22 x 44 mm, Leica Surgipath). The coverslip was heated using a heat block (70-80°C), until the film adhered to the coverslip. A second round coverslip (22 mm ⌀, VWR Ltd.) was then placed on top of the heated film and held until the film was cool again. This method was employed in a number of ways, i.e., to generate watertight seals between coverslips, or to create capillary channels.

For mounting coverslips on both fixed and live cells, this method was amended to reduce damage and exposure of heat to the cells. Hence, the thermal sealing of the slips was achieved using the tip of a soldering iron to ensure only local heating (images of some exemplar sample chambers are presented in the Appendix A).

2.4 Nanoparticle synthesis

All functionalised and non-functionalised mix-matrix capped gold nanoparticles were prepared as described in Duchesne *et al.*, 2008.

2.4.1 Mix Matrix Nanoparticle preparation (for 1 mL AuNPs)

100 µL ligand mix (70:30; CVVVT-ol:HS-C11-EG4-OH):

- 70 µL CVVVT-ol (Peptide Protein Research Ltd., Hampshire, UK) 2 mM was obtained by mixing 35 µL CVVVT-ol (4 mM in 75:25 DMSO:ddH_2O) with 35 µL ddH_20

- 30 µL HS-C11-EG4-OH (ProChimia Surfaces Sp. z o.o., Sopot, Poland) 2 mM was obtained by mixing 6 µL HS-C11-EG_4-OH (10 mM in ethanol) with 6 µL ethanol and 18 µL ddH_20

The above ligand mix was added to 900 µL of AuNPs (usually procured from BBI solutions, Cardiff, UK) and vortex mixed.

Once mixed, 100 µL of 10xPBS Tween-20 (0.1 % v/v) was added, vortex mixed, and left to mix on a rotating wheel at room temperature overnight.

2.4.2 G-25 chromatography: removal of excess ligand

Nanoparticles were concentrated using 10 K Nanosep centrifugal filters (PALL) by centrifugation for 7 mins at 10,000 rpm. The sample was applied to a Sephadex G-25 superfine (GE Healthcare) column (column size depended on the size of the sample: column volume was 10 times or greater than the sample volume) with 1xPBS, or 200 mM NaCl when addition of $NiSO_4$ was required in the next step, as the mobile phase. The pink fraction eluting in the void volume was collected.

2.4.3 Functionalised nanoparticles

Functionalisation of nanoparticles was achieved by adding a ligand possessing an extension at its distal (to the SH group) terminus to the ligand mixture at a defined mol %. Titration of such functional ligand has been shown to provide control over the number of these ligands incorporated into the nanoparticle ligand shell (Levy *et al.*, 2006; Duchesne *et al.*, 2008). The Functional ligands used were biotin and hexahistindine (HS-CVVVT-His_6-Biotin), and Tris-NTA (HS-C16-EG3-Tris-NTA, a gift from R. Tampé, Germany).

2.4.4 Biotin functionalised nanoparticles

The peptide HS-CVVVT-His_6-biotin was included in the ligand mix at 0.5 % (mol/mol). The ligand shell was prepared as previously described (Section 2.4.1) having scaled the mix for addition of biotin peptide, and excess ligand was removed using Sephadex G-25 chromatography. Purification of biotin nanoparticles was achieved by affinity chromatography on ProBond resin (Invitrogen), which has Ni^{2+}-NTA (nitrilotriacetic acid) functional groups. One volume of resin was added for 10 volumes of particles and left for several hours on a rotary wheel. The resin was then poured into a column and washed with 10 column volumes of 1xPBS. Then, the bound particles were eluted from the column using PBS supplemented with 200 mM imidazole. The imidazole was removed from the eluted particles by buffer exchange into 1xPBS Tween-20 0.05 % (v/v) using Nanosep centrifugal filters.

2.4.5 Mono-functionalised Tris-NTA nanoparticles

The ligand Tris-NTA was included in the ligand mix at a range of 0.03 % (mol/mol) and the excess ligand removed by chromatography on Sephadex G-25 with 200 mM NaCl as the mobile phase. The nanoparticles were then incubated with 250 mM $NiSO_4$ for 2 hours at room temperature on rotary wheel; to ensure the Tris-NTA

groups were loaded with Ni^{2+} ions. Removal of excess $NiSO_4$ was achieved by Sephadex G-25 chromatography and the nanoparticles were then buffer exchanged into 1xPBS using Nanosep centrifugal filters. Titration of the number of Tris-NTA per nanoparticle and purification of mono-functionalised nanoparticles was achieved by affinity chromatography on Strep-Tactin Sepharose (IBA GmbH) functionalised with a biotinylated peptide bearing a hexa-histidine sequence (biotin-GAAHHHHHH). Nanoparticles were eluted with 200 mM imidazole in 1xPBS and then buffer exchanged into 1xPBS Tween-20 0.05 % (v/v) with Nanosep centrifugal filters.

2.4.6 Mono-functional FGF-2 nanoparticles

Mono-functional Tris-NTA nanoparticles in 1xPBS Tween-20 0.05 % (v/v) were loaded with 250 mM $NiSO_4$ for 2 hours at room temperature on a rotary wheel. The excess $NiSO_4$ was removed by Sephadex G-25 size exclusion chromatography with 200 mM NaCl as the mobile phase after which the nanoparticles were buffer exchanged into 1xPBS. The particles were then incubated with purified hexa-histidine tagged FGF-2 (a gift of Ruoyan Xu, Changye Sun and Yong Li, University of Liverpool) overnight at 4°C on a rotary wheel or for 3 hours at room temperature. The mixture was then centrifuged for 40 mins at 13000 g and 4°C. The supernatant corresponding to excess FGF-2 was removed and the particles were resuspended in 200 µL of PBS. The centrifugation was performed 4-5 times in order to remove all excess FGF-2, and the pellet was finally resuspended in 1xPBS Tween-20 0.05 % (v/v).

Functionalisation of nanoparticles with other FGFs (a gift of Ruoyan Xu, Changye Sun and Yong Li, University of Liverpool) was achieved in the same way.

2.5 Single nanoparticle standards: Sample preparation

2.5.1 Poly-L-lysine Immobilised Nanoparticles

Glass coverslips were incubated with poly-L-lysine (mw 70,000-150,000, 0.01% w/v in BioReagent, Sigma Aldrich, cat no. 25988-63-0) for 40 min and washed thoroughly thereafter with ultrapure Milli-Q water. The coverslip was then incubated with 60 pM 9.3 nm gold nanoparticles (BBI Ltd.) diluted in Milli-Q water to achieve appropriate spacing of gold nanoparticles.

2.5.2 Streptavidin Immobilised Nanoparticles

Glass coverslips were incubated with 500 µg/mL of Streptavidin (from *Streptomyces avidinii*; cat no. 9013-20-1, Sigma Aldrich) for 40 min and washed thoroughly thereafter with ultrapure Milli-Q water. The coverslip was then incubated with 120 pM of biotin functionalised gold nanoparticles diluted in 1xPBS to achieve appropriate spacing of gold nanoparticles.

2.5.3 Gelatin Immobilised Nanoparticles.

A 2 % gelatin solution (w/v in ddH_2O, Sigma Aldrich, cat no. 9000-79-8) supplemented with 0.05 % (w/v) sodium azide was diluted with a 9.3 nm AuNP solution to give a final concentration of 60 pM of gold colloid. This concentration was appropriate to generate gold nanoparticle spacing of approximately 0.036 particles/μm^3. The solution was then stored at room temperature. When required, the 2 % (w/v) gelatin solution was heated to 50°C in a water bath, and then drawn into a sample chamber *via* capillary action. The gelatin samples were used for the axial dimension confocal volume *via* a photothermal z-sweep acquisition (see Chapter 3 Section 3.6.1).

2.6 Ligand exchange in the presence of DTT

A 1 M DTT stock solution was prepared in MilliQ H_2O and kept at -20°C. The stock solution was further diluted to give concentrations required for DTT ligand exchange assays. Purified ligand capped nanoparticles (57 µL), 33 µL 10xPBS and 10 µL DTT solution at different concentrations (or ddH_2O when the required concentration of DTT was 0 mM) were added to a 384 well plate. A blank well, which only contained ddH_2O, was used as reference. All samples were in triplicate (Chen *et al.*, 2012).

2.7 UV-visible spectrometry

Absorption spectra of all nanoparticles were recorded at room temperature using a Spectra Max Plus spectrophotometer (Molecular Devices, Wokingham, UK), between 450 nm and 700 nm.

2.7.1 Calculation of the stability parameter

The surface plasmon absorption peak of 9.3 nm gold nanoparticles is around 520 nm (depending on the presence of a capping layer). When nanoparticles become aggregated, and their surface plasmons couple, a 'red shift' in the absorption spectra is seen. This can be approximated by the absorbance at 650 nm. Therefore, a stability parameter was calculated to allow different experiments to be compared. The stability parameter (SP) was defined as;

$$SP = \frac{A_{650} - A_{ref650}}{A_{520} - A_{ref520}}$$

where A_{650} and A_{520} are the absorbance of nanoparticles in different concentration of DTT at 650 nm and 520 nm respectively. The terms A_{ref650} and A_{ref520} are the absorbance of a well containing only Milli-Q water at 650 nm and 520 nm. For

comparison of the results, the calculated SP was normalized by dividing this value by the SP for ligand capped nanoparticles in 0 mM DTT (Chen *et al.*, 2012).

2.8 Photothermal imaging set-up

All images were taken using our homebuilt photothermal confocal microscope (a schematic is presented in Chapter 3 Figure 3.5). The excitation laser (523 nm; ND:YAG, Ventus Laser Quantum) is modulated at a frequency of 459.5 kHz using an acousto-optical modulator (Isomet). This heating beam was then 'cleaned' using a spatial filter. This was done to remove ellipticity generated by the modulation and generates a Gaussian beam profile. The excitation beam was then overlaid with a non-resonant probe laser (633 nm; JDSU) *via* a cold mirror (ThorLabs). The superimposed beams were focused onto the sample *via* an oil immersion objective (Zeiss Plan-Apochromat 63x, numerical aperture (NA) 1.4). The sample is placed on a piezo scanning stage (MCL502385, MadCity Labs), which allows movement of the sample in 3 dimensions (x, y, and z) over the fixed laser spot. Scanning was achieved by a piezo stage driver (MCL NanoDrive 85) under the control of the Nanonis RC4 module and Nanonis program (Specs-Zurich). The transmitted and forward scattered light was collected by a second oil objective (Zeiss Neofluar 40x, NA 1.3) and passed through a highpass filter (ThorLabs) to block the excitation laser. The red component was focused upon one photodiode of the balanced photoreceiver (Model 2107 10 MHz adjustable photoreceiver, New Focus). A lock-in amplifier (DSP 7260, Signal Recovery) was used to identify the scattered component of the probe beam that corresponds to the modulation frequency or 'beat-note' (i.e., 459.5 kHz). The signal was acquired by the Nanonis SC4 Acquisition Module (Specs-Zurich). The signal was averaged over a period of 5 ms for most imaging applications and a greyscale pixel value was generated. The values along a scan path, i.e. photothermal signal values at

each position, are then converted into a photothermal image. The images were finally saved in an .sxm format.

2.9 Characterisation of the confocal volume

The axial dimensions (x and y) of the confocal volume of the microscope, generated from the overlap of the laser beams, were measured by photothermal imaging. Images were taken of streptavidin immobilised nanoparticles (see Section 2.5.2) at the maximum photothermal signal. This maximum photothermal signal corresponded to what would be expected at the "waist" of our confocal volume. To discern the axial dimension of the confocal volume (z), a sweep in the z-axis of a 9.3 nm gold nanoparticle in gelatin was performed. This sweep measured the photothermal intensity at 50 nm intervals along the z-axis of the signal (5 ms acquisition time), with a settling time of 50 ms at each interval. The output was an intensity profile of the confocal volume in z.

2.10 Photothermal ACS acquisition

Samples were loaded into pre-prepared channel sample chambers (see Section 2.3**)** by capillary action. Work involving nanoparticles capped with a mix-matrix monolayer required the channel to be pre-incubated with 10 mg/mL BSA in 1xPBS to prevent adsorption onto the glass. The channel was subsequently washed with 1xPBS, and then the correct glycerol solution for the experiment. Once mounted onto the microscope piezo stage, the detection volume was focused approximately 5-10 μm into the solution. The signal was acquired from the Oscilloscope 2T module of the Nanonis program at a rate of 20 kHz, giving a delay time of 50 μs. Each signal was 640 ms long and taken from the Oscilloscope 2T by a custom program written in LabView 8.5 (National Instruments). Then, each acquired signal was autocorrelated by the program and kept in memory until the desired number of autocorrelation

curves was generated. The curves were averaged, to give the final autocorrelation curve used for analysis. A copy of the code for the autocorrelation spectroscopy acquisition, "ACS_3", is provided on the Appendix B CD-ROM.

2.11 Photothermal RICS acquisition

Photothermal RICS of nanoparticles in solution used the same experimental set-up as that described in Section 2.10; however, it differed in the data acquisition. The sample volume was raster scanned through the sample multiple times and the images saved. The images were typically 256 x 256 pixels with a pixel size of 50 nm (thus, the ROI was approximately 12.8 x 12.8 μm) and a pixel dwell time of 200 μs. Typically, between 20-30 images were acquired for RICS analysis. For Photothermal RICS on live cells the acquisition was largely similar, however, the detection volume was focused just 0.5 μm into the sample. For analysis, 20-50 images were acquired on live cells.

2.12 Transmission electron microscopy

Colloidal nanoparticle samples were spotted on to 200-mesh Formvar coated copper mesh grids and left to dry. The samples were digitally imaged using an FEI Tecnai G^2 120 kV transmission electron microscope in the Centre for Biomedical Electron Microscopy, University of Liverpool.

2.13 Incubation of Rama 27 cells with FGF proteins labelled with gold nanoparticles for photothermal imaging

Rama 27 cells seeded onto coverslips, as described in Section 2.1, were either incubated with FGF-NP conjugates as is (live cells), or pre-incubated with 10 mg/mL BSA in a buffer that was nine parts 1xPBS to 1 part Krebs Ringer buffer. Generally, all FGF-NP mixtures were in 10 mg/mL BSA PBS:Ringer. Further additions, such as oligosaccharides or unlabelled FGF protein, are described in the text. The

concentrations of FGF-NP used for incubation are specified for each experiment. After washing unbound FGF-NP from the cells using PBS, the cells were mounted for photothermal imaging.

2.14 Analysis of imaging and spectroscopy data

2.14.1 Single nanoparticle photothermal image analysis

Photothermal images were analysed using the Gwyddion freeware program. This allowed identification of the particle spots within the image (using the 'grains' tool) by thresholding. Signals arising from two touching/partially-overlapped nanoparticles were removed by area, i.e., approximate area photothermal peak arising from a single nanoparticle in an image with pixel size 50 nm was 80 pixels^2, and, therefore, spots above this area threshold were removed. Then the average signal for each particle was recorded. These data could then be transferred to OriginPro 8.6 for analysis of photothermal signal distributions.

2.14.2 TEM image analysis

For the sizing of nanoparticles from transmission electron micrographs ImageJ was used. The diameters where calculated using the macro PSAdev (http://code.google.com/p/psa-macro/; Appendix A). The macro calculates the maximum diameter of nanoparticles in an image and returns the data in the form of a list or histogram, which may be exported to statistical software for analysis.

2.14.3 Diameter and photothermal signal distributions

The statistical package OriginPro 8.6 was used to compile the histograms for both particle diameter and mean photothermal signal data. The histograms were fitted with a Gaussian curve *via* the fitting tool within the software. The fitting was set to carry out as many iterations of the Levenberg-Marquardt algorithm until the curve

had been fully minimized. The full width at half maximum (FWHM) of the distribution could then be determined.

2.14.4 Analysis of PhACS autocorrelation spectra

Acquired autocorrelation spectra were saved as a LabView measurement file (.lvm) and imported into OriginPro 8.6. To extract the characteristic diffusion time the spectra were normalized to a scale between 0 and 1. The normalized spectra were fitted with a single fit parameter for the characteristic diffusion time, τ_D, using Equation 3.3 (Chapter 3 Section 3.6.1) with a custom written fitting algorithm. The shape parameter, A, was fixed. The diffusion coefficient and hydrodynamic radii were subsequently calculated using Equation 3.6 (Chapter 3 Section 3.7).

2.14.5 Analysis of PhRICS data

Photothermal RICS images were first converted from .sxm to .tiff images using Gwyddion. The images were then loaded into the RICS module of the SimFCS software. Firstly, a moving average of the image sequence was taken to remove any immobile features from the images, i.e., signal that persists in at the same position throughout the image sequences. Then the moving average was subtracted from the image sequence and the spatial autocorrelation function applied. The whole surface of the resulting autocorrelation image was then fitted with fixed parameters depending on time per line, lateral dimension of the detection volume and pixel size. The program extracted the image size in pixels automatically. The fit (described in Chapter 3 Section 3.8) resulted in extraction of the diffusion coefficient for mobile features in the image.

3. Photothermal microscopy: detecting and probing the dynamics of single gold nanoparticles

The detection of gold nanoparticles *via* their photothermal signature can be exploited in a group of related, but non-equivalent, techniques, which allow gold nanoparticle labelled molecules to be probed. The localisation of single gold nanoparticles, and, therefore, labelled molecules, can be elucidated *via* the use of photothermal microscopy (Cognet *et al.*, 2003; Berciaud *et al.*, 2006; Lasne *et al.*, 2006; Duchesne *et al.*, 2012). Stoichiometry of interacting molecules may also be inferred using autocorrelation spectroscopy (ACS), as this is a method that can determine the diffusion coefficients and concentration of gold nanoparticles (Octeau *et al.*, 2009; Paulo *et al.*, 2009; Radunz *et al.*, 2009). Photothermal tracking can also be implemented, and allows the 'random walk', i.e., diffusion path, and interactions of the nanoparticle to be elucidated (Lasne *et al.,* 2006). In this chapter, the optical properties of the nanoparticles themselves, which make them amenable to photothermal detection, are discussed. Then calibration of the second homebuilt photothermal microscope at the University of Liverpool is described. The calibration ultimately leads to the detection of single gold nanoparticles at a high signal-to-noise ratio by photothermal imaging. This serves as the basis for the implementation of the related techniques mentioned above, as well as a new development: photothermal raster imaging correlation spectroscopy.

3.1 Optical properties of gold nanoparticles – Scattering and absorption nanolabels

Noble metal nanoparticles have historically been of great interest throughout the ages due to the exceptional optical properties they exhibit. Thus, such properties have ultimately made them worthy candidates for optical and plasmonic detection techniques, due to their strong interaction with light. Gold and silver nanoparticles have been the subject of much research, and exceptional control of their size and shape has been achieved. This means that very small nanoparticles, e.g., < 60 nm diameter, can be synthesised, which would be applicable to their use as an optical label (De *et al.*, 2008). However, the diameter and shape of the nanoparticles produced affects greatly the optical properties they exhibit, and hence the techniques used to image and detect them. For example, spherical gold and silver nanoparticles possess a clear single plasmon band at 520 nm and 410 nm, respectively (Doty *et al.*, 2004). For the remainder of this chapter, and the thesis, the focus will be on spherical gold nanoparticles. Here, the scattering and absorption properties of spherical nanoparticles will be discussed. Those properties underlie their detection by photothermal heterodyne imaging.

Early techniques for the detection of single molecules relied on the scattering of light with labels such as plastic beads (μm) and then large (> 40 nm) gold nanoparticles (Gelles *et al.*, 1988; Kusumi *et al.*, 1993; Sako & Kusumi, 1994). In the case of scattering labels, the interaction of the particles with light waves, known as Rayleigh scattering, occurs when the electromagnetic waves in light are scattered by particles with diameters much smaller than the wavelength of the light. The power of such single molecule analysis resulted in a gradual expansion of the field and experiments in diverse systems, including tracking latex bead labelled AMPA

receptors on neurites of cultured neurone cells (Borgdorff & Choquet, 2002). Gold nanoparticles have also been used as scattering labels; for example, ligand capped gold nanoparticles have been used to label both transferrin and alpha 2-macroglobulin receptors on normal rat kidney fibroblast cells (Sako & Kusumi, 1994). This revealed that as well as free diffusion of receptor molecules within confined "corrals" of cytoskeleton and that the restructuring of these "corral" structures was a key process in the movement of receptor molecules from compartment to compartment.

For spherical objects, such as gold nanoparticles, the amount of light scattered by a nanoparticle is characterised by Mie theory, and it decreases with the 6^{th} power of the particle radius, whereas the absorption decreases with the 3^{rd} power of the radius (Mie, 1908; Boyer *et al.*, 2002; Kelly *et al.*, 2003). At these sizes (i.e., greater than 40 nm) this scattering effect dominates over absorption ($\sigma_{scatt} > \sigma_{abs}$). Consequently, scattering techniques become less able to detect a nanoparticle as its diameter decreases (Figure 3.1). This, therefore, limits how small the gold label can be before its scattering intensity becomes too small to distinguish from that of the background (Moerner & Orrit, 1999). This restriction means that labels must have relatively large diameters, over 40 nm for gold nanoparticles. In the context of the biological environment the labels, due to their large size, are likely to perturb the movements or interactions of the molecules labelled, especially in crowded molecular environments, e.g., a synaptic or epithelial in the extracellular matrix junction, where the "head room" is of the order of nanometers to tens of nanometers, respectively. The detection of nanoparticles by scattering will also be undermined by the biological sample itself having a high scattering background; hence signal-to-noise is an issue, and so single nanoparticle detection becomes difficult.

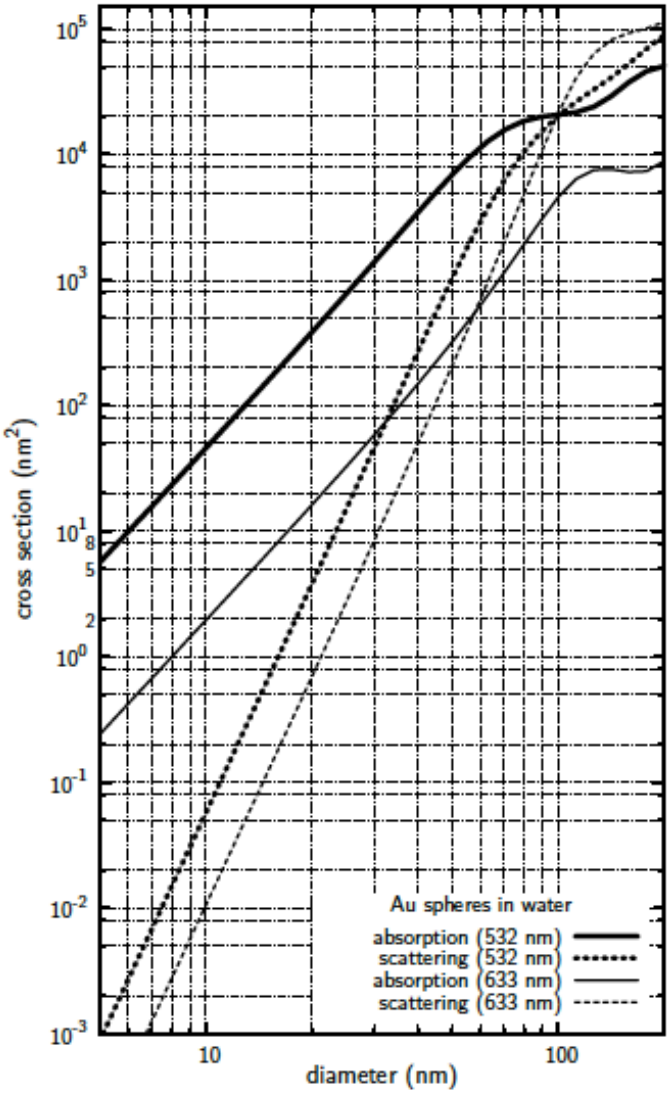

Figure 3.1 The calculated light absorption and scattering cross sections of different diameters of spherical gold nanoparticles at 532 nm and 633 nm in water (figure reproduced from Van Dijk *et al.*, 2006)

However, for the smaller gold nanoparticles, typically < 40 nm, the absorption of light begins to dominate over the scattering, i.e., $\sigma_{abs} > \sigma_{scatt}$ (Figure 3.1), as absorption only decreases with the 3rd power of the nanoparticle radius (Mie, 1908; Boyer *et al.*, 2002; Kelly *et al.*, 2003). This effect, first described by Mie in 1908, explains the characteristic red colour of colloidal gold nanoparticles. Thus, absorption of light can be exploited to detect smaller nanoparticles, as they are extremely efficient absorbers of light especially at their plasmon band (520 nm). When a focused laser beam excites a nanoparticle, light energy is converted to heat and released into the surrounding medium. The absorbed light causes a collective oscillation of the free electrons within the nanoparticle. The energy is dissipated first through the gold lattice structure and then through the immediate environment, resulting in local heating. The heat source generates a temperature gradient that decays with the inverse distance from the nanoparticle centre (d, Fig. 3.2A);

$$\Delta T(d) = \Delta T_0 \frac{R}{d} \qquad \textbf{(3.1)}$$

where the temperature increase at the surface of the nanoparticle $\Delta T_0 = P_{abs}/4\pi\kappa R$ resulting from the absorbed optical power P_{abs}, the surrounding medium's heat conductivity κ and the particle radius R. Consequently, a corresponding increase in the refractive index (RI) is generated, leading to a gradient in the surrounding medium (Figure 3.2B). This refractive index gradient has also been likened to a "thermal lens", discussed in detail by Selmke *et al*. (2012b).

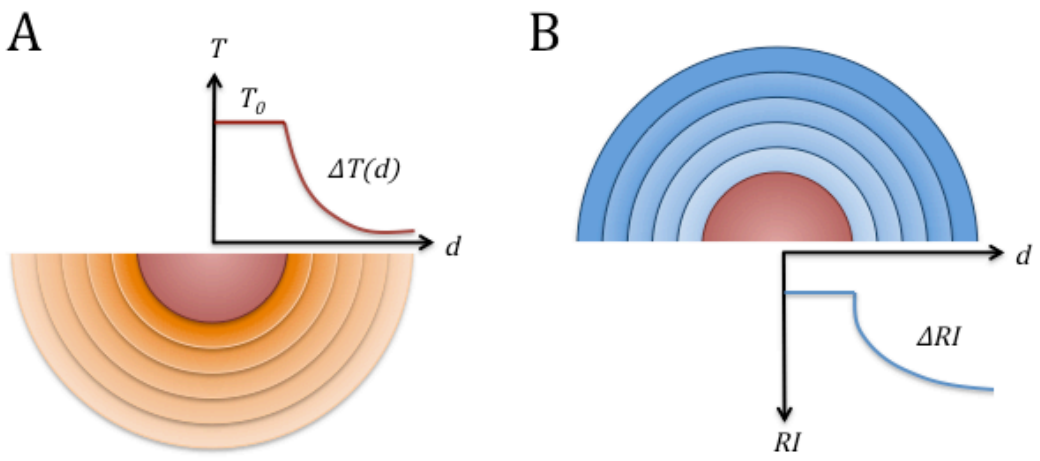

Figure 3.2 Photothermal response of a nanoparticle under excitation at the plasmon band. (A) Excitation of a nanoparticle (red) at the surface plasmon resonance leads to heat release and a change in temperature around the nanoparticle *ΔT(d)* (orange) that decreases with the inverse distance from the particle centre (*d*). (B) This leads to an increase in the refractive index (*ΔRI*; blue) of the medium immediately surrounding the medium.

These phenomena are collectively known as the photothermal effect, and have been exploited in a variety of set-ups to detect gold nanoparticles (Berciaud *et al.*, 2006; Kulzer *et al.*, 2008; Absil *et al.*, 2010). The heat release, unlike many relaxation processes (i.e., QDs and fluorescent molecules), is completely stable over time. Thus, it has been of great interest for applications of tracking and imaging of gold nanoparticles, and subsequently any biomolecules labelled by them (Lasne *et al.*, 2006; Duchesne *et al.*, 2012).

3.2 The development of photothermal microscopy

The exploitation of the photothermal signal generated when a nanoparticle is excited near its surface plasmon resonance led to the birth of the field of photothermal microscopy. During the 1990's, harnessing the photothermal effect within an optical microscope was of great interest, and towards the turn of the century it was first utilised in an optical set-up to detect non-fluorescent molecules in solution (Velinov, 1995; Tokeshi *et al.*, 2001). This was swiftly followed by the first detection of single gold nanoparticles *via* the photothermal effect, as described by Boyer *et al*. This technique was termed Photothermal Interference Contrast (PIC) and relied on the splitting of the probe beam (He-Ne laser, 633 nm), such that two laser spots were present when focused into the sample (Figure 3.3). One of the laser spots would be combined with the excitation source (532 nm; argon-ion), which was intensity modulated at frequencies from 100 kHz up to 10 MHz (Boyer *et al.*, 2002). The beams were back reflected by the sample along the same optical path and recombined with a Wollaston prism. The recombined beams were then sent onto a photodiode detector, which allowed fluctuations in the intensity of the probe beam to be detected by a lock-in amplifier referenced by the excitation modulation frequency. Scanning samples over the laser spots allowed images to be acquired, and detection of

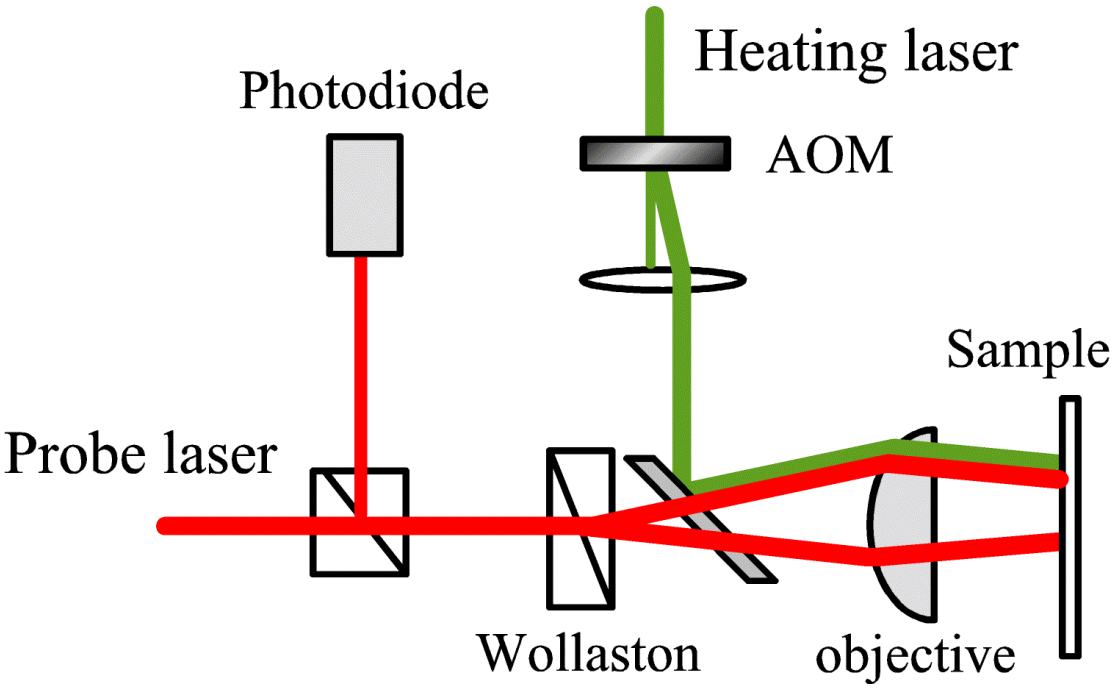

Figure 3.3 The optical set-up for PIC described in Boyer *et al*. Figure reproduced from Boyer *et al.*, 2002.

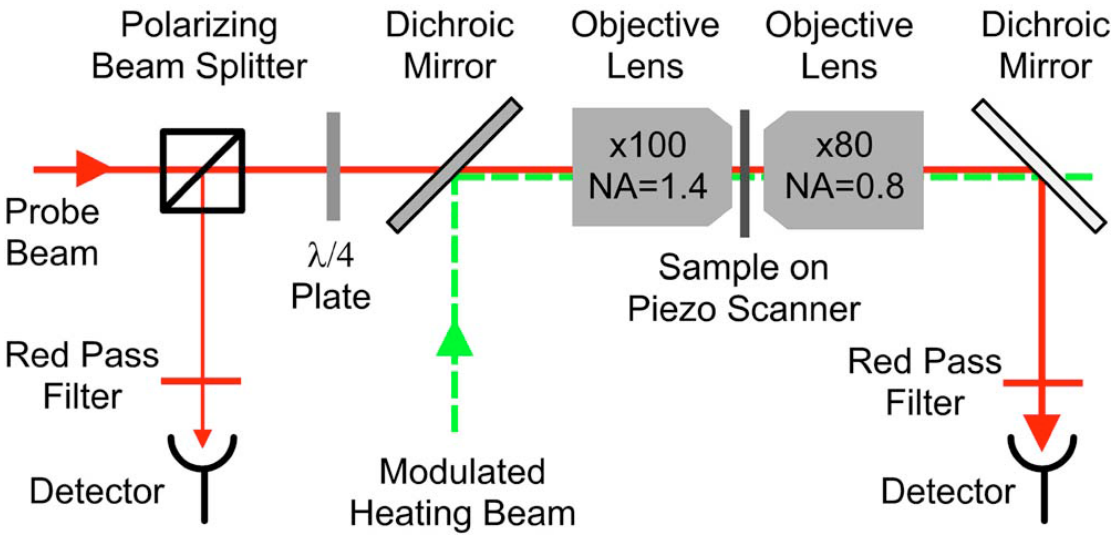

Figure 3.4 The optical set-up for PHI described in Berciaud *et al*. Figure reproduced from Berciaud *et al.*, 2006.

nanoparticles down to diameters of 5 nm was achieved, even when present in highly scattering samples (Boyer *et al.*, 2002).

Later, the same group was able to demonstrate an improved optical set-up for the photothermal detection of individual gold nanoparticles, Photothermal Heterodyne Imaging (PHI). This method combined a time modulated excitation beam with a non-resonant probe laser (Figure 3.4). Here, the scattering of the probe beam was frequency shifted due to interaction with the time-modulated change in the refractive index around a gold nanoparticle as a result of the modulation of excitation. This scattering detected by the photodiode could then be extracted using a lock-in amplifier. This technique was much more sensitive than PIC (both in the transmission and back-reflected modes), with a signal-to-noise ratio approximately two orders of magnitude higher. In turn this allowed the detection of single gold nanoparticles as small as 1.4 nm in diameter, i.e., consisting of approximately 60 gold atoms, at a relatively low heating power of 5 MW/cm^2 with a signal-to-noise ratio of 10 (Berciaud *et al.*, 2006). This optical set-up has served as the basis for the field of photothermal microscopy when attempting to detect single gold nanoparticles, and has led to the development of many techniques that exploit the exceptional signal intensity and optical stability of the nanoparticles.

3.3 Photothermal detection and imaging set-up at Liverpool

A schematic of the current photothermal microscope set-up is presented in Figure 3.5. Based around a confocal microscope the sample is excited with a 523 nm ND:YAG laser (~ 2500 kW/cm^2). This wavelength is near to the surface plasmon resonance peak of gold nanoparticles and, therefore, its absorption causes conversion of this energy to heat on the timescale of picoseconds. Subsequently, a change in the refractive index around the nanoparticle is observed; this stable signal (sometimes

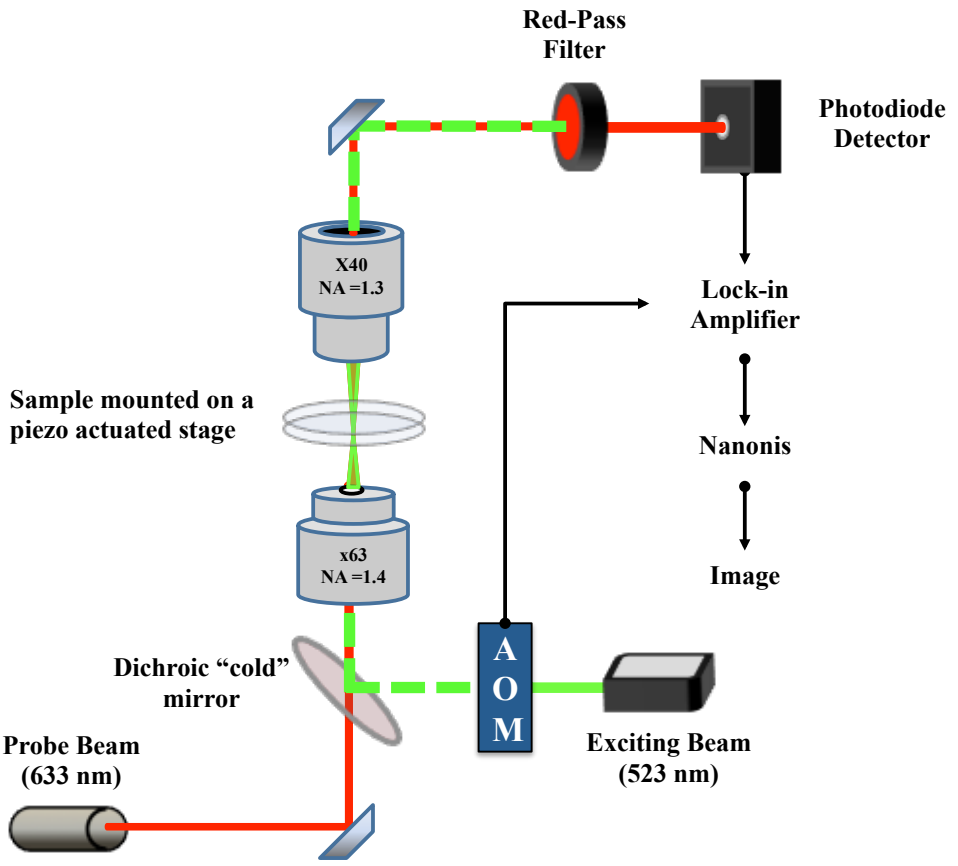

Figure 3.5 Schematic of our photothermal microscope. The excitation beam is intensity modulated using an acousto-optic modulator (AOM) and is overlaid with the non-resonant probe beam using a dichroic mirror. The overlapped beam is focused into the sample by a high numerical aperture (NA) objective and the sample is moved across the fixed laser spot using a piezo-electric scanning stage. The transmitted light from the sample is collected by a second high NA objective and, after removal or the exciting beam using a red-pass filter, is focused onto a photodiode detector. The voltage induced in the detector is filtered using a lock-in amplifier, referenced by the modulation frequency from the AOM, and the extracted signal is used to make an image by the Nanonis software.

referred to as a nano- or thermal-lens) can be exploited to detect an absorbing particle with a probe laser in the optical microscopy set-up (Boyer *et al.*, 2002; Selmke *et al.*, 2012b). Here the probe beam used is a 633 nm He-Ne laser, and is overlapped with the exciting laser using a dichroic mirror. The excitation beam is modulated at a known frequency (Ω = 490.5 kHz), which causes the frequency shift of the probe beam when a nanoparticle is detected. This frequency was chosen, as in this range the highest signal-to-noise was seen for detection of 10 nm gold nanoparticles, and has been demonstrated previously (Berciaud *et al.*, 2006). Upon detection of a particle, the modulated change in refractive index of the surrounding medium causes scattering and thus co-modulation of the probe laser beam. This probe beam is detected by a photodiode, after removal of the excitation beam by a red-pass filter. The voltage induced across the photodiode is sent to the lock-in amplifier. The photothermal signal, corresponding to the side-band or "beat-note" in the probe beam, can then be extracted. Therefore, objects that do not absorb light at 523 nm will not be detected. Similarly, only objects that do absorb at this wavelength, e.g., gold nanoparticles, will elicit a signal in this system. The signal is not only stable over time, but its intensity is proportional to the volume of gold present (Berciaud *et al.*, 2004; Berciaud *et al.*, 2006). The sample is mounted upon a piezo-electric scanning stage (MadCity Labs), and it is moved over the fixed laser spots when photothermal images are acquired. The raster scan required to acquire the images themselves is controlled by a Nanonis controller (Specs-Zurich), and the user interface allows scan speed and pixel dwell time to be adjusted accordingly. This allows, among other things, the photothermal signal within a region to be acquired, which can then be used to produce a photothermal image.

3.4 Photothermal imaging of single gold nanoparticles

An important, and obvious, first challenge with a photothermal microscope that is intended for single nanoparticle/molecule microscopy is to demonstrate that the instrument can actually detect single gold nanoparticles. A secondary, but also important, requirement is that nanoparticles can be detected at high signal-to-noise ratio (SNR) at relatively low heating laser powers. The detection of single gold nanoparticles on other photothermal microscope set-ups has been well established, as too have the imaging parameters that allow high signal to noise detection, e.g., modulation frequency, mounting medium and laser beam overlap (Berciaud *et al.*, 2006; Selmke *et al.*, 2012a; Selmke *et al.*, 2013)

A variety of single nanoparticle samples were prepared via different methods for imaging and calibration of the photothermal microscope (see Chapter 2 Section 2.5), however, this section will focus on 8.8 nm citrate stabilised gold nanoparticles (BBI Ltd.) deposited on a poly-L-lysine coated coverslip. Areas of the sample where well-spaced single nanoparticles were present were imaged using the photothermal microscope. The images acquired were typically 17.5 by 17.5 microns. Images consisted of 352 pixels by 352 pixels with an approximate pixel size just short of 50 nm. The dwell time for each pixel was 5 ms. An exemplar scan of single gold nanoparticles is presented in Figure 3.6 (left panel), with a surface plot in (right panel) to show more clearly the diffraction limited photothermal signal peak of a single nanoparticle. If the peaks within the image do indeed correspond to single gold nanoparticles, then the intensity of the peak will be proportional to the volume of the gold nanoparticles used. By comparison of the diameter distribution of the nanoparticles with the distribution of photothermal signal peak intensities, one can deduce whether single nanoparticles are detected. The intensities of 463 imaged

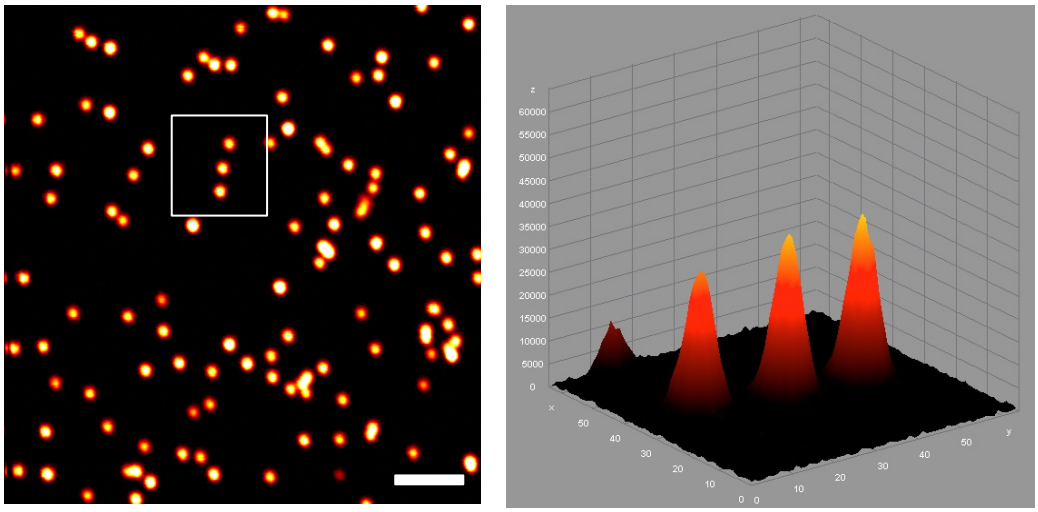

Figure 3.6 Photothermal image of 8.8 nm citrate stabilised gold nanoparticles immobilised on poly-L-lysine. Surface plot of photothermal peaks (right) within the image (white box), where x- and y- axes denote the pixel number and the z-axis is the grayscale value at that pixel. Scale bar corresponds to 5 µm.

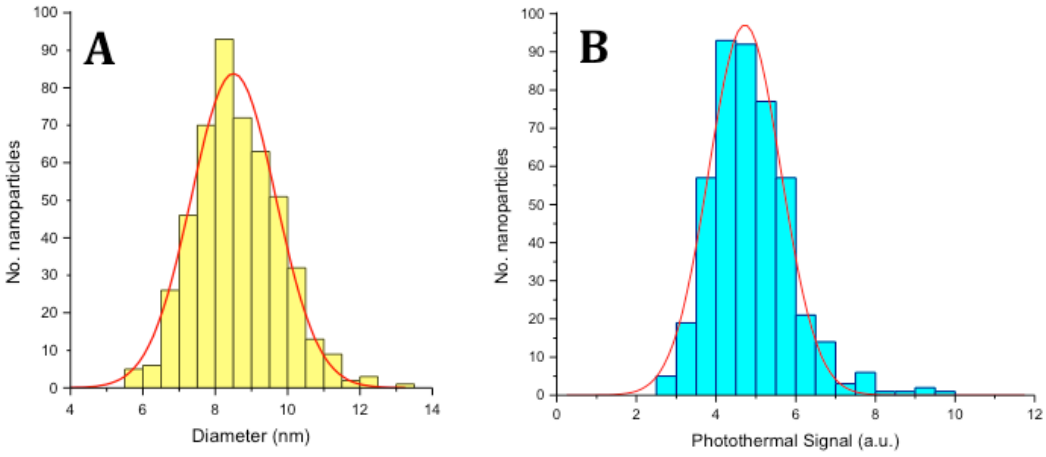

Figure 3.7 Diameter and photothermal signal intensity distributions of single gold nanoparticles. (A) The diameter of gold nanoparticles was determined by electron microscopy. (B) The same batch of nanoparticles was then imaged using photothermal microscopy and the intensity of the signal produced recorded.

photothermal peaks were extracted using Gywddion and plotted in a histogram (Figure 3.7B). The diameter of gold nanoparticles from the same batch was previously determined by transmission electron microscopy, and the diameter distribution of 451 imaged nanoparticles is presented in Figure 3.7A. Both the diameter and the photothermal signal distribution were fitted with a Gaussian curve in order to extract the full width at half maximum (FWHM) of the distribution. The first indication that the imaged photothermal peaks arise from single absorbing nanoparticles is that the distribution is monomodal. Deviation from a monomodal distribution would suggest that the sample contained polydisperse aggregates of nanoparticles spaced within the diffraction limit on the coverslip. In this instance there would be signals corresponding to an intensity of 2, 3, 4 or more nanoparticles. If single nanoparticles were indeed detected, then the FWHM of the distribution of photothermal signals will be equal to 3 times or less of the FWHM for the diameter distribution as determined by electron microscopy, as the photothermal signal depends on the volume of the nanoparticle. The FWHM for the photothermal signal distribution is approximately 45 %, whereas the for the diameter distribution it is 35 % (FWHM are represented as percentages for comparison, and are equal to the FWHM divided by the maximum value of the distribution). The FWHM of the photothermal signal distribution is 1.3 times greater than that of the diameter distribution; therefore, by virtue of being less than 3 times the width of the diameter distribution so confirming that single 8.8 nm gold nanoparticle were detected.

3.5 Photothermally induced heating around a gold nanoparticle: Considerations of local heating for biological applications

Photothermal detection is sensitive to the amount of energy absorbed by a nanoabsorber, in this case a spherical gold nanoparticle, and dissipated as heat into its

local environment. Therefore, an important consideration is how this heating will impact on the local environment of the nanoparticle, whether this is through changes in its diffusion or thermal effects on attached biomolecules. Thermal denaturation of proteins is long established and is used as a means of analysing protein function (Dill & Shortle, 1991; Uniewicz *et al.*, 2010). Heat-induced protein denaturation results from a combination of changes to the hydration of the protein (i.e., changes in the surface bound water molecules) and protein unfolding (Brovchenko *et al.*, 2005). Both effects are significantly contributed to by the increased breakage of hydrogen bonding at high temperature. Additionally, breakage of weaker bonds, such as disulfide bonds, may occur at high temperatures (well above 100°C). The result is a significant decrease in the secondary structure, exposing hydrophobic residues, thus, leading to agglomeration and aggregation of unstructured proteins (Volkin & Klibanov, 1987). FGF-2, which is the subject of much of the work carried out in Chapter 5, has been well characterized in terms of its thermal stability (Vemuri *et al.*, 1994; Uniewicz *et al.*, 2010). The melting temperature of FGF-2 is 55-59°C, depending on buffer and measurement conditions, and this has been shown to consistently increase (T_m ~ 70-90°C) when the FGF-2 binds to heparin (Vemuri *et al.*, 1994; Uniewicz *et al.*, 2010).

In order to assess if the temperature profile generated when a nanoparticle is under photothermal excitation with the current photothermal microscope set-up (Figure 3.8), Equation 3.1 was used to calculate the elevation in temperature as a function of distance from the nanoparticle centre. The exemplar temperature gradient was calculated for a gold nanoparticle with a 10 nm diameter (approximately the size of the nanoparticles used in this Thesis) in water under constant excitation (~ 2500 kW/cm^2, laser power used in this set-up) and is presented in Figure 3.8. The profile

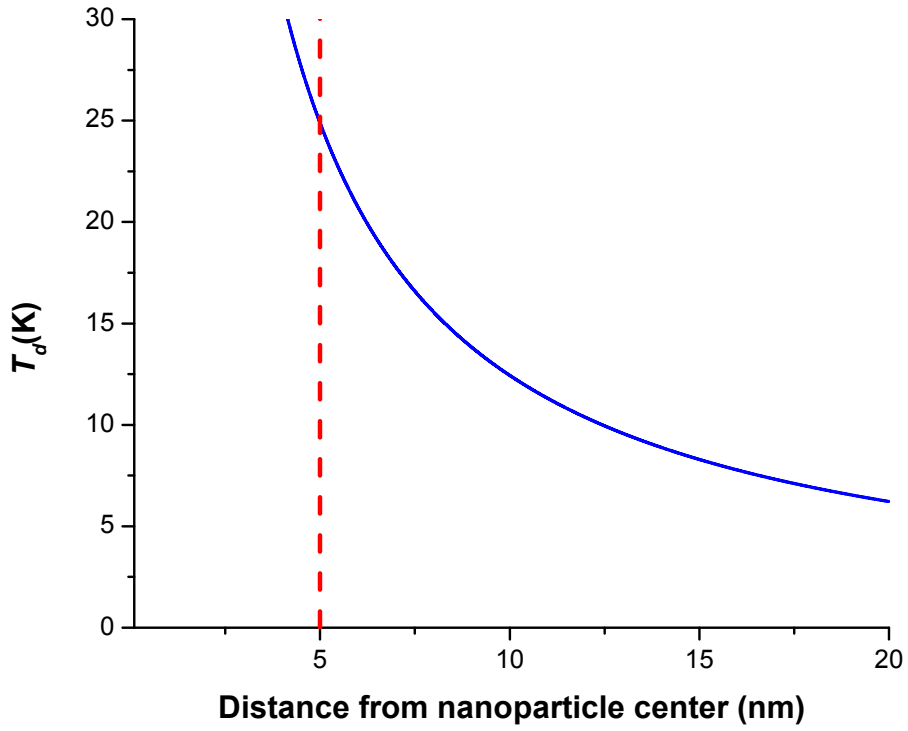

Figure 3.8 Temperature profile of a 10 nm diameter gold nanoparticle under constant photothermal excitation (2500 kW/cm^2) in water. The increase in temperature as a function of the inverse distance from the nanoparticle centre (—) was calculated using Equation 3.1 with the distance that corresponds to the nanoparticle surface indicated (---).

decreases with the inverse distance from the nanoparticle centre, and the elevation in temperature at the nanoparticle surface (5 nm, red dashed line; Figure 3.8) is 24.88 K. However, this temperature drops to 17.77 K when only 2 nm from the nanoparticle surface. Therefore, it is evident that in the current set-up that the rise in temperature around a nanoparticle is unlikely to have a significant effect on a protein attached to the nanoparticles in this Thesis (c.a. 9.8 nm diameter with a 1-2 nm ligand shell; Chapter 4). This increase is brings the overall temperature close to the melting temperature of FGF-2, however, it is pertinent to consider that the timescale of the techniques used to determine the melting temperature, i.e., DSC and DSF, tend to be from second to minutes, however, repetition of such data has been demonstrated in laser irradiation set-ups over milliseconds (Sagar *et al.*, 2013). . When performing photothermal measurements the nanoparticle is under excitation for half of the time it is observed, due to intensity modulation of the laser. Thus, it can be said that the average heat dissipation into the sample if half that when the nanoparticle is under continuous excitation, as described by the above calculations (Gaiduk *et al.*, 2010). Therefore, the average temperature experienced by the attached protein is likely to be half that calculated here. Additionally, in this Thesis, observation of nanoparticles functionalised with FGF proteins is achieved by raster scanning (Section 3.8) with dwell times on the order of milliseconds, for photothermal images, and microseconds for RICS. Thus, nanoparticles will be under observation, and thus excitation, for short times even if a nanoparticle is sampled multiple times, which is unlike a tracking experiment where the nanoparticle will be under constant observation (Duchesne *et al.*, 2012). Thus, given the melting temperature of FGF-2 protein both unbound and bound to heparin, it is unlikely that the temperatures and denaturation times required for protein unfolding will be reached in the experiments. Hence, this

heating will not significantly impact the secondary structure and, therefore, function of the protein. However, especially when experiments move to 37°C, it is something that may require adjustment in the future by the use of smaller nanoparticles or reduction of excitation laser power.

3.6 Correlation Spectroscopy of gold nanoparticles

Correlation analysis of fluctuations in a signal over time, e.g., fluorophores or nanoparticle diffusion, can yield the physical parameters that contribute to the signal fluctuation, i.e., concentration, diffusion and viscosity of the medium. This analysis is, therefore, an attractive approach when one is interested in the dynamic diffusion properties of biological molecules, as the fluctuations of labelled molecules will elucidate the diffusion properties and interactions of those molecules both in solution and on/in live cells.

Typically, correlation spectroscopy experiments consist of the acquisition of a fluctuating signal that corresponds to molecules passing through a detection volume due to Brownian motion. Light required to excite the label (plus any detection beam if it is a pump-probe experiment, e.g., photothermal microscopy) is focused into the sample and the detection volume is usually a product of the point spread function (PSF) of that light in the imaging system. The fluctuating signal can be captured in a variety of ways, e.g., a signal time trace or image, and the data are then correlated. A number of different correlation analyses can be applied depending both on the data format, but also the information one seeks to gain from the data.

The approaches described above have been routinely and extensively used in the field of fluorescence imaging to determine the diffusion coefficients of labelled biological molecules *in vitro* and *in vivo* (Crick *et al.*, 2006; Yu *et al.*, 2009). This has led to the development of a number of related, but not necessarily equivalent,

correlation spectroscopy techniques including fluorescence correlation spectroscopy (FCS) and fluorescent raster image correlation spectroscopy (RICS). More recently, taking lead from fluorescence imaging, correlation analysis has been applied to photothermal microscopy. Several investigators, almost contemporaneously, developed the technique known as photothermal autocorrelation spectroscopy, abbreviated to PhACS in this thesis (Octeau *et al.*, 2009; Paulo *et al.*, 2009). This allowed the measurement of the diffusion coefficient, and thus the hydrodynamic radii, of gold nanoparticles in solution. It was also sensitive enough to detect the presence of a capping layer, and interaction of biotin functionalised nanoparticles with streptavidin to form higher order nano-assemblies (Octeau *et al.*, 2009). In the next section, the calibration of the photothermal microscope to allow PhACS will be described. The data acquisition and fitting parameters required to perform PhACS will also be discussed. This will then serve as a tool to investigate the diffusion of gold nanoparticles in solution.

In the final section a new technique, photothermal raster image correlation spectroscopy (PhRICS), will be described. This technique will be used to probe the same samples as those probed with PhACS, as a proof of principle.

3.6.1 Autocorrelation Spectroscopy

Photothermal imaging allows the localisation of nanoparticle labelled molecules, and possibly the stoichiometry of their interactions to be determined. However, the data garnered are static, i.e., they do not elucidate the dynamic behaviour of a molecule. Biomolecules are seldom static even when associated with large-scale cell structures, such as the plasma membrane or extracellular matrix, or cell surface receptors and morphogens, and cytoskeleton for motor and intracellular signalling proteins. In the case of FGFs, their movement and positioning are key to

their signalling functions. The target cell relies on the morphogen gradient set up, in conjunction with heparan sulfate, which encodes spatio-temporal information that is then interpreted by the cell (Cohn *et al.*, 1995; Serls *et al.*, 2005; Zhu *et al.*, 2010; Duchesne *et al.*, 2012). Thus, it is essential to access information on the diffusion, positioning and concentration of FGF molecules in order to delineate how they elicit their signalling function. The photothermal set-up, discussed previously (Section 3.3), can be modified to allow access to the dynamics of nanoparticles, and their assemblies, *via* PhACS (Octeau *et al.,* 2009).

ACS can be used to probe the diffusion properties, concentration and molecular dynamics of heterogeneous molecules *in vitro*. The set-up for autocorrelation experiments is often very similar (whether the label is fluorescent or a nanoabsorber) and relies upon the passage of labelled molecules through a detection volume at a region of interest (Maiti *et al.*, 1997; Octeau *et al.*, 2009). Passage of labelled molecules through the volume generates a signal, which is correlated with itself over time (using the autocorrelation function). The normalized autocorrelation function is the product of the signal at time t and at another time point $t + \tau$, normalized by the average signal squared;

$$G_{(\tau)} = \frac{\langle \delta S(t) \delta S(t+\tau) \rangle}{\langle S(t) \rangle^2} \qquad \textbf{(3.2)}$$

where $\delta S(t)$ is the difference between the average signal value and the signal at time t, and $\langle \ \ \rangle$ denotes averaging over time. Conventionally, the observation volume is assumed to be of an elliptical Gaussian shape, due to the point spread function of the imaging system, and, therefore, values of $G_{(\tau)}$ satisfy the following equation;

$$G_{(\tau)} = \frac{1}{N\left(1 + \frac{\tau}{\tau_D}\right)\left(1 + \frac{\tau}{(A^2\tau_D)}\right)^{\frac{1}{2}}} \qquad \textbf{(3.3)}$$

where N is the average number of molecules in the observation volume, A is the shape parameter of the observation volume (corresponding quotient of the axial dimension divided by the lateral dimension), and τ_D is the characteristic diffusion time through the volume (Octeau *et al.,* 2009). The signal is acquired over time, and subsequently the autocorrelation function of that signal is calculated. This generates a curve that decays over time with the rate of decay depending on the persistence of the fluctuations within the volume, i.e., how long it takes on average for a molecule to pass through the volume. Hence, the fluctuations observed within the volume, i.e., from molecular diffusion, will be reflected in the autocorrelated data. Therefore, the autocorrelation values obtained can be fitted with Equation 3.3 to derive the diffusion parameters for molecules in this type of volume.

3.6.2 Characterisation of the confocal detection volume

The decay of the autocorrelation function when applied to molecules diffusing through a fixed detection volume relies on two factors; the diffusion coefficient of the molecule under observation and the dimensions of the detection volume. In the context of single point autocorrelation spectroscopy, the diffusion coefficient is normally the parameter being probed; therefore, accurate knowledge of the dimensions of the detection volume is essential. In the following text, characterisation of the confocal detection volume for the photothermal microscope will be described.

Previously, many methods have been used for the characterisation of confocal volumes from theoretical calculations to experimental validation. Generally the detection volume in a system is assumed to be a Gaussian prolate ellipsoid; with the two minor axes (lateral dimensions in x and y) being equal and smaller than the major axis (axial dimension in z). This shape is generated by the interaction of the focused laser beam with the optical system, and is known as the point spread function (PSF). For photothermal microscopy, the overlapping of the focused excitation and probe beam profiles generates the detection volume. The signal generated by a nanoparticle passing through the detection volume is dependent on the relative focal positions of the two beams (Selmke *et al.*, 2013). The dependence of the photothermal detection volume on the focal geometry of the pump and probe beam are discussed in detail in the literature (Selmke *et al.*, 2012b). Here, the relative focal positions of the two laser beams have been optimised so that the detection volume is as close as possible to a single ellipsoidal volume.

The most common method for determining the dimensions of a detection volume experimentally is by scanning or 'sweeping' an object that can be detected, whether this is a single nanoparticle or fluorescent bead, through the volume in the lateral (x and y) and axial (z) directions. It is worth noting that other methods to deduce the confocal volume dimensions have been used. For example, using the characteristic time it takes for an object of known diffusion coefficient to pass through the volume, thus, making it possible to extract axial and lateral dimensions, assuming the volume is a Gaussian prolate ellipsoid of the form; $x = y < z$ (Ruttinger *et al.*, 2007).

To deduce the lateral dimensions of the detection volume for our photothermal microscope, imaging of single nanoparticles was performed. The nanoparticles were

biotinylated and immobilized on streptavidin, as described in Section 2.5.2. The images used to extract the line profile of the lateral dimensions were identical to those shown in Figure 3.6. The pixel size of the images is 50 nm and the line profiles of the x and y dimension of the nanoparticle were extracted using ImageJ. Due to the nature of the image acquisition, the measurement of the x dimension is aligned with the scan direction, whereas the y measurement is perpendicular to the scan. Two exemplar profiles for the two situations are shown in Figure 3.9A and B. For the purposes of getting the best measurement of the lateral dimensions the line profiles of the imaged fitted individually with a Gaussian curve. The resulting FWHM of the fits were taken and averaged, to give a mean lateral measurement of 318.6 ± 7.8 nm (n = 47). This value is in correspondence with what would be expected for the diffraction-limited spot of the probe laser when focused (i.e., 633 nm, hence λ/2 = 316.5 nm). The measurement of the lateral dimensions of the detection volume is particularly crucial and it has been shown previously that signal fluctuations in correlation spectroscopy are dominated by objects diffusing in 2 dimensions across this lateral plane (Rigler & Mets, 1993). The FWHM of the beam profile can then be used to calculate the radius at $1/e^2$ width using the following equation;

$$2w = \frac{\sqrt{2}\,\mathrm{FWHM}}{\sqrt{\ln 2}} \qquad \textbf{(3.4)}$$

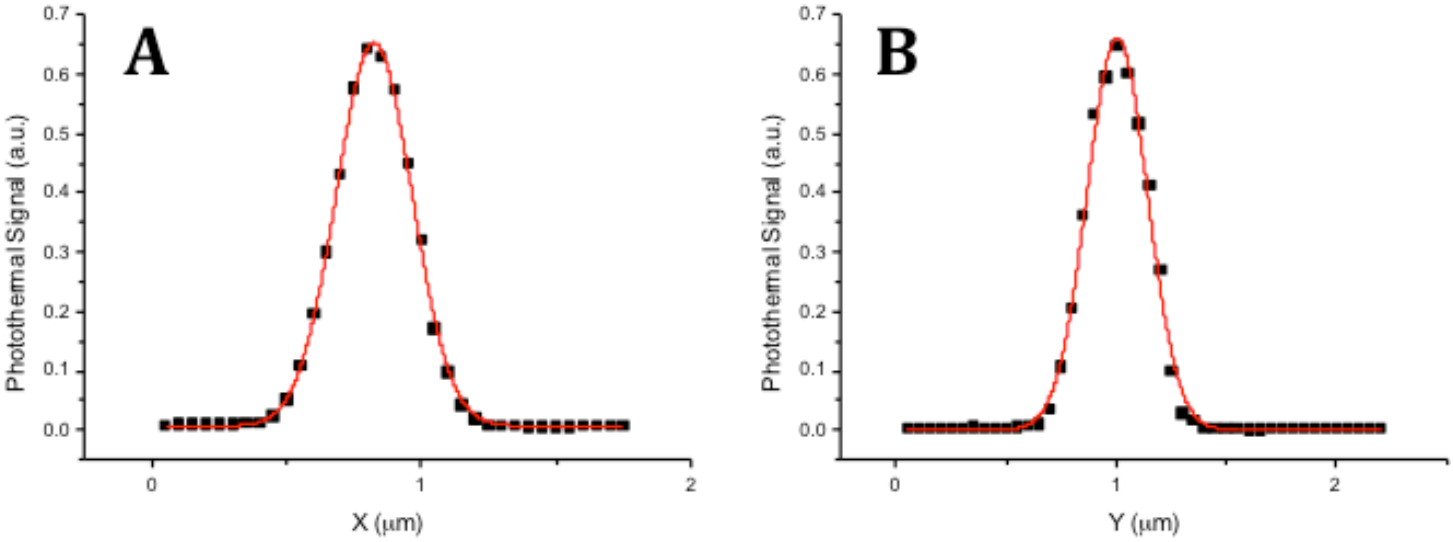

Figure 3.9 Line profiles of imaged nanoparticles at the peak photothermal intensity (■) in the lateral dimensions. Intensity line profiles for a nanoparticle both (A) with and (B) orthogonal to the scan direction fitted with a Gaussian curve (red line).

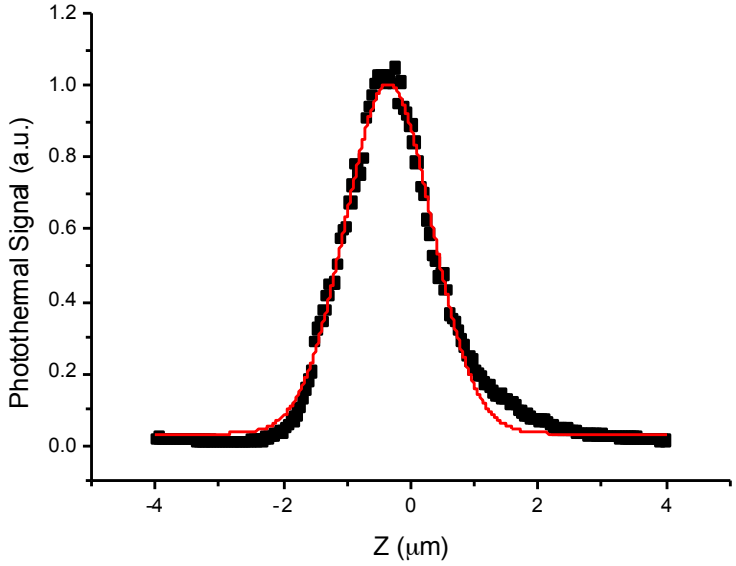

Figure 3.10 Sweep in Z direction of the confocal volume over a single nanoparticle. The acquired photothermal signal at each point is represented by the black squares (■). The data is fitted with a Gaussian curve (red line).

where $2w$ is equal to the full width of the beam at $1/e^2$ intensity. Therefore, using Equation 3.4 the lateral beam radius is 270.6 ± 6.7 nm.

Knowledge of the axial dimension of the detection volume allows the z-resolution of the system to be estimated. Previously, measurement of the axial length of the detection volume has always consisted of z-stack imaging and subsequent extraction of the intensity profile, which has been used by many authors to demonstrate the axial resolution of their photothermal microscope (Octeau *et al.*, 2009; Paulo *et al.*, 2009; Gaiduk *et al.*, 2010). This method is certainly valid for determination of this parameter; however, it relies on exceptionally good mechanical stability of the microscope. It could also be argued that this might not accurately reflect a nanoparticle diffusing through the volume, and may generate an over estimation of the axial resolution of the microscope, as it has been previously discussed that the axial fluctuations have a limited contribution to the measured diffusion time (Rigler & Mets, 1993). Here, a different approach was employed to measure the axial dimension of the microscope, whereby a single nanoparticle is moved through the volume by the piezo-stage over a few seconds and the photothermal signal recorded (referred to as a "z-sweep"). This approach eliminates any contributions from focal drift, and goes someway to simulating a nanoparticle diffusing along the axial direction of the detection volume. The z-sweep consisted of steps of 50 nm and an acquisition time at each point of 5 ms (comparable to both the resolution and dwell time for the images used for measurement of the lateral dimension). An exemplar z-sweep is shown in Figure 3.10, and is fitted with a Gaussian curve. Once again the FWHM of the fits (n = 7) were taken and averaged to give a measurement of 1.56 ± 0.14 μm, and, therefore, according to Equation 3.4 gives a $1/e^2$ beam radius of 1.32 ± 0.12 μm.

With both the axial and lateral measurement of the detection volume it is possible to calculate the actual volume of detection. This would then allow the determination of the approximate concentration of objects diffusing through the volume. Assuming again the volume is a prolate ellipsoid, the actual volume of detection is equal to 0.4 fL. This measurement, coupled with the axial and lateral dimensions, will allow both the diffusion coefficient and approximate concentration of nanoparticles diffusing in solution to be calculated. Thus, the capacity and dimensions of the detection volume will be used in the following sections to see if indeed nanoparticles of known size in solution of known viscosity can be probed.

3.7 Probing the diffusion of nanoparticles in solution: Photothermal autocorrelation spectroscopy

To achieve this a signal must be acquired from the sample over time so the autocorrelation function can be applied. The Nanonis software currently does not allow for this to be done in an automated fashion, and certainly does not allow the autocorrelation function to be applied in real-time. Therefore, all PhACS was performed using a custom homebuilt program written within LabVIEW (Appendix B; Section 2.10). Briefly, the program is split into two main parts; acquisition of the photothermal signal over a known time (signal trace) from the Nanonis SC4/program, and subsequent autocorrelation of that signal to give an autocorrelation curve. Typically, each curve is kept in memory and all the curves will be averaged at the end of the acquisition to give a final autocorrelation curve. Analysis of the curves is performed “off-line” using a custom written fitting algorithm (Appendix B) in Origin 8.5 based on the model discussed (Equation 3.3) earlier for fluctuations in an ellipsoidal detection volume.

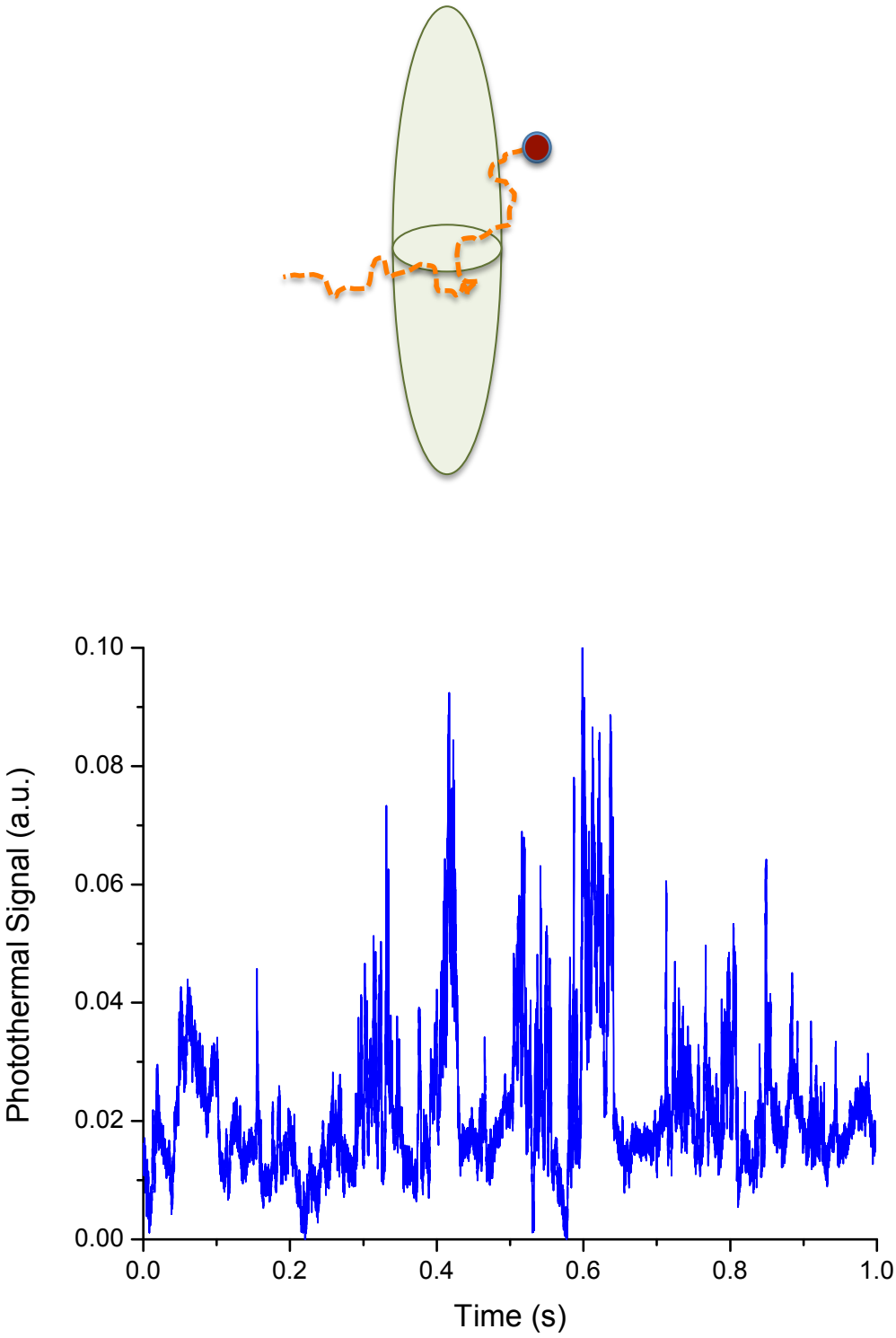

Figure 3.11 Photothermal signal acquired from 15 nm gold nanoparticles in 50 % glycerol over a period of 1 s. The fluctuations seen in the photothermal signal are due to the diffusion of gold nanoparticles through the detection volume as a result of Brownian motion.

To determine the accuracy of the measured characteristic time from the autocorrelation spectra generated, calibration samples of citrate stabilised gold nanoparticles of known size were used. Nanoparticles sized 10 nm and 15 nm were mixed with a glycerol:water solution to give a final concentration of approximately 20 nM gold nanoparticles in a 50 % (w/w) glycerol:water solution. The concentration of glycerol was verified using a refractometer (Bellingham and Stanley Ltd.).

When a nanoparticle passes through the volume a fluctuation in the signal is detected, for example, a signal trace of citrate stabilised 15 nm gold nanoparticles in 50 % glycerol (Figure 3.11). It can be seen clearly in the photothermal signal trace that peaks are detected when a nanoparticle diffuses through the volume. The time over which this peak extends will be dependent on the diffusion coefficient of the nanoparticle observed and the dimensions of the volume. This is typically the type of signal traces used for autocorrelation analysis. It is worth considering, however, that this technique and analysis absolutely depend on fluctuations being present in the data. Therefore, if the number of fluctuations/events is too low, then the analysis fails. This situation may arise in two settings; either the concentration of nanoparticles is too low, hence no/very few detected fluctuations, or the concentration is too high, whereby the signal is almost constant or the detector is saturated. It is important to be mindful of these situations when performing PhACS experiments both in solution and on cells.

Another important consideration is effects of photothermally induced heating (Section 3.5) may have on the measurement of nanoparticle diffusion, for example when performing PhACS. The measured diffusion coefficients for gold nanoparticles in water has been demonstrated to depend on the excitation power used (Radunz *et al.*, 2009). Increased incident heating intensities (i.e., mW, measured before the

microscope) led to an increase in the measured diffusion coefficient, i.e., the nanoparticles moved faster, which was termed as "hot Brownian motion". This effect is influenced by the temperature increase at the surface of the nanoparticle (Radunz *et al.*, 2009). For the diameters of nanoparticles used by these authors, 20 and 30 nm, decreases in the characteristic residence times in the confocal volume were observed at surface temperatures ranging from 10 K up to 90 K. For 20 nm gold nanoparticle a rise in the surface temperature of 30 K resulted in approximately a 20 % decrease in the characteristic residence time, and thus an increase in the measured diffusion coefficient. The experimental data for a rise of 20 K at the surface of 20 nm gold nanoparticles yielded no change in the measured characteristic diffusion time expected for a nanoparticle of this size in water. Moreover, the data at "low" and "high" surface temperatures for 20 nm nanoparticles deviate significantly from the proposed model for "hot Brownian motion". Whether surface temperature changes on the scale as those described for our set-up (i.e., 24.88 K) have an effect on diffusion of smaller nanoparticles, e.g., 10 nm, were not shown, however, if "hot Brownian motion" holds for nanoparticles of decreasing sizes, it is unlikely that small changes in local temperature contribute significantly to measurement and will likely fall within the error of the measured diffusion coefficient *via* photothermal detection in our set-up.

The autocorrelation spectra of nanoparticles sized 10 nm and 15 nm are shown in Figure 3.12. The spectra decrease from their maximum value at a rate dependent on the characteristic time for nanoparticles to pass through the detection volume. The time taken for the curve to reach half the maximum value is the characteristic diffusion time (τ_D). The characteristic diffusion times for all the nanoparticle extracted when fitted with Equation 3.3 are presented in Table 3.1. From the

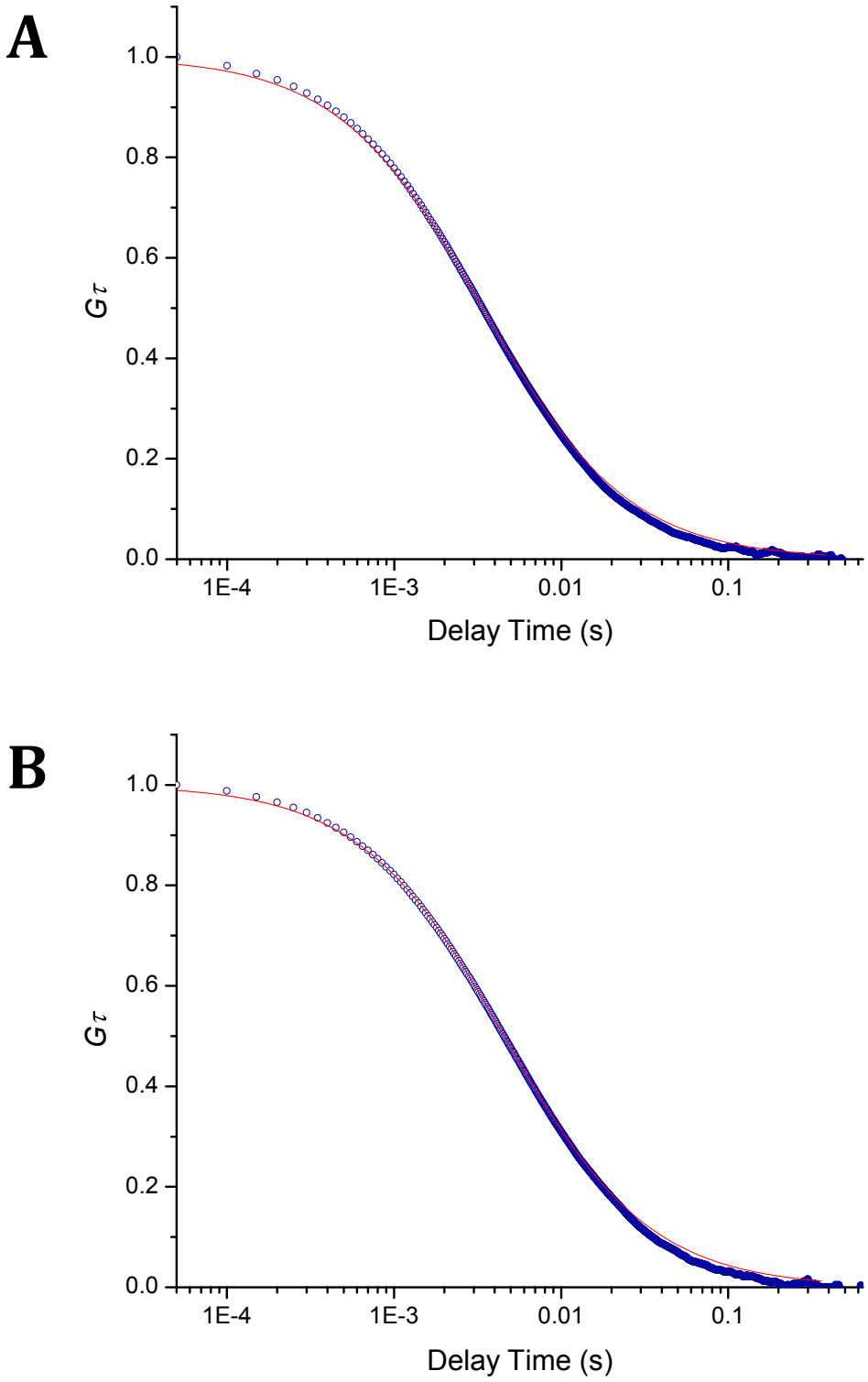

Figure 3.12 The autocorrelation function (○) for c.a. (A) 10 nm and (B) 15 nm citrate gold nanoparticles suspended in 50 % glycerol (v/v). The curves are fitted with Equation 3.3 (red line).

characteristic diffusion time it is possible to calculate the average diffusion coefficient (D) of the nanoparticles using the following equation;

$$D = \frac{w_{xy}^2}{4\tau_D} \qquad \textbf{(3.5)}$$

where w_{xy} is the lateral 1/e^2 radius of the confocal volume in microns (0.270 μm, Section 3.6.2). From the diffusion coefficient of the nanoparticles it is possible to calculate the hydrodynamic radii (R), and thus the diameter, of the detected nanoparticles using the Stokes-Einstein relation;

$$D = \frac{k_B T}{6\pi\eta R} \qquad \textbf{(3.6)}$$

where k_B is the Boltzmann constant, T is the temperature in Kelvin and η is the viscosity of the solution in Pa.s. Using Equation 3.6, the measured hydrodynamic diameter, i.e., 2 times R, was calculated (Table 3.1). It can be seen that the calculated hydrodynamic diameters from the PhACS analysis for all nanoparticles are significantly higher than that expected from the TEM data. In fact, for both nanoparticle sizes, the diameters are approximately 5-6 nm larger than the mean diameter determined by TEM. This is certainly unexpected, however, the size increase is consistent between different experiments, i.e., different nanoparticle samples. The calculated diffusion coefficient largely depends on the measured characteristic residence time measured for the nanoparticles in solution (τ_D; Equation 3.4), as the 1/e^2 radius has been previous experimentally determined (Section 3.5.2). Therefore, it is entirely possible that this error, due to the consistency in the measured τ_D, occurs in response to an error in the communication between the custom written program (Appendix B) and the Nanonis SC4 acquisition module. The origin of this

miscommunication is difficult to determine with the experimental data, however, one could use signals of known periodicity, e.g., the modulation of the excitation laser, to measure if the ability to measure time correctly arises from the Nanonis SC4 or the

Table 3.1 Characteristic diffusion time and hydrodynamic diameter by PhACS of 10 and 15 nm gold nanoparticles in 50 % glycerol (v/v)**.**

Nominal Diameter (nm)	Diameter by TEM ± SD (nm)	Characteristic Diffusion Time ± SD (τ_D, ms)	Hydrodynamic Diameter by PhACS (nm)
10	9.4 ± 1.1	3.7 ± 0.1	14.8 ± 0.4
15	13.9 ± 1.9	5.2 ± 0.1	20.8 ± 0.4

VI's in the custom program that permit the signal to be taken from the Nanonis SC4. This experiment would reveal that if the effect of increased τ_D, and therefore increased particle size arises from the discontinuity in the measured time by either program. The next section (Section 3.8) will describe the implementation of a new technique, which eliminates the need for a custom written program to perform the acquisition and requires only the use of raster scanning images to measure the diffusion coefficient of the same nanoparticles used here in solution.

3.8 Raster image correlation spectroscopy

In the previous section, it was shown that PhACS could be used to probe the diffusion dynamics of gold nanoparticles in solution, and extract their average diffusion coefficient(s). This technique works extremely well for homogeneous solutions/mixtures of absorbing nanoparticles. However, the data garnered from PhACS lacks spatial and temporal information about the distribution of the

nanoparticles. This flaw goes "unseen" when probing homogeneous solutions, however, if the distribution of nanoparticles (concentration) and their diffusion speeds were to be inhomogeneous, then performing PhACS at a single point within the sample would lead to at best an inaccurate measure of the actual dynamics of diffusion. This is particularly important in the context of a biological system, where the distribution of labelled biomolecules could indeed, and are likely to be, inhomogeneous, due to biological structures at different length scales

In fluorescence microscopy, FCS is routinely used to measure the diffusion coefficient of fluorescently labelled biomolecules. Apart from suffering with photostability issues of the fluorescent label, as described earlier (Chapter 1 Section 1.1.3), it too suffers from the lack of spatial information described above. This led to a development of an extension to this technique known as fluorescent RICS, which relies on the temporal correlation of raster scan images of a sample, and has been used to investigate the diffusion dynamics of fluorescent molecules both in solution and in/on cells.

Fluorescent RICS, first described by Digman *et al.*, is a technique that measures the signal intensity, and, therefore, the fluctuations, during a raster scan image. It was shown that the raster scan images provided identical information on the diffusion dynamics seen in FCS measurements. However, it also provided spatial correlation information, which is not present when a single point FCS measurement is performed. The RICS method can be applied to most existing fluorescent laser scanning microscopes. The acquisition of the RICS data is relatively simple, if one has very good control over the signal-to-noise of the system, whereby successive raster scan images are acquired over time. The imaging path must follow that of a raster scan for the analysis to be carried out (Figure 3.13A), as exact knowledge of a

pixel's or line's position in time is critical. By having this knowledge it allows the intrinsic time structure of the raster scan to be exploited, and the data, therefore, generate temporal information about the sample in the range of; microseconds (a pixel or many pixels), milliseconds (a scan line or many scan lines), and seconds (an image or multiple images) (Figure 3.13B). This, coupled with the spatial information present within the image, gives a unique method for probing the "fast" (μs) and "slow" (s) dynamics of biomolecules over a relatively large detection area.

Although the acquisition of the data is an important part of this technique, equally important is the deconvolution of these data to yield information on the fluctuations present therein. This is done again by a correlation analysis, however, it is not as simple as the single point autocorrelation spectroscopy discussed earlier.

The autocorrelation function of a molecule diffusing through the detection volume at a single point decays with a characteristic time dependent on the diffusion coefficient and the dimensions of the volume. However, when applying the RICS methodology the sample is probed at many different spatial locations (typically pixel sizes are on the scale of 50-200 nm) throughout the raster scan, that are not equally spaced in time. Thus, the correlation analysis applied in ACS (Equation 3.2) cannot be applied to raster scan images. Instead a spatial correlation is applied defined as;

$$G_S(\xi, \Psi) = \frac{\langle I(x,y)I(x+\xi, y+\Psi)\rangle_{x,y}}{\langle I(x,y)\rangle^2_{x,y}} \qquad \textbf{(3.7)}$$

where ξ and Ψ are the spatial increments in the x and y directions, respectively, and the angle brackets indicate averaging over all the spatial locations in both x and y directions. In order to calculate the spatial correlation for a two-dimensional spatial

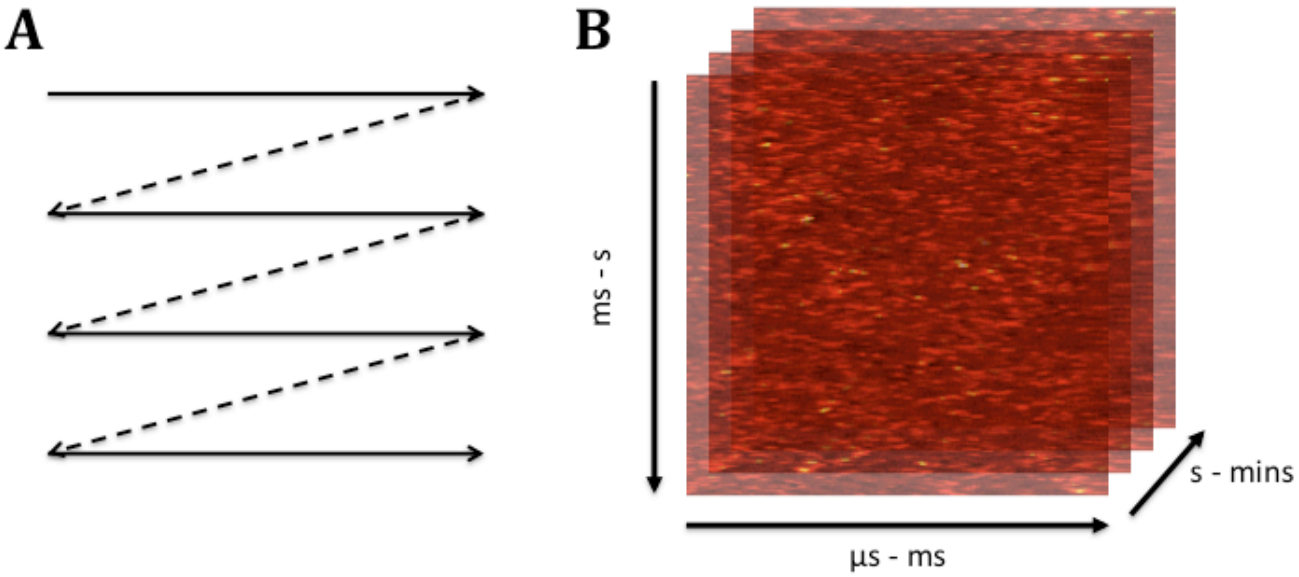

Figure 3.13 A raster scan and the time structure within sequential raster scan images. (A) An example of a raster scan path, whereby one line is acquired (solid arrows) and then the scanner moves back to the beginning of the next line (dashed arrows) (B) Raster scanning an area multiple times yields time resolved information in the range of; µs to ms within a scan line, ms to s within an image and s to minutes within the stack of images.

raster scan image in which objects are diffusing an overall correlation function is applied, $G_S(\xi,\Psi) = S(\xi,\Psi) \times G(\xi,\Psi)$, where

$$S(\xi,\Psi) = \exp\left(-\frac{\frac{1}{2}\left[\left(\frac{2\xi\delta r}{w_0}\right)^2 + \left(\frac{2\Psi\delta r}{w_0}\right)^2\right]}{\left(1+\frac{4D(\tau_p\xi+\tau_l\Psi)}{w_0^2}\right)}\right) \quad \textbf{(3.8)}$$

$$G(\xi,\Psi) = \exp\left(-\frac{\frac{1}{2}\left[\left(\frac{2\xi\delta r}{w_0}\right)^2\right]}{\left(1+\frac{4D(\tau_p\xi+\tau_l\Psi)}{w_0^2}\right)}\right) \quad \textbf{(3.9)}$$

Here, D is the diffusion coefficient, δr is the distance between adjacent points in the line or between lines, w_0 is $1/e^2$ of the Gaussian illumination profile, and $\tau_p$and τ_l are the time per pixel and per line, respectively. Using Equation 3.8 and 3.9 it is possible to fit spatially correlated raster scan images, and therefore extract the average diffusion coefficient of the molecule present within the sample. This means, for example, if an object is "slowly diffusing" there is likely to be correlation between the pixel it is detected at and the immediately neighbouring pixels, as these pixels will correspond to the dimensions of the detection volume. However, if an object is diffusing "faster" the fluctuation lasts longer than the time taken to move a distance corresponding to the detection volume. Therefore, it can be said that the correlation decreases with a characteristic length dependent on the diffusion coefficient and the dimensions of the detection volume (Digman *et al.*, 2005).

Used extensively by the group of Enrico Gratton, RICS has proved a very useful tool for investigating the diffusion and concentration of fluorophores in solution and fluorescently labelled proteins in cells. For example, RICS was able to effectively measure the diffusion speed and concentration of fluorescein and mEGFP

in solution, which compared favourably with FCS measurements of the same sample (Brown *et al.*, 2008; Digman *et al.*, 2009). It was subsequently applied to probing the diffusion of mEGFP tagged paxillin in Chinese hamster ovary cells (CHO) and revealed that paxillin was present in the cytoplasm on average in clusters of 2-4 proteins per cluster (Brown *et al.*, 2008).

The RICS approach has been demonstrated to work in the setting of fluorescence microscopy, however, an interesting question is if the analysis can be used for other non-fluorescence based techniques, such as photothermal microscopy. Although the final raster scan images from both techniques are very similar it must be noted that the acquisition is not. With a fluorescence microscope the laser is scanned across the sample, i.e., the sample remains in a fixed position. In photothermal imaging the sample is moved across the fixed laser position by a piezo scanning stage. This means that scanning with a photothermal microscope is conventionally slower than a fluorescence microscope. However, here it is demonstrated that it is possible to scan at speeds allowing comparable pixel dwell times for the raster scan (~ 200 μs). This dwell time will be used for all the images presented in connection with the RICS analysis. This new combination of photothermal microscopy and RICS will be called PhRICS.

3.9 Photothermal raster imaging correlation spectroscopy

Previously, the observation of nanoparticle diffusion (and the proteins they label) *via* photothermal microscopy has been executed using two approaches, PhACS and photothermal tracking (Lasne *et al.*, 2006; Octeau *et al.*, 2009; Duchesne *et al.*, 2012; Leduc *et al.*, 2013). Each has distinct advantages that make them more suited to a particular biological problem. Photothermal tracking yields data on the spatiotemporal position of single nanoparticle labelled biomolecules. The tracks

allow access to a broad range of diffusion modes/coefficients a single molecule can experience, which can give much insight into the heterogeneity of the molecules' environment and interactions. However, this technique, in the context of free diffusion (μs timescales) or fast reaction diffusion (tens of ms timescales), is limited by its time resolution (approximately 40 ms between points). The diffusion speed limit of the most advanced photothermal tracking set-up is in the region of 2-3 $\mu m^2/s$. This would, therefore, mean that for molecules undergoing relatively free diffusion, or fast reaction diffusion, the technique would provide a biased insight of the range of diffusion coefficients. The fast molecules will simply be quicker than the tracker and not be detected. Access to the fast populations of nanoparticles in freely diffusing environments, such as in solution or in the cytoplasm of cells, has been achieved by PhACS. However, as discussed earlier, single point autocorrelation spectroscopy suffers from a lack of coverage of the system being observed, i.e., although the position is known it only covers a single diffraction limited area, which may bias data for heterogeneously diffusing species in heterogeneously organised environments.

An approach that would bridge the gap between photothermal tracking and PhACS, would be an approach similar to that used for fluorescent RICS. This would not only provide access to fast diffusing molecules, like PhACS, but would also give the spatiotemporal information supplied by a single molecule tracking approach. Here, the development of this novel approach for photothermal microscopy is presented, termed photothermal raster imaging correlation spectroscopy.

A first goal is to see whether it is possible to generate images that would allow full access to free diffusion of nanoparticles in solution. Typically, photothermal imaging is performed with a pixel dwell time of 1-10 ms. This would be much too slow for fast free diffusion to be resolved. Therefore, photothermal images were

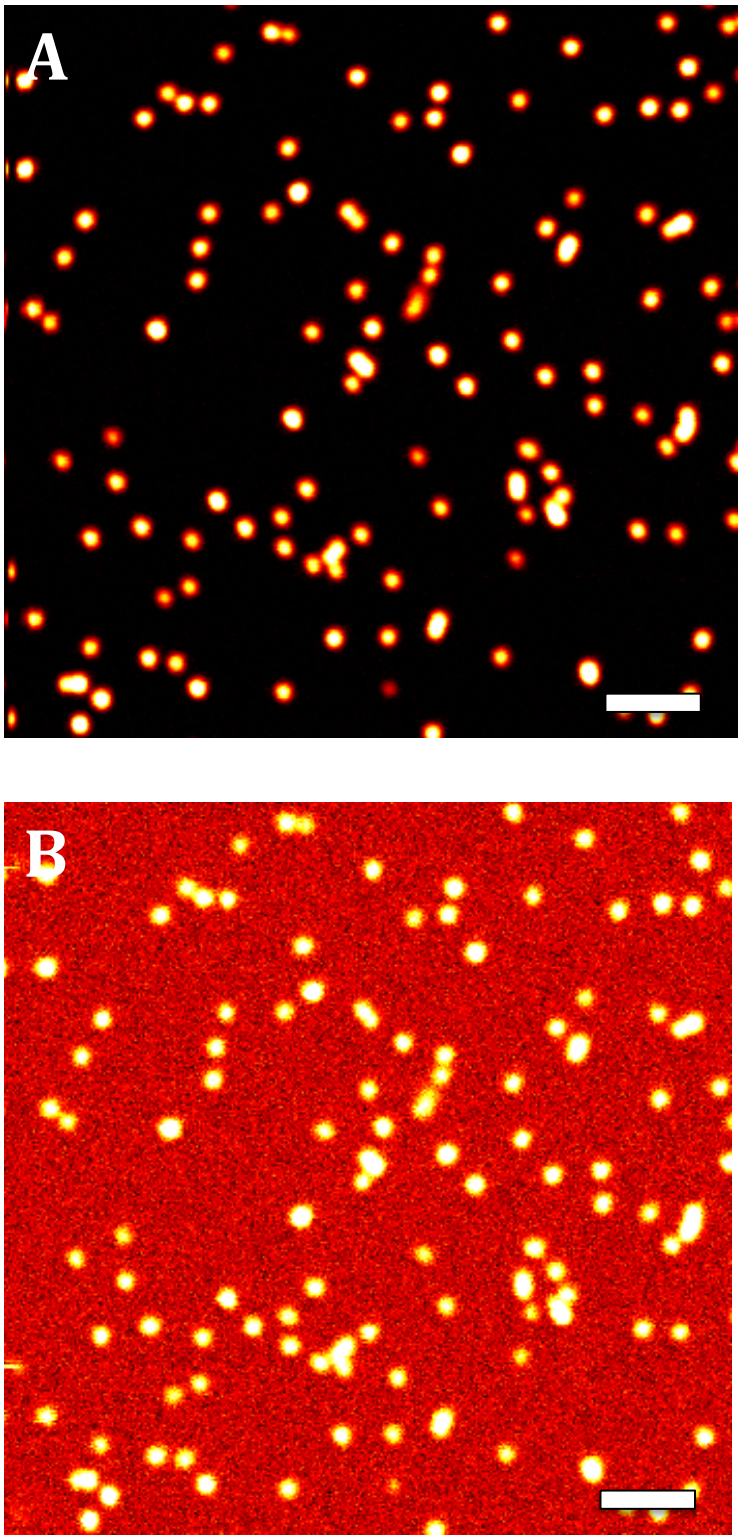

Figure 3.14 Comparison of photothermal raster scan imaging at different pixel dwell times on immobile nanoparticles. Images are of the same nanoparticles with a pixel dwell time of 5 ms (A) and 200 μs (B). Pixel size for both images is 50 nm and scale bars are 5 μm in size.

performed with a pixel dwell time of 200 μs, on a sample of biotinylated nanoparticles immobilised on a streptavidin surface (pixel size was 50 nm, Fig. 3.14). In comparison with the images taken at 5 ms pixel dwell time (Fig. 3.14A), it is clear that the nanoparticles are still detected when the dwell time is set at 200 μs (Fig. 3.14B). The approximate signal-to-noise ratio (SNR) for a single nanoparticle at 200 μs dwell time is ~ 30. This is high enough for RICS imaging to be performed, as a SNR of 10 or greater is required for single nanoparticle tracking applications. Therefore, these parameters will be used throughout this thesis for PhRICS.

Now that fast raster scanning can be utilised to give appropriate photothermal images for RICS analysis, the next step is to perform PhRICS experiments and compare the results to an already established method. Therefore, to this end PhRICS was performed on the nanoparticle samples used for calibration of the PhACS acquisition in Section 3.7. Comparison of the calculated diffusion coefficients from the two techniques will show if the PhRICS approach is an applicable technique for probing the diffusion of nanoparticles.

For PhRICS imaging in solution a 12.8 μm by 12.8 μm area approximately 10 μm into the sample was raster scanned with approximately 50-70 images taken for analysis to be performed. The images were 256 by 256 pixels with a pixel size and dwell time of 50 nm and 200 μs, respectively. An example of a PhRICS image is presented in Figure 3.15A, which is the raster scan image of 15 nm gold nanoparticles in a 50 % (v/v) glycerol solution. For analysis of the PhRICS images, firstly a moving average is removed from the image sequence. This step is taken to remove immobile components from the analysis and then the spatial autocorrelation analysis is applied, and results in a final autocorrelation image (Figure 3.15B). Finally, the surface plot of the autocorrelation image is fitted with the Equations 3.8 and 3.9 that

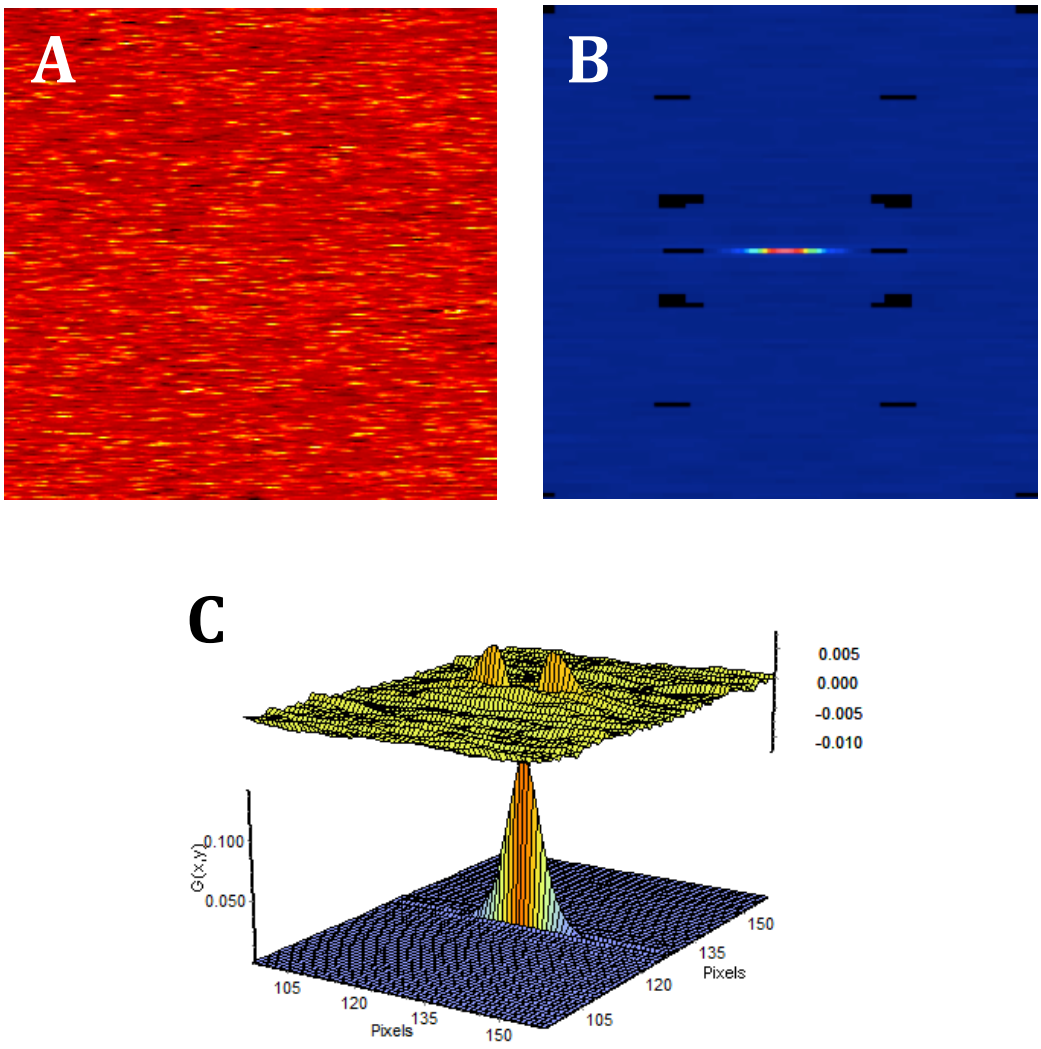

Figure 3.15 PhRICS analysis of 15 nm gold nanoparticles in 50 % (v/v) glycerol solution. (A) One frame from a PhRICS stack showing the characteristic streaking fluctuations due to diffusion of nanoparticles through the detection volume during the 12.8 x12.8 µm raster scan. (B) The averaged spatial autocorrelation image (image cropped and enlarged to show spatial correlation) of sequential RICS images after removal of moving average. (C) Surface fitting of (B) with Equations 3.8 and 3.9, with the spatial autocorrelation function for diffusion (lower axis) and the residuals (upper axis).

The PhRICS was performed on the same gold nanoparticles used for the PhACS experiments (Section 3.6, Table 3.1). The glycerol concentration for the 10 and 15 nm nanoparticle solutions was measured to be 50 % (v/v) using a refractometer. The measured diffusion coefficient for the gold nanoparticles of different sizes in glycerol solutions by PhRICS is presented in Table 3.2. For 15 nm nanoparticles in 50 % glycerol the measured diffusion coefficient was 5.0 ± 0.5 $\mu m^2/s$ which corresponds to a hydrodynamic diameter in 50 % glycerol of 14.6 ± 1.4 nm (as determined by Equation 3.5). Thus, the diameter measured by PhRICS is in excellent agreement with the expected hydrodynamic diameter, which would correspond to the,

Table 3.2 The measured diffusion coefficient and hydrodynamic diameter by PhRICS of 10 and 15 nm gold nanoparticles in 50 % glycerol.

Diameter by TEM ± SD (nm)	Diffusion Coefficient by PhRICS ($\mu m^2/s$)	Hydrodynamic Diameter by PhRICS (nm)
9.4 ± 1.1	7.5 ± 0.4	9.8 ± 0.5
13.9 ± 1.9	5.0 ± 0.5	14.6 ± 1.4

core diameter measured by TEM plus the citrate stabilizing ligand. This is in contrast to the diameter measured by PhACS (20.8 ± 0.4 nm; Table 3.1), which is ~ 6 nm greater than the diameter measured by PhRICS. The ligand shell of citrate cannot impart more than ~ 0.5 nm thickness to the nanoparticle, it appears that the larger diameters measured by PhACS are an artefact. The source of this artefact may be an acquisition/programming problem in the LabView code for acquiring the signal trace from the Nanonis SC4 software and autocorrelating it. The average hydrodynamic diameter measured PhRICS is a slightly higher than that seen by TEM. One possible

explanation is that PhRICS samples a larger number of nanoparticles due to the amount of data/images required to perform the analysis. Also, PhRICS is more sensitive to larger particles/aggregates that may be present, as they may be sampled multiple times within the image. This may have an effect when the spatial autocorrelation is applied, if the larger nanoparticle is not slow enough, or immobile, for removal by the moving average. In addition, the layer of citrate on the nanoparticle surface is likely to increase the hydrodynamic radius by ≤ 0.5 nm. In any event, these data demonstrate the greater sensitivity of the PhRICS to the sample and the species therein, due to the large area covered, as opposed to PhACS. The PhRICS analysis of 10 nm nanoparticles in 50 % (v/v) glycerol yielded a measured diffusion coefficient of 7.5 ± 0.4 $\mu m^2/s$. Again using Equation 3.5, the measured hydrodynamic diameter was calculated (Table 3.2). For 10 nm gold nanoparticles the hydrodynamic diameter was observed to be 9.8 ± 0.5 nm. Again this measurement is significantly smaller than that seen by the PhACS measurment, i.e., 14.8 ± 0.4 nm (Table 3.1). This further strengthens the argument that the larger particle sizes seen by PhACS are due to an artefact, which may arise from an error in the signal extraction the Nanonis module. The PhRICS hydrodynamic diameter for the 10 nm nanoparticles is again in excellent agreement with the TEM data, thus demonstrating that the technique can determine the diffusion coefficient and hydrodynamic diameters of gold nanoparticle in solution accurately.

3.10 Conclusions from Chapter 3

Photothermal microscopy has been shown to be a powerful optical technique for the detection at a high signal-to-noise ratio of non-fluorescent absorbing molecules and nano-objects, in particular noble metal nanoparticles. The development of the instrumentation has led to many techniques that can be used to probe the dynamics of nanoparticles, i.e., diffusion, size, concentration and interactions. Subsequently, the technique has begun to be exploited to probe biological questions at the single molecule level, owing to the exceptional signal stability.

This previous work served as a starting point for the development of a photothermal microscope at the University of Liverpool that would allow such measurements to be performed. The detection of single nanoparticles at comparable signal-to-noise ratios to the best systems in the world has been achieved, and has served as a platform for the implementation of multiple techniques like photothermal imaging and PhACS. The implementation of PhACS has allowed the diffusion dynamics of nanoparticles to be probed in solution, and thereby deduce their hydrodynamic diameters. However, the measured τ_D, and thus hydrodynamic diameters, were significantly larger than expected for the nanoparticle size. Due to the consistency of the PhACS results, and that PhRICS did not corroborate these measurements, it suggests that the problem lies within the communication between the Nanonis module and the custom written program that leads to an erroneous measurement of time. If these issues can be solved then in the future this technique could be used to probe local viscosities in unknown samples, or biological environments, and to make single point measurements of gold nanoparticle labelled proteins in or on cells.

The optical set-up has also led to the development of a novel technique that has great potential for looking at the spatiotemporal diffusion dynamics of nanoparticle labeled protein, known as PhRICS. This technique bridges the gap between the two currently existing photothermal techniques used for *in vitro* biophysics, i.e., PhACS and photothermal tracking. This technique not only allows full access to the range of diffusion coefficients that may be observed within biological samples, like PhACS, but also retains comparable spatiotemporal information encoded within a random walk. The combination of these two parameters will allow unparalleled access to the spatio-temporal organization of nanoparticle labelled protein, and with further development could be used to delineate the structure of biological environments, e.g., extracellular matrices or cytosol.

Chapter 3

4. Biological Stabilisation and Functionalisation of Gold Nanoparticles for Imaging Biomolecules and Probing Biological Interactions

To label a biomolecule in a controlled manner at a structurally defined position, long a goal of structural and chemical biologists, is an important step in the elucidation of biological functions. The labelling of specific sites or groups within a biomolecule can be achieved by many diverse strategies, whether this is the labelling of a specific amino acid(s) or chemical tags being engineered into the protein (Ong *et al.*, 2002; Waugh, 2005). However, in all instances, the functions or properties of the attached label are extremely important and depend in part on the information required, e.g., for imaging, fluorophores or nanoparticles may be used, whereas in mass spectrometry the label can help identify the fragment of interest (Aebersold & Mann, 2003; Parak *et al.*, 2005; Ori *et al.*, 2009). This has led to the labelling of molecules in live cells either by chemical reaction or by the manipulation of a cellular genome to yield a fluorescent fusion protein (Prescher & Bertozzi, 2005; Johnsson & Johnsson, 2007; Livet *et al.*, 2007). Important characteristics of these labels are that they must not only label the molecule specifically and at a defined position, but they also should not hinder the biomolecule's function.

Gold nanoparticles have been widely used in the past to label biomolecules. For example, the use of gold nanoparticles conjugated to antibodies, referred to as

'immunogold', has allowed the identification and localization of both intra- and extracellular proteins via electron microscopy (Clevenger & Epstein, 1984; Peach *et al.*, 1988). However, a longstanding challenge is to prevent such labels from aspecifically binding in the biological environment, thus yielding a "false-positive" result (Birrell *et al.*, 1987). More recently, this problem has been circumvented *via* the development of effective passivation and functionalisation strategies. This has been exploited to detect and track single gold nanoparticles on cells using photothermal microscopy and tracking. The main issue with the use of such labels in biological environments *in vitro* and *in vivo* is aspecific interaction with molecules present therein, which would render the label useless (Doty *et al.*, 2004; Duchesne *et al.*, 2008). Two main strategies are employed for the stabilisation of nanoparticles for use in biological environments; both involve anchoring of molecules to the gold surface. Use of long polymers to stabilise the surface of a nanoparticle has been employed in many instances, with many different applications proposed (Corbierre *et al.*, 2001; Freese *et al.*, 2012). For example, Freese *et al.* provided a systematic study of the effect of different polymer coatings on the interaction of the nanoparticle with primary endothelial cells. A second approach used has been the generation of a self-assembling monolayer of small ligands on the surface of the nanoparticle with a thiol group at their foot that can bind to the gold surface. Such an approach has been adopted with ligands such as alkane thiol ethylene glycols (SH-EG), peptides, and peptidols (Levy *et al.*, 2004; Duchesne *et al.*, 2008; Maus *et al.*, 2009). This has yielded success in the protection of gold nanoparticles from aspecific interactions, and has also been shown previously to better protect the nanoparticle surface than solely polymer based systems (Wuelfing *et al.*, 1998). A mixed monolayer ligand shell that combines both SH-EG and peptidol ligands has proven to be very effective in the

protection of gold nanoparticle labels (Duchesne *et al.*, 2008) and in some instances superior to SH-EG alone (Chen *et al.*, 2012). This ligand shell will be used to develop a method for preparing maleimide and thiol functionalised nanoparticles in this chapter.

The functionalisation of such protected nanoparticles is critical for their use as molecular probes. Currently, it is possible to conjugate mix-matrix nanoparticles to functional molecules, e.g., proteins (Duchesne *et al.*, 2008). The specific conjugation of FGFR (and later FGF-2) to mix-matrix nanoparticles was achieved *via* the use of a Tris-NTA ligand (Duchesne *et al.*, 2008; Duchesne *et al.*, 2012). It was demonstrated that nanoparticles of defined stoichiometry (i.e., with a single FGFR per nanoparticle) could be prepared by controlling the number of Tris-NTA ligands incorporated into the nanoparticle ligand shell (Duchesne *et al.*, 2008). The ability to control the stoichiometry of the conjugation is critical when attempting single molecule work. This approach, although leading to a stable conjugate, is non-covalent. Although Ni^{2+} Tris-NTA has a much slower K_d than NTA, due to avidity, there remains the concern that naturally occurring histidine patches on some proteins may provide binding sites for the Tris-NTA ligand. Thus, the Tris-NTA may exchange for such patches in the course of an experiment. Moreover, not all biomolecules are amenable to a hexahistidine tag, e.g., oligosaccharides. Therefore, an approach that allowed a chemically versatile covalent linkage to be formed between a biological molecule, in a structurally defined position, and a nanoparticle would be of great interest.

In this chapter, the reaction explored to achieve the above aim is that of a maleimide group with sulfhydryl groups, known as Michael addition. Two routes were attempted to prepare nanoparticles presenting the maleimide functional group; a "one-step" disulphide ligand shell method that imparts maleimide functionality in the

initial step, and a "click chemistry" approach, whereby the group is added in a later step. The first route provides a cautionary example of problems one may experience when working with disulphide ligands. In contrast, the click-chemistry route demonstrates the exceptional versatility one can achieve with maleimide functionality.

4.1 Disulphide ligand shells for gold nanoparticles: A "one-step" route to imparting maleimide functionality

Maleimide is an attractive functional group for the covalent labelling of biomolecules, due to its stability in water (c.f. N-hydroxysuccinimide commonly used to label amines), the relative scarcity of thiols on proteins, and the absence of thiols on other molecules such as nucleic acids and sugars. It thus has the potential of selectively labelling biomolecules at structurally defined positions. The name "maleimide" is a contraction of maleic acid and imide, due to its formation by reaction of maleic acid with amines and the subsequent presence of a nitrogen atom flanked by two acyl groups. The maleimide has a double bond present, which will readily react with sulfhydryl groups to form a covalent linkage, known as a Michael addition reaction (Gregory, 1955). An example reaction mechanism is presented in Figure 4.1. In the presence of a sulfhydryl group, whether this is in isolation or part of a larger molecule (e.g., thiol of a cysteine), the maleimide acts as a Michael acceptor, i.e., it allows the addition of the nucleophillic sulfhydryl group. One of the carbon atoms adjacent to the double bond undergoes nucleophillic attack by the thiolate anion. This results in the formation of a thioether bond. Depending on the carbon that is attacked by the thiolate anion, it can lead to the formation of isomeric compounds, however, the resulting thioether bond is irreversible and covalent.

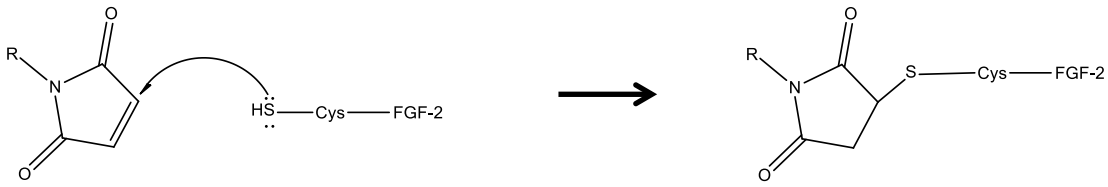

Figure 4.1 Michael addition reaction for a cysteine of FGF-2 protein to a maleimide to give a stable covalent linkage. In the presence of a sulfhydryl group of cysteine the maleimide acts as a Michael acceptor. One of the carbon atoms adjacent to the double bond undergoes nucleophillic attack by the thiolate anion resulting in the formation of a thioether bond.

The conjugation of molecules possessing a maleimide group to both flat and a nanoparticle gold surface has been explored previously. Houseman *et al.* used a mixture of molecules comprised of a PEGylated alkane chain joined by a disulphide bond (that does not react with maleimide), and the same molecule with the addition of a maleimide group on one of the polyethylene glycol chains to modify flat gold surfaces. This approach allowed incorporation of a maleimide group in one functionalisation/coating step and served as a basis for the generation of versatile surfaces for biological applications. The applications included both the immobilisation of synthetic carbohydrates, for lectin binding studies, and the conjugation of cysteine-containing polypeptides, for patterning cell adherence (Houseman *et al.*, 2003).

The incorporation of maleimide groups upon the surface of gold nanoparticles has been described previously *via* a number of different methods. Ba *et al.* demonstrated that a maleimide group could be incorporated in a two-step reaction, whereby amino groups are incorporated into the monolayer of the gold nanoparticle, and then reacted with an amino reactive maleimide functionalised molecule (Ba *et al.*, 2010). The particles were shown to be reactive with thiol groups present within liposomes, and were used for labelling and tracking of membrane lipids on live cells. Incorporation of the maleimide group, or a derivatized form, during the initial monolayer formation has also been shown. By derivatizing the maleimide group as part of a maleimide-furan Diels-Alder adduct, the reaction of the maleimide with the thiol anchoring group is avoided (Zhu *et al.*, 2006; Gobbo & Workentin, 2012). The maleimide can be liberated thereafter by heating in the presence of toluene resulting in the loss of the furan. Another strategy employed is the derivitization of the thiol group, with the maleimide, therefore, remaining unmodified (Oh *et al.*, 2010). Here a

thioctic acid was used as the anchoring group for binding to the gold surface. This meant that sulfhydryl groups were not present, and this bond would only be broken upon reaction with the gold surface. This method allowed the incorporation of the maleimide group in one reaction step to the gold nanoparticles, and it was shown that some control over the number of maleimide groups per particle could be achieved (Oh *et al.*, 2010). However, it should be noted that a single maleimide group per nanoparticle was not demonstrated, although the nanoparticles did have excellent stability to aggregation and ligand exchange in the presence of NaCl and DTT, respectively.

Therefore, it appears that two strategies are employed when wanting to incorporate a maleimide group into the monolayer of a nanoparticle. Either protection of the sulfhydryl anchoring groups is required, if the maleimide is not protected/inactive (Houseman *et al.*, 2003; Oh *et al.*, 2010), or the functionality is achieved by an additional reaction step after monolayer formation (Ba *et al.*, 2010; Gobbo & Workentin, 2012). The strategy that will be initially employed here will exploit the protection given by a disulphide bond to the sulfhydryl group, as other larger organic molecules may affect adversely the packing of the monolayer. The disulphide ligand that will be used here is that described by Houseman *et al*, i.e., two alkyl chains joined by a disulphide bond and terminated by polyethylene glycol chains. The skeletal formula of the unfunctionalised disulphide polyethylene glycol ligand used, referred to from now on as D-PEG, is shown (Figure 4.2A). This design of ligand protects the thiol group from interaction with the maleimide group when in solution, however, allows the reaction with the gold surface to proceed. The maleimide functionalised disulphide ligand (D-Mal) is also shown in skeletal form in Figure 4.2B. Houseman *et al*. have described the use of disulphide ligands to allow

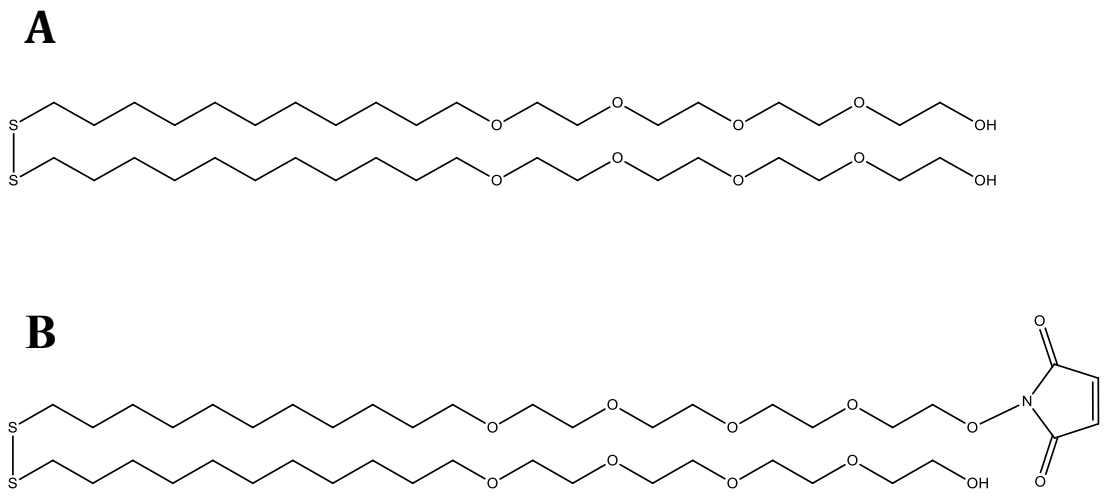

Figure 4.2 Skeletal structure of (A) D-PEG ligand and (B) D-Mal ligand used for disulphide capping reactions

"one-step" formation of monolayers with maleimide functionalisation on flat gold surfaces previously. In the present instance, the ability to perform this reaction on a curved gold surface will be explored.

4.1.1 Synthesis and stability of the D-PEG ligand shell

A first key step when synthesising a new ligand shell protocol is to assess whether the ligands self-assemble to form a shell able to stabilise the nanoparticle. The first test is colloidal stability: poor ligand shells do not prevent electrolyte-induced aggregation. A second step is to determine if the ligand shell protects the nanoparticle from non-specific binding. To this end, chromatography on a variety of common low pressure stationary phases such as Sephadex (equivalent to polysaccharides) and ion-exchange resins (equivalent to amines and carboxyl groups on proteins) has been found to provide good discrimination (Duchesne *et al.*, 2008). Finally, the resistance of the ligand shell to ligand exchange provides information on the likely density or 'packing' of ligands and whether in a biological environment endogenous thiols are likely to replace the ligand shell (Chen *et al.*, 2012). Such exchange may compromise the stability and alter the biological function of the nanoparticle.

The ligand capping reaction was essentially the same as for thiolated ligands (Chapter 2 Section 2.4). Colloidal 10 nm gold nanoparticles (BBI Ltd.) were reacted with 1 mM D-PEG ligand at a ratio of 9 volumes nanoparticle to 1 volume D-PEG ligand in methanol. The reaction was supplemented with 10xPBS Tween-20 0.1 % (v/v) to give a final concentration of 1xPBS, and left overnight with mixing on a rotating wheel. The nanoparticle/ligand mixture was then concentrated using centrifugal filters (10 kDa cut-off, PALL Ltd.) by centrifugation at 10,000 rpm for 7 min. The concentrated sample was then purified from the remaining excess D-PEG

ligand using Sephadex G-25 size-exclusion chromatography, where the pink fraction corresponding to the capped nanoparticles was collected. Functionalisation with D-Mal ligand was achieved by including a percentage (v/v of a 1 mM stock in methanol) of the D-Mal ligand in the initial ligand mix with the D-PEG.

A ligand exchange reaction with DTT (Chen *et al.*, 2012) was used to test the stability of the monolayer in the presence of a competing thiol (Chapter 2 Section 2.6). The principle of the assay is that DTT is a poor ligand and will not provide colloidal stability to the nanoparticles in the presence of electrolytes. Thus, by incubating the purified nanoparticle with DTT in the presence of NaCl, substantial ligand exchange will result in nanoparticle aggregation and a consequent red shift of the plasmon absorbance. DTT is the preferred choice for the ligand exchange reaction, as although cysteine could also be a candidate, DTT is smaller and so provides a more stringent test (Chen *et al.*, 2012). Purified D-PEG nanoparticles were incubated with 0 to 30 mM DTT and the UV-vis spectra taken at intervals from 1 hour up to 48 hours. The spectra allowed for the stability parameter for each (Chapter 2 Section 2.7.1), and thus the resistance of the D-PEG nanoparticles to ligand exchange to be quantified. The stability parameters for D-PEG nanoparticles in the presence of DTT over 48 hours are shown in Figure 4.3A. The D-PEG nanoparticles were stable up to 6 hours in all concentrations of DTT. Aggregation of nanoparticles was observed after 24 hours at the two highest concentrations of DTT, 20 and 30 mM, and at 48 hours aggregation also occurred in the presence of 10 mM DTT. Though the ligand shell is not as stable as other reported ligand shells in the presence of DTT, e.g., mix-matrix (Chen *et al.*, 2012), stability at a concentration of 10 mM DTT for 24 hours is acceptable for work in biological environments. The same ligand exchange reaction was also performed using the D-Mal ligand at 1 %

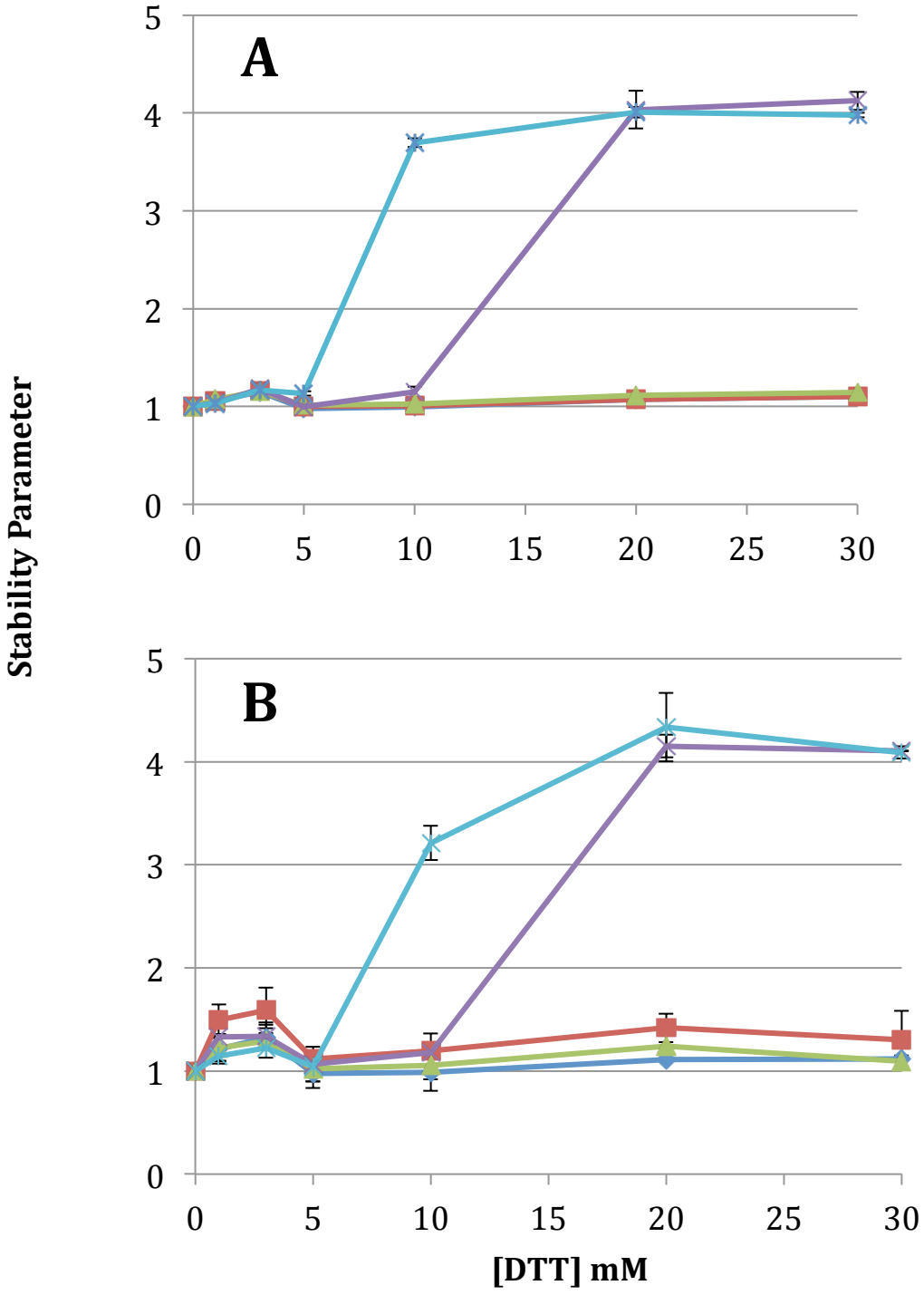

Figure 4.3 The stability parameter calculated for (A) D-PEG NPs and (B) 0.1 % D-Mal NPs at different concentrations of DTT. The stability parameter was taken at time points of 1 hour (◆), 3 hours (■), 6 hours (▲), 24 hours (×) and 48 hours (✳).

(v/v) of the ligand, and the stability was identical to that of the solely D-PEG monolayer (Fig. 4.3B). Thus, D-PEG formed a monolayer on the nanoparticles that imparted good stability and the stability of the monolayer was not undermined by the addition of D-Mal ligands.

4.1.2 Michael addition of biomolecules to maleimide and thiol functionalised D-PEG nanoparticles

The next step was to use the maleimide function to conjugate the nanoparticles to molecules of biological interest. The conjugation reaction should proceed through a Michael addition reaction, as previously described. To this end, two biomolecules were chosen as exemplars; a maleimide modified heparin-derived hexasaccharide, and a recombinant protein, FGF-2. The interactions between HS and FGF-2 are discussed in Chapter 1.

D-Mal nanoparticles will require thiol groups on proteins for conjugation, which can be naturally occurring as the side-chain of cysteine residues. The FGF-2 protein has 4 cysteine residues, but only two are at the surface of the protein, i.e., not buried in the core of the structure (Figure 4.4). These residues are at positions 77 and 95 in the polypeptide backbone. However, C-77 is only partially exposed, and, therefore, the likely candidate for Michael addition is C-95. It is worth noting that both of these cysteine residues are on surfaces of the protein distinct from its heparin binding sites (Ori *et al.*, 2009; Xu *et al.*, 2012). Therefore, the conjugation reaction is unlikely to hinder heparin/heparan sulfate binding. The conjugation proceeded by mixing D-Mal nanoparticles with a 3.5 times molar excess of FGF-2 protein. The reaction was left for 3 hours with mixing on a spinning wheel. Subsequently, the mixture was purified using heparin affinity chromatography (heparin agarose, Biorad) with 10 mM phosphate as the mobile phase (Figure 4.5). In the absence of maleimide

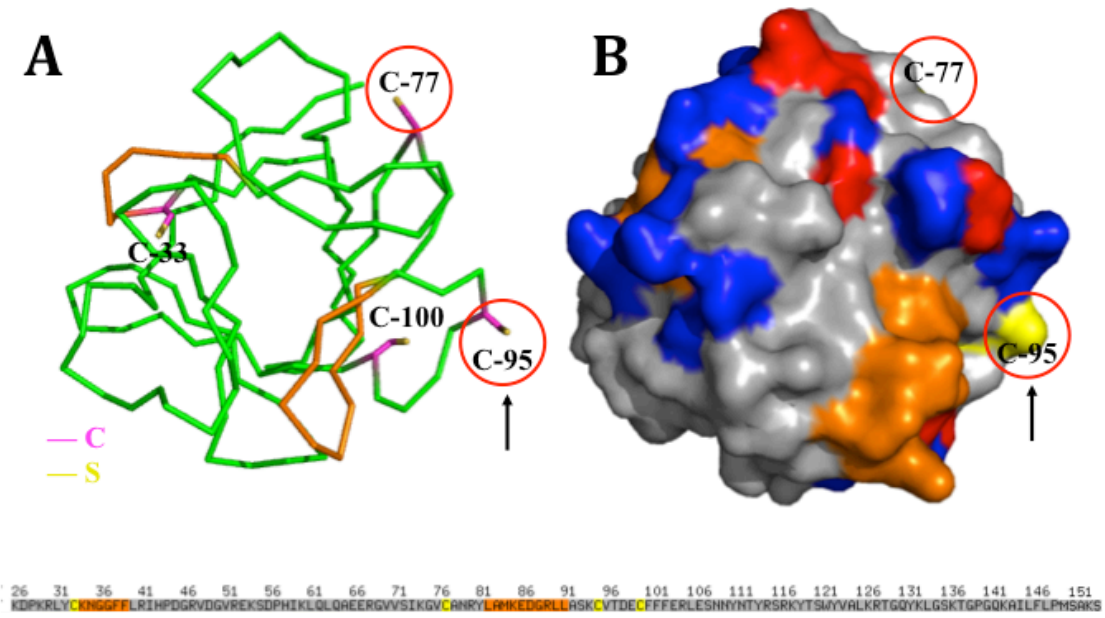

Figure 4.4 FGF-2 crystal structure. FGF-2 structure is represented in both (A) ribbon and (B) electrostatic surface forms. All cysteines in FGF-2 are denoted in (A), whereas only the surface cysteines in (B) are ringed (red). The candidate cysteine for Michael addition to our nanoparticle is marked with the arrow (black). The heparin binding sites of FGF-2, according to Ori *et al.*, 2009, are marked in both (A) and (B) along with the polypeptide sequence (bottom) in orange.

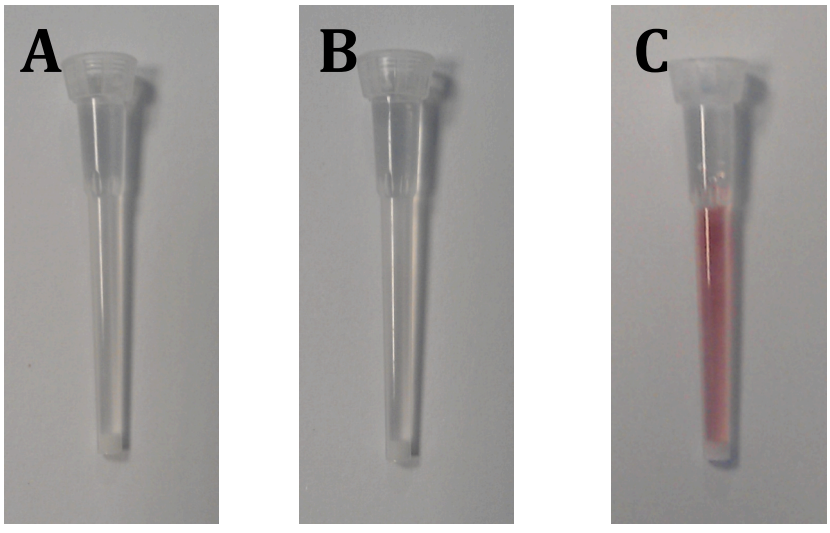

Figure 4.5 Heparin agarose affinity chromatography columns loaded with; A) D-PEG NPs incubated with FGF-2 protein, B) D-Mal NPs and C) D-Mal NPs after incubation with FGF-2 protein.

functionality, Michael addition of the nanoparticle to the protein cannot occur; hence no pink colour is seen on the column (Figure 4.5A). The same result is seen when D-Mal nanoparticles in the absence of FGF-2 protein are loaded onto the column and subsequently washed (Figure 4.5B). However, when FGF-2 protein and D-Mal nanoparticles are incubated together and then loaded onto the column a pink colour is seen (Figure 4.5C). This can only occur if the FGF-2 protein is covalently conjugated to the nanoparticle *via* Michael addition, and that its heparin binding function is not perturbed. A further demonstration that the binding of nanoparticles to the column is a result of FGF-2 conjugation is that they are characteristically eluted from the heparin agarose with 2 M NaCl. Thus, this demonstrates that it is indeed possible to conjugate proteins that possess naturally occurring thiol groups, by virtue of a cysteine side chain(s), to D-Mal nanoparticles *via* a Michael addition reaction. Conjugation of FGF-2 protein to nanoparticles has been demonstrated previously, however, this is the first time the conjugation method has yielded a covalent linkage between protein and nanoparticle. This route would also be applicable to other proteins that present an exposed cysteine or proteins that have been engineered to have a surface accessible cysteine.

One advantage of the maleimide functionalisation of nanoparticles is that it provides a versatile platform for the conjugation of other biomolecules. The second exemplar is the conjugation of a heparin-derived hexasaccharide, which provides a tool for imaging FGF-sugar complexes. The reactivity of the reducing end of heparin and heparan sulfate-derived oligosaccharides is poor and production of oligosaccharide-nanoparticle conjugates through reaction of the reducing end with amines on the nanoparticle will have a very low yield. For this reason, the reducing end of the oligosaccharides was first reacted with 4-(4-N-Maleimidophenyl) butyric

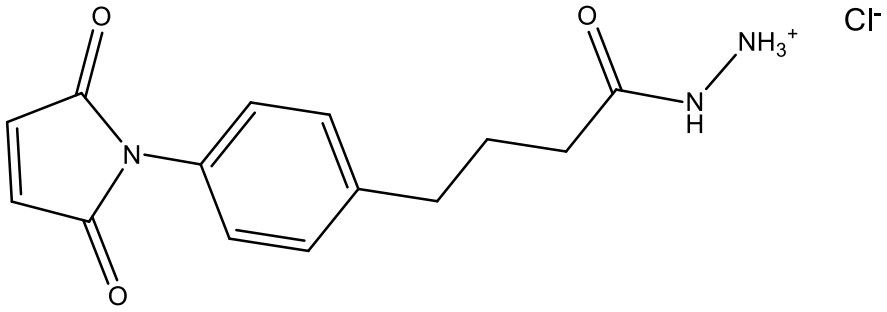

Figure 4.6 MPBH molecule used to label the non-reducing end of oligosaccharides with a maleimide group.

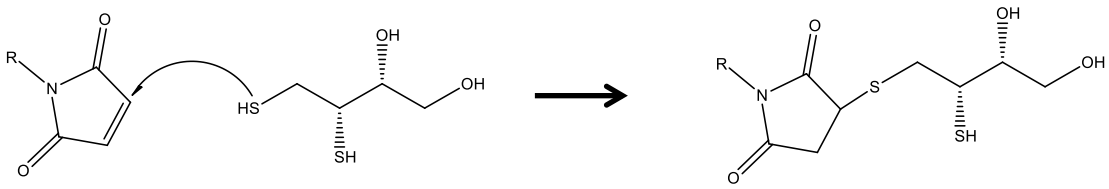

Figure 4.7 Michael addition reaction of DTT and a maleimide. This reaction gives a stable covalent thioether linkage between the DTT and maleimide as a product with a free thiol group for further Michael addition reactions.

acid hydrazide (MPBH, Thermo Scientific; a skeletal structure is presented in Figure 4.6). The hydrazide undergoes a Schiff base reaction with the carbonyl group present at the non-reducing end, yielding a maleimide functionalized oligosaccharide (Gift of Nina Azmi; Azmi, PhD thesis, University of Liverpool, 2012). Thus, this yields a convenient functional group with good reactivity. The problem remains to introduce a thiol to the nanoparticle that will allow the reaction with the maleimide functionalised sugar to occur. Since thiols bond strongly to the gold surface, the thiol must be introduced after the assembly of the ligand shell. This was accomplished by reacting D-Mal NPs with a 1 mM excess of DTT, conditions where ligand exchange will not occur (Figure 4.3). One of the thiols on the DTT molecule will react with the maleimide on the nanoparticles, and this would leave a free unreacted thiol, thus achieving thiol functionalised gold nanoparticles (Figure 4.7).

D-Mal NPs were reacted with a 1 mM excess of DTT for 1 hour with mixing on a spinning wheel; D-Mal NPs are stable at this concentration of DTT for 48 hours, (Figure 3.3), therefore, significant ligand exchange is unlikely to occur. The excess DTT was removed by Sephadex G-25 size-exclusion chromatography with 1xPBS Tween-20 0.05 % (v/v) as the mobile phase. The purified thiol functionalised nanoparticles (D-SH NPs) were then concentrated approximately 5-fold using centrifugal filters. The D-SH NPs were then reacted with an excess of maleimide-hexasaccharides. The resulting mixture was then subjected to anion-exchange chromatography on DEAE-Sepharose with 10 mM phosphate as the mobile phase (Figure 4.8). When neither the maleimide hexasaccharide nor the thiol is present in the reaction mixture, no binding of nanoparticles is seen on the

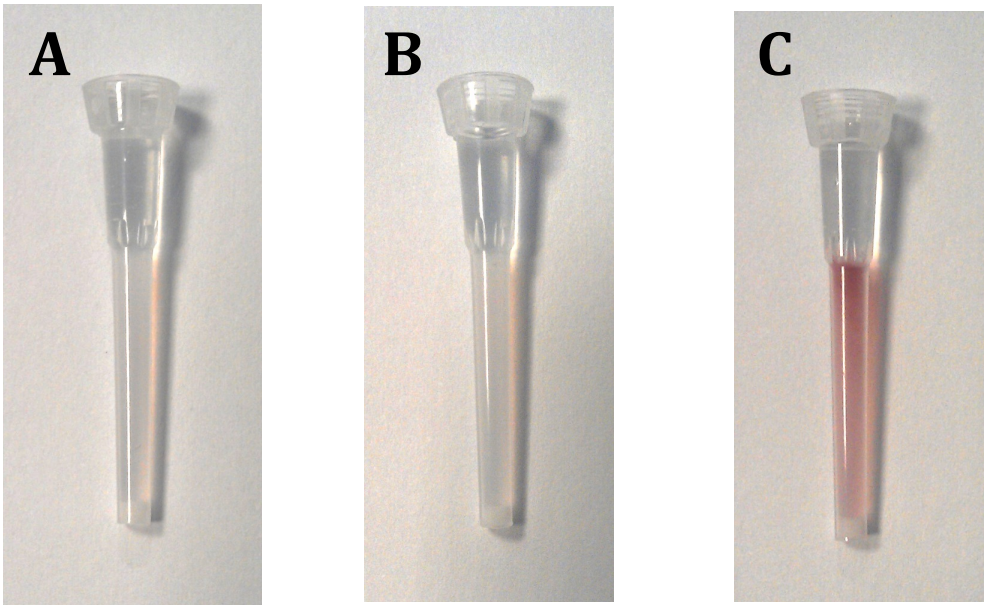

Figure 4.8 DEAE-Sepharose anion exchange chromatography columns loaded with; (A) D-PEG NPs incubated with hexasaccharide, (B) D-Mal NPs and (C) D-Mal NPs after incubation with maleimide hexasaccharide.

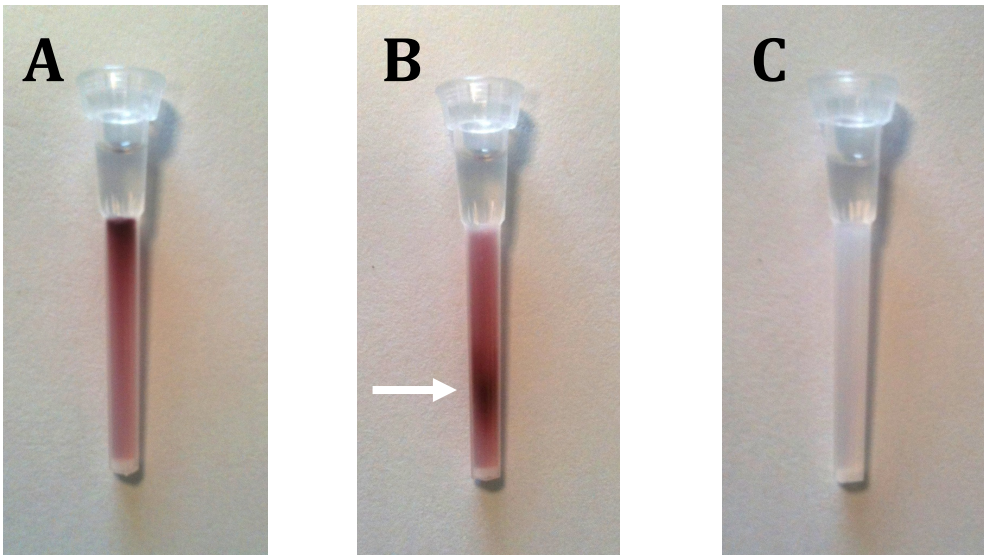

Figure 4.9 DEAE-Sepharose column of D-PEG NPs after a period at 4°C. (A) D-PEG loaded onto column. (B) Elution with 1 column volume of 2M NaCl. White arrow indicated movement of a concentrated band of nanoparticles. (C) Same DEAE-Sepharose column as in (A) and (B) after washing with 3 column volumes of 2M NaCl.

DEAE Sepharose (Figure 4.8A and B). However, when D-SH NPs are mixed with the maleimide functionalised hexasaccharide, a pink colour is seen at the top of the DEAE-Sepharose. This indicates that the Michael addition reaction between the maleimide of the hexasaccharide and the thiol on the nanoparticle was successful as the nanoparticle can now be purified due to the charge of the sugar; nanoparticles were eluted with 2 M NaCl, consistent with hexasaccharide functionality on the nanoparticles (Figure 4.8C).

The next step would be to use these nanoparticles for investigating the interaction of FGF-2 with the hexasaccharide, as it has been demonstrated previously that an oligosaccharide of this length will bind the protein (Delehedde *et al.*, 2002). However, continuation of this experimental work was impaired by poor chemical stability of the reagents. Upon repeating the synthesis over the course of nine months, the nanoparticles with a D-PEG ligand shell began to show evidence for a negative charge. These "age-related" properties of the disulphide ligand are described in more detail in the next section.

4.1.3 "Age-related" adsorption of D-PEG nanoparticles to DEAE-Sepharose

Over time, nanoparticles synthesised with D-PEG ligand began to show evidence for negative charge. In the previous section, purification of nanoparticles functionalised with hexasaccharide was achieved by DEAE-Sepharose anion-exchange chromatography. The controls for the purification, i.e., D-PEG NPs incubated with an excess of hexasaccharide and D-Mal NPs only, did not bind to the DEAE-Sepharose columns (Figure 4.8A and B). However, when this protocol was repeated with the same batch of ligand capped nanoparticles, which had been stored at 4°C for 6 months, the control nanoparticles were observed to bind to the DEAE

Sepharose. Repetition of the experiment, with nanoparticles capped with the D-PEG ligand stored at -20°C also gave the same result. This indicated that the problem must come from the capping ligand, and that the monolayer formed on the nanoparticles exhibits a negative charge (indicated by the binding to DEAE-Sepharose). This led to a new batch of ligand being ordered, which was used immediately from the company for synthesis of D-PEG nanoparticles. Figure 4.9 depicts the anion-exchange chromatography on DEAE-Sepharose of 10 nm gold nanoparticles capped with the new batch of D-PEG ligand. When loaded onto the column the nanoparticles bind to the resin, and the column appears pink, with a concentrated band at the column bed (Figure 4.9A). This indicates anion-exchange and, thus, the monolayer does indeed possess a negative charge, and this time the negative charge was present on the ligand immediately from shipment. This is further confirmed when 2 M NaCl was applied to the column, which caused the band of nanoparticles to chromatograph immediately (white arrow, Figure 4.9B). All nanoparticles were eluted from the DEAE-Sepharose by washing with 3 column volumes of 2 M NaCl (Figure 4.9C). This behaviour is consistent with what would be expected for anion-exchange purification of negatively charged groups on a biomolecule, or nanoparticle. However, the origins of this behaviour and how it manifested over time are mysterious. One cause may be modification of the structure of the ligand, which may have led to the formation/addition of negatively charged groups, e.g., a carboxylic acid. To further understand if structural changes to the ligand were the cause of this negative charge mass spectrometry would need to be performed. However, as reproducibility of the preceding work (Section 4.1.2) was not possible, a second route to achieve maleimide functionality was explored and will be described in the remainder of this chapter.

4.2 Copper-free click chemistry route to maleimide functionality: Versatile labelling of biological molecules with gold nanoparticles

Generally, "click chemistry", describes a subset of chemical reactions that lead to the formation of new products from smaller simpler reactants, under mild conditions. The azide-alkyne Huisgen cycloaddition is perhaps the best known of these, and has been adopted extensively to modify biological molecules and nanoparticles (Lutz & Zarafshani, 2008). This reaction occurs in the presence of a copper catalyst and an example of its use is the coupling of bacterial lipases to gold nanoparticles, such that the enzyme retained its activity (Brennan *et al.*, 2006). One drawback is the use of a Cu^{+} catalyst. Cu^{+} is quite reactive and may cause unwanted side reactions, such as the production of hydroxyl radicals through the Fenton reaction (Lloyd *et al.*, 1997), which could damage either the biomolecule or the nanoparticle ligand shell. Moreover, should the Cu^{+} not be entirely removed after conjugation, then Fenton reactions mediated by the metal ion may damage the biological system and cause unwanted stress responses (Lloyd & Phillips, 1999).

Baskin *et al.* described a copper-free method for this reaction, often referred to as "copper-free click chemistry". This method is particularly advantageous for use in biological systems, as it removed the need for a copper catalyst. The reaction was achieved by the use of two fluorine atoms, which withdrew electrons from a cyclooctyne. This geometry generates strain on the carbon-carbon triple bond that subsequently promotes the cycloaddition reaction in the absence of a catalyst. This allowed Baskin *et al.* to label covalently, and with high specificity, cell surface glycans for investigation of their transmembrane trafficking. An exemplar reaction mechanism between an azide group and a cyclooctyne is depicted in Figure 4.11. The reaction depicted shows a different strained cyclooctyne, whereby the strain is

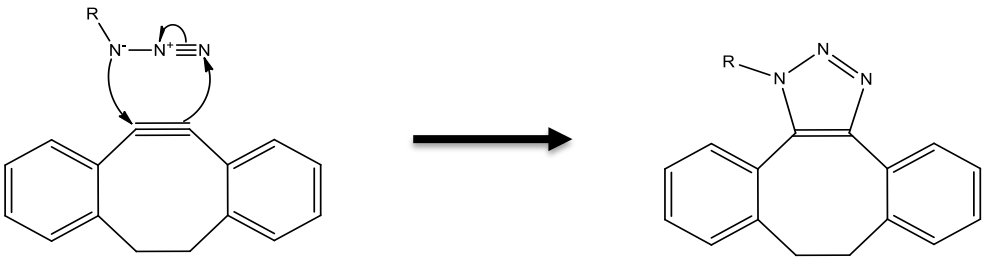

Figure 4.11 Copper-free cycloaddition of DIBO and an azide group. The reaction forms a stable triazole. The triple bond of DIBO interacts with the dipole of the azide moiety, which leads to the pericyclic formation of a stable triazole.

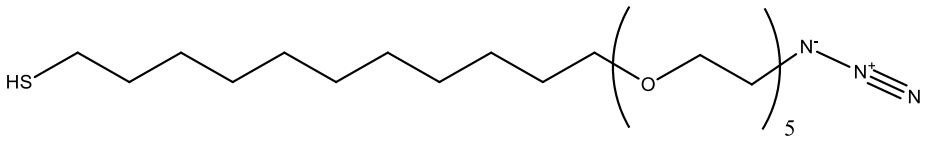

Figure 4.12 Skeletal structure of the azide ligand.

provided by flanking aryl groups, a result of an iterative process of modifications to the fluorinated cyclooctyne presented in Baskin *et al.*, in order to improve reaction kinetics (Jewett *et al.*, 2010). The reaction proceeds *via* a simple 1,3-dipolar cycloaddition reaction, whereby the triple bond of the dibenzocyclooctyne (DIBO) interacts with the dipole generated by the azide group. This azide acts simultaneously in this reaction as both a nucleophile and an electrophile, thus, leading to the pericyclic formation of a stable triazole.

In the following sections, gold nanoparticles with an azide ligand are functionalised, *via* copper-free click chemistry, with a strained cyclooctyne possessing a maleimide. The azide ligand shell is shown to be stable to DTT-mediated ligand exchange and, therefore, amenable to use in biological environments. It is demonstrated that the number of maleimides on the nanoparticle can be controlled, thus, gold nanoparticles with one maleimide group can be prepared. The conversion of this functional group to a thiol group *via* the reaction of DTT is also described. Gold nanoparticles bearing a single maleimide or a thiol are then used in the conjugation to both protein and oligosaccharide respectively, in a controlled stoichiometry of 1:1. The nanoparticles then provide a tool for investigating the interactions of these biomolecules using photothermal microscopy (Chapter 5 Section 5.2 and 5.5).

4.2.1 Stable azide functionalised gold nanoparticles: A template for copper-free click chemistry

Functionalisation of nanomaterials with azide functional groups has been described previously, and has provided a versatile platform for additional covalent reactions with strained cyclooctynes *via* both copper catalysed and copper-free click chemistry (Brennan *et al.*, 2006; Bernardin *et al.*, 2010). Azide containing

nanoparticles were generated by the incorporation of a small percentage of an azide functionalised alkane-thiol PEG ligand into a mixed monolayer of peptidol and alkane-thiol PEG (structure of the azide ligand is presented in Figure 4.12). The constituents of the mixed monolayer and the rational for the ligand proportions are described in Duchesne *et al*., (2008). Upon addition of the azide ligand the other constituent ligands are proportionally scaled down to allow for the percentage of functional ligand in the ligand mix. Hence, the ligand mix consisted of 99 % (mol/mol) of matrix ligands (70:30, CVVVT-ol to HS-C_{11}-EG_4-OH, respectively) supplemented with 1 % (mol/mol) azide ligand (HS-C_{11}-EG_5-N_3). The reaction was buffered by the addition of 10xPBS (pH 7.4) supplemented with Tween-20 0.1 % (v/v) to give a final concentration of 1xPBS, and left overnight with mixing on a rotary wheel. Excess free ligand was then removed from the nanoparticles by Sephadex G-25 size-exclusion chromatography with 1xTBS (pH 7.6) Tween-20 0.05% (v/v) as the mobile phase. The reason for the use of 1xTBS as the mobile phase was that this was the recommended buffer for use of particles for the subsequent conjugation reaction (Promega); however, this reaction was seen to proceed in 1xPBS also.

The purified azide functionalised gold nanoparticles (N_3NPs) were used as is to set up a ligand exchange reaction in the presence of DTT, as previously described (Chapter 2 Section 2.5). The UV-vis absorption spectra for the reaction were taken at various time intervals and the stability parameter (SP) was calculated (Figure 4.13). The stability of the N_3NP monolayer is identical to that of nanoparticles only possessing mix-matrix ligands. Both show resistance to ligand exchange in the presence of 10 mM DTT up to 48 h (Figure 4.13A and B). Stability of the 1 % N_3NPs at 24 h in 10 mM DTT is consistent with previously reported ligand exchange

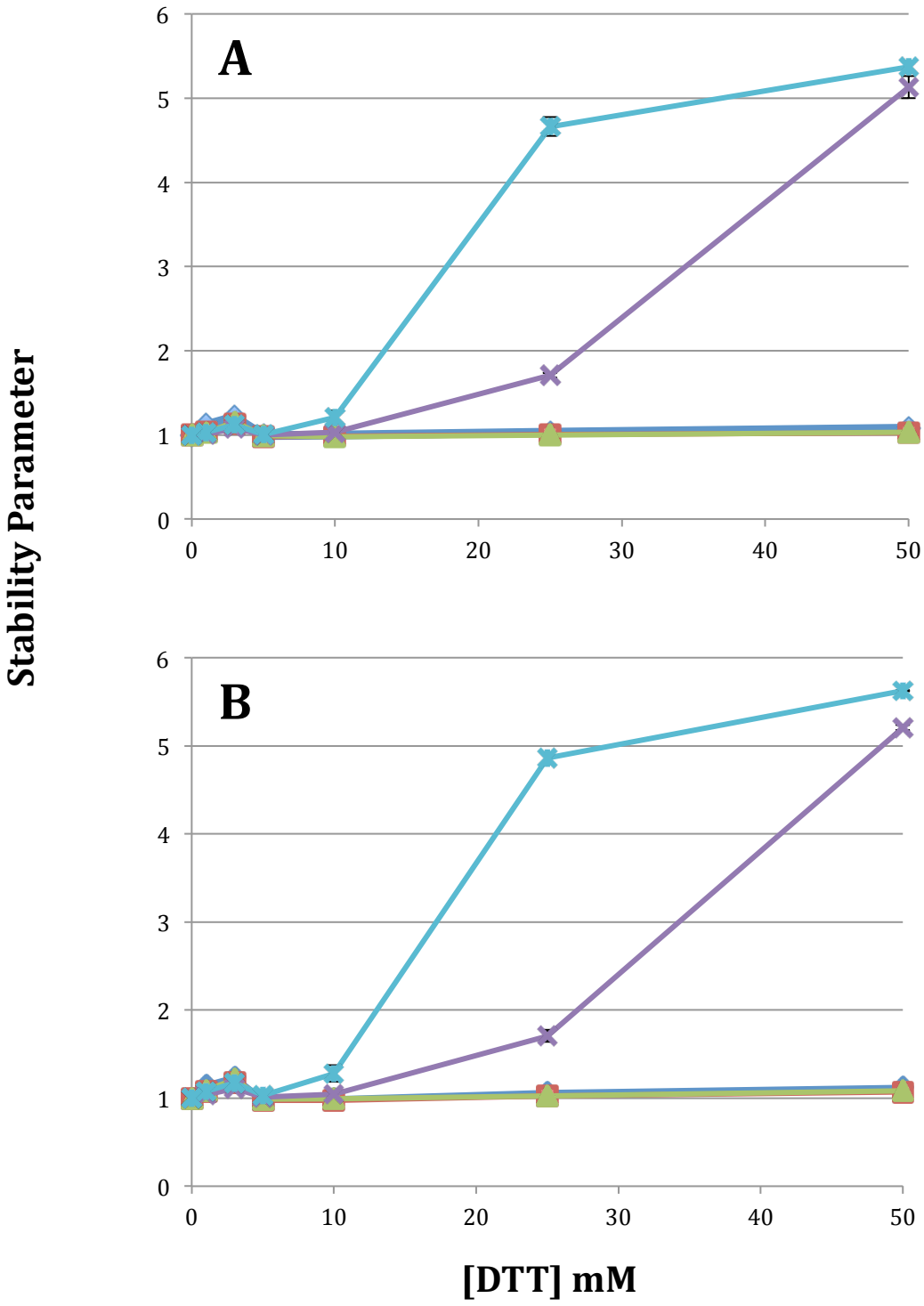

Figure 4.13 Calculated stability parameter for mix-matrix (A) and 1% N_3 (B) ligand shells in the presence of DTT. The stability parameter was taken at time points of 1 hour (♦), 3 hours (■), 6 hours (▲), 24 hours (×) and 48 hours (✳).

reactions with an unfunctionalised mix-matrix monolayer (Chen *et al.*, 2012), and is also consistent with the control data. At higher concentrations of DTT, i.e., 25 and 50 mM, nanoparticle aggregation, evidenced by the increase in the stability parameter was observed after 24 h, indicating that the monolayer was not stable. This increase in the stability parameter would be the result of ligand exchange.

4.2.2 Monovalent maleimide gold nanoparticles via copper-free click chemistry

The next goal was to demonstrate control over the number of the azide groups on the nanoparticle, with the aim of identifying an approach that would yield monovalent azide nanoparticles, and hence, monovalent maleimide functionalisation. This is essential for certain applications, such as single molecule biophysics. To determine the number of maleimide functional groups present on the nanoparticles after the click reaction, a pull-down of the nanoparticles functionalised with a biotinylated peptide was performed. Previously, it has been shown that the percentage of nanoparticles pulled down by affinity resins is proportional to the amount of a functional peptide or ligand present within the monolayer (Levy *et al.*, 2006; Duchesne *et al.*, 2008). In Lévy *et al.*, assuming a Poisson distribution for the number of ligand per nanoparticles, it was estimated that when 10 % of the nanoparticles are bound to resin the nanoparticle population will possess an average of 0.1 functional ligands per nanoparticle, which corresponds to 10 % of the nanoparticles possessing at least one functional ligand (with no more than 0.48% possessing two or more functional ligands) and 90% no functional ligand. Therefore, a titration was performed with gold nanoparticles by varying the molar percentage of azide ligands (1 – 0.1 %) in the ligand mix. The N_3NPs then underwent the click chemistry in the presence of a 100 μM DIBO functionalised with a maleimide (DIBO-Mal) for one

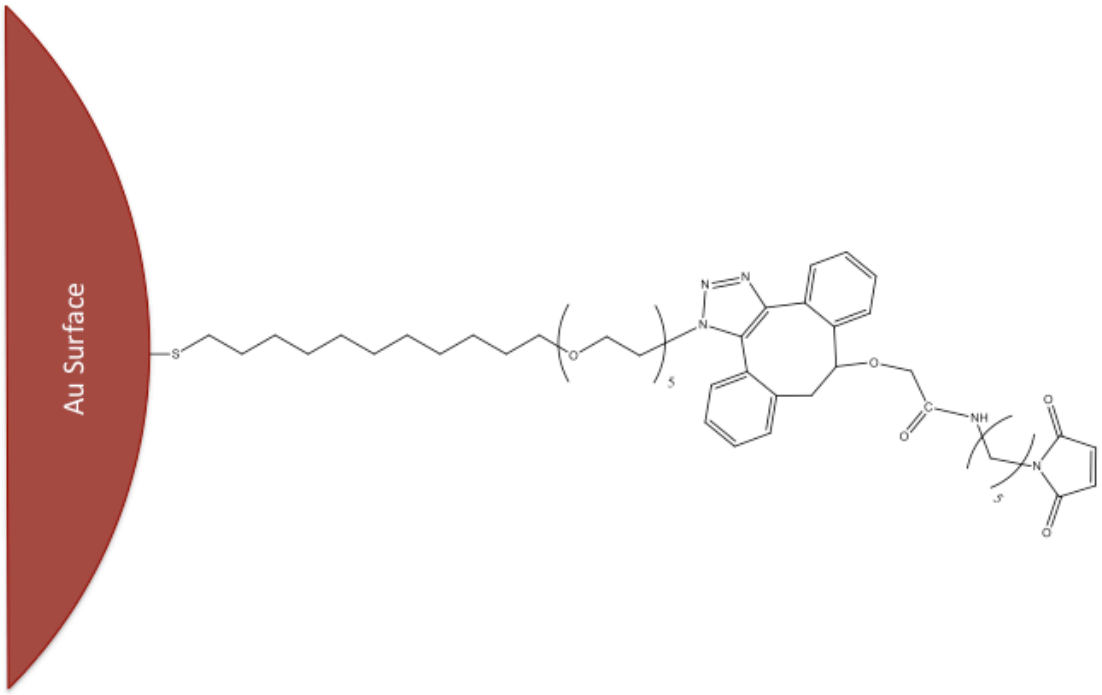

Figure 4.14 Skeletal structure of the final product of the click-chemistry reaction between the nanoparticle bound N_3 ligand and the DIBO-Mal strained cyclooctyne.

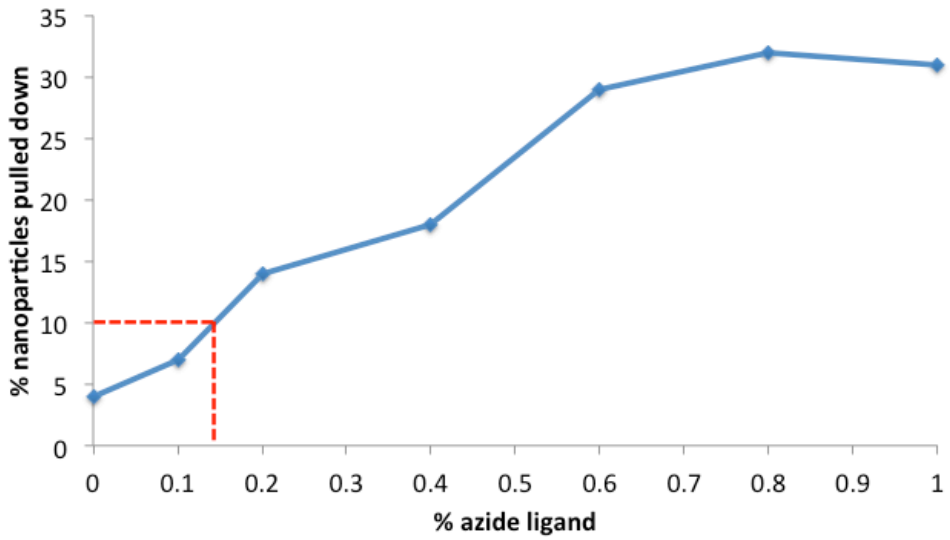

Figure 4.15 Titration of maleimide function by biotinylation. The dashed red line denotes concentration of azide ligand, and thus maleimide functionalisation, at which 10 % of nanoparticles are pulled down by StrepTactin Sepharose.

hour in the dark with mixing on a rotating wheel. This reaction generated maleimide functionality on any nanoparticles possessing azide ligands, and therefore generates DIBO-Maleimide functionalised nanoparticles nanoparticles (DIBO-Mal NPs; Figure 4.14). After removal of excess DIBO-Mal by Sephadex G-25 size-exclusion chromatography, with 1xTBS Tween-20 0.05 % (v/v) as the mobile phase, the nanoparticles were reacted unmodified with a biotinylated peptide (CVVVTGAAHHHHHH-K(biotin)-RKK) for 3 hours. This time was judged to be sufficient for Michael addition of the thiol on the cysteine of the peptide with the maleimide on the nanoparticle. After removal of excess peptide *via* another round of size-exclusion chromatography the nanoparticles were incubated with Strep-Tactin Sepharose (IBA solutions) overnight. The Strep-Tactin Sepharose will bind to the biotin present within the peptide with high affinity ($K_d \sim 100$ fM). Therefore, the quantity of nanoparticles bound to the resin will directly reflect proportion of biotinylated azide ligands within its monolayer. Thus, the amount of nanoparticles left in the supernatant would indicate the amount of particles pulled down when compared with the initial concentration of nanoparticles. The concentration of the nanoparticle in the supernatant was quantified by UV-vis spectrometry, and the percentage of nanoparticles pulled down onto the resin calculated (Figure 4.15). Nanoparticles at all concentrations of N_3 ligand were pulled down, with a decrease in the pull-down percentage from 0.6 % to 0.1% N_3 ligand. The concentration at which 10 % pull-down was achieved was 0.15 % (mol/mol, azide ligand: mix matrix ligand mix, Figure 4.15, dotted line). From this point, in order to generate monovalent maleimide functionalised nanoparticles, the initial N_3NPs were synthesized with 0.15 % (mol/mol) azide ligand in their monolayer. It is important to note that this titration only holds for the current batches of ligands and nanoparticles. If either constituent

were to change then the titration would have to be repeated, as not all batches of nanoparticles and ligands are identical.

4.2.3 Conjugation of biomolecules to monovalent maleimide nanoparticles via Michael addition reactions

Having generated the monovalent DIBO-Mal NPs described in the previous section, the next step was to attempt their conjugation to FGF-2 and maleimide modified oligosaccharides. For Michael addition to occur with the maleimide on the DIBO-Mal NP a free thiol is required. Therefore, the reaction should proceed in the same fashion as the reaction with the D-PEG/D-Mal NPs (Section 4.1.2). Hence, the biomolecules selected for the conjugation reactions are identical to those used for the D-PEG/D-Mal NPs, i.e., FGF-2 and maleimide modified heparin-derived hexa- and dodecasaccharides.

FGF-2 was incubated at a 3.5 times molar excess over DIBO-Mal NPs with mixing for 3 hours on a rotating wheel. The mixture was then purified *via* heparin agarose affinity chromatography. Images of the heparin agarose affinity columns can be seen in Figure 4.16. Nanoparticles bearing no maleimide functionality, i.e., a mix matrix monolayer, when incubated with FGF-2 do not bind to the column (Figure 4.16A). This is also the case when DIBO-Mal NPs that have not been incubated with FGF-2 are passed through the column (Figure 4.16B). When the DIBO-Mal NPs are incubated with FGF-2 protein the pink colour of the gold nanoprobe is seen on the heparin agarose column (Figure 4.16C). The nanoparticles can be eluted with 2 M NaCl, which is sufficient to elute FGF-2 from heparin affinity columns.

A maleimide will readily undergo Michael addition with other thiol functionalised molecules. If DIBO-Mal nanoparticles are reacted with an excess of

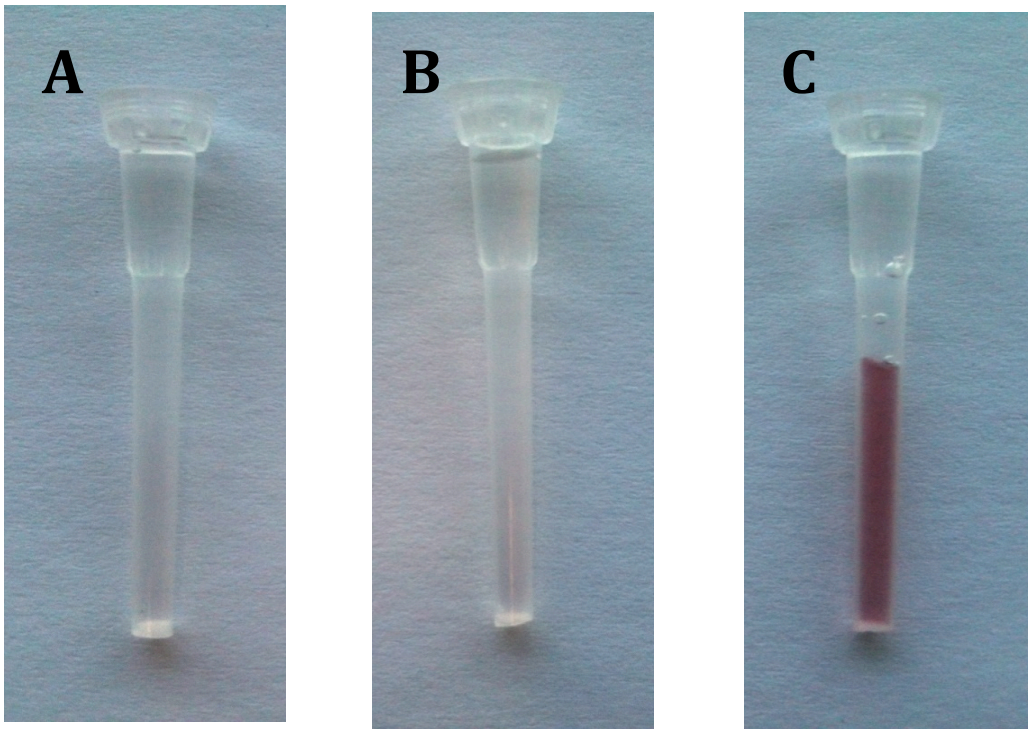

Figure 4.16 Purification of DIBO-FGF-2 NPs via affinity chromatography with heparin agarose. (A) Mix-matrix nanoparticles incubated with an excess of FGF-2 protein, (B) DIBO-Mal nanoparticles and (C) DIBO-Mal nanoparticles incubated with an excess of FGF-2 protein.

dithiols, e.g., DTT, then the resulting nanoparticle will have thiol functionality (Section.4.1.2; Figure 4.7). Hence, DIBO-Mal NPs were incubated with an excess of 1 mM DTT for 1 hour to generate thiol functionality, after which excess DTT was removed *via* Sephadex G-25 size-exclusion chromatography with 1xPBS Tween-20 0.05 % (v/v) as the mobile phase. To see if indeed thiol nanoparticles (DIBO-SH NPs) were generated, they were reacted with small oligosaccharides derived from heparin modified with a maleimide: hexasaccharide (Section 4.1.3), and a dodecasaccharide, a longer oligosaccharide (Gift from Nina Azmi; Azmi, PhD thesis, University of Liverpool, 2012). Nanoparticles with a non-functionalised mix monolayer incubated with the hexa- or dodecasaccharide did not bind to the DEAE Sepharose (Figure 4.17 A and D) and neither did DIBO-SH NPs in the absence of the hexa- and dodecasaccharide (Figure 4.17 B and E). When DIBO-SH nanoparticles had been incubated with the hexa- or dodecasaccharides for 3 hours with mixing, and subsequently used for anion exchange chromatography, nanoparticles bound to the DEAE-Sepharose, indicated by a pink colour at the top of the column (Figure 4.17 C and F). Thus, nanoparticles only bind to the resin when the Michael addition reaction has occurred between DIBO-SH NPs and the maleimide modified oligosaccharides. The hexa- or dodecasaccharides NPs can be eluted from DEAE-Sepharose with 2 M NaCl. The nanoparticles were subsequently buffer exchanged into 1xPBS Tween-20 0.05 % (v/v) *via* multiple centrifugation steps (35 mins at 13000 rpm), allowing removal of excess hexa- or dodecasaccharides.

This work shows that both FGF-2 protein and maleimide hexa- and dodecasaccharides were successfully conjugated to DIBO-Mal NPs. With the control over the number of maleimide groups on the nanoparticle established, these nanoparticle conjugates are, therefore, stoichiometrically coupled at a ratio of one

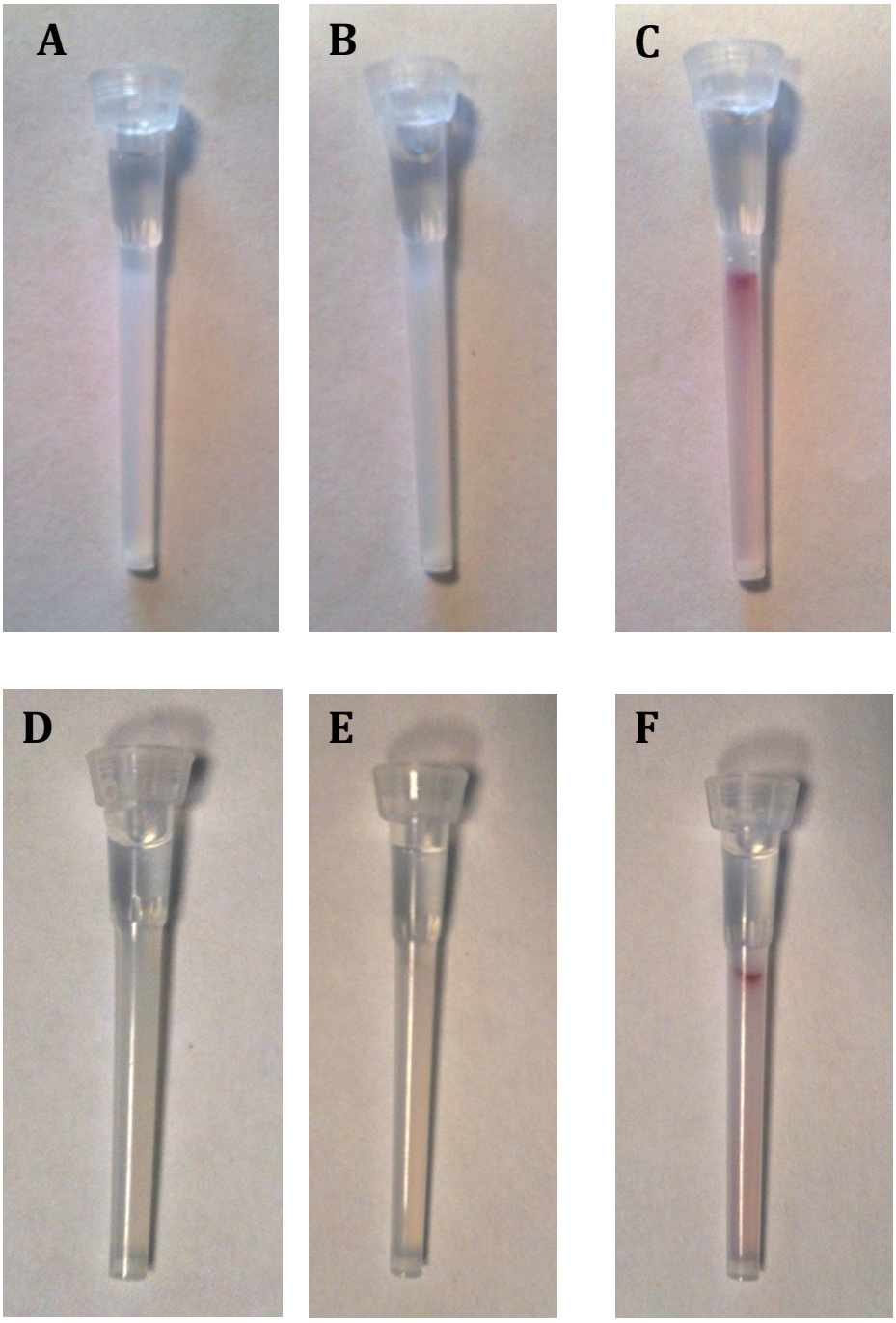

Figure 4.17 Purification of DIBO-hexa- and dodecasaccharide NPs *via* anion exchange chromatography on DEAE-Sepharose. Mix-matrix nanoparticles incubated with an excess MBPH functionalised (A) hexa- and (D) dodecasaccharide. SH NPs on DEAE-Sepharose control for both (B) hexa- and (E) dodecasaccharide experiments. SH NPs incubated with an excess of MBPH functionalised (C) hexa- and (F) dodecasaccharide purified on DEAE-Sepharose.

nanoparticle to one biological molecule. This will enable single nanoparticle biophysics experiments, using photothermal microscopy, to probe the biological interactions of these molecules. Some proof of principle experiments using the conjugates described above will be examined in the next section.

4.3 Covalent biomolecule-nanoparticle conjugates for single molecule biophysics experiments

4.3.1 Cell Imaging with DIBO-FGF-2 nanoparticle

The interaction of FGF-2 with its cell surface HS co-receptor is fundamental to its biological function. Previously, nanoparticle labelled FGF-2 proteins have been utilized for single molecule photothermal microscopy to probe this interaction on cells at the single molecule level. In this work, the nanoparticles with a Tris-NTA moiety were conjugated to the hexa-histidine tagged FGF-2 protein, through the non-covalent coordination of Ni^{2+} ions (Duchesne *et al.*, 2012). Here, the conjugation of nanoparticle (DIBO-Mal NP) and FGF-2 protein (unmodified, i.e., no tags) was used to see if the same labelling could be achieved. Therefore, fixed Rama 27 fibroblast cells were incubated with 220 pM of purified DIBO-FGF-2 NPs, in accordance with previous FGF-2 photothermal experiments (Duchesne *et al.*, 2012). After washing, the sample was mounted in Krebs ringer buffer and the cells were imaged using the photothermal microscope (Figure 4.18). When incubated with DIBO-FGF-2 NPs, gold nanoparticles are detected bound to the surface of the cell (Figure 4.18A and B). Movement of the DIBO-FGF-2 NPs is also seen within the image, indicated by the presence of a streak (white box, Figure 4.18B). This behaviour is very similar to that previously seen by Duchesne *et al.* for FGF-2 when bound to cellular HS. Therefore, it appears in this simple experiment that the covalent FGF-2-nanoparticle conjugate, DIBO-FGF-2 NP, could be used for similar biophysics experiments to those described

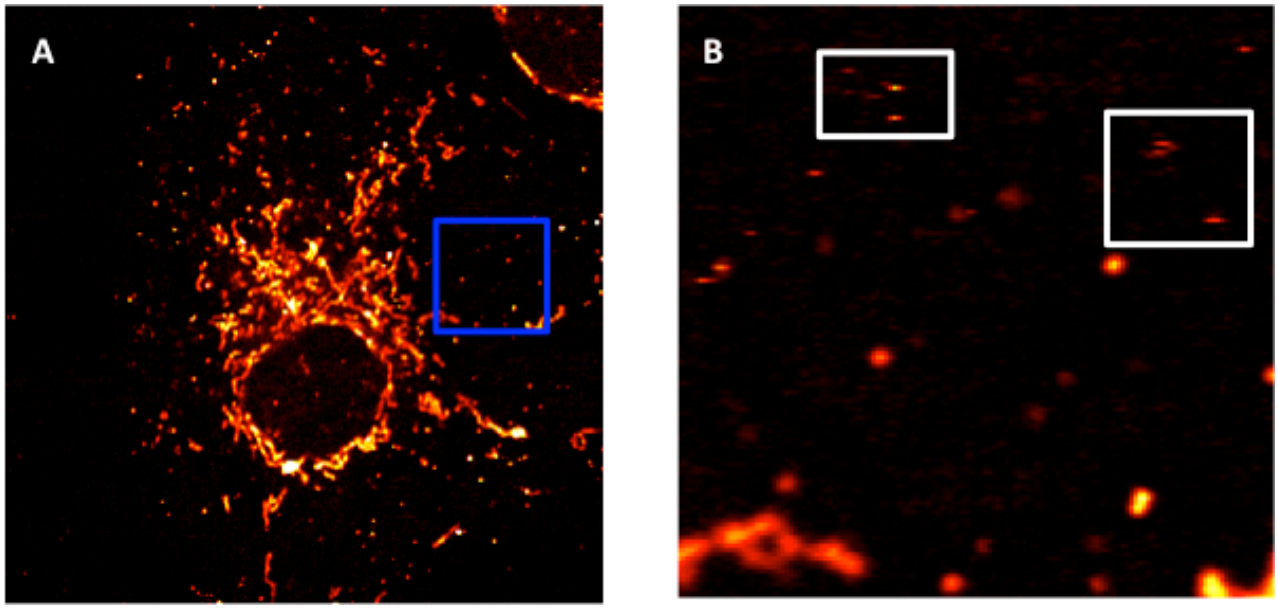

Figure 4.18 DIBO-FGF-2 NPs on RAMA 27 cells. (A) 70 x70 µm image of Rama 27 cells incubated with 220 pM of DIBO-FGF-2 NPs. (B) Zoomed 10 x10 µm image of the area in A (blue box). Streaking attributed to diffusion of DIBO-FGF-2 NPs is marked with white rectangles.

in Duchesne *et al*., without the potential for exchange of the nanoparticle for an endogenous histidine-rich protein.

4.4 Conclusions from Chapter 4

Nanoparticles can be successfully passivated with a monolayer based on disulphide ligands. This monolayer is stable to ligand exchange and the disulphide ligands can be exploited to incorporate a maleimide group in a single ligand capping reaction step. The maleimide functionalised nanoparticles were shown to be a versatile platform for the conjugation of protein, FGF-2, and the generation of particles presenting a single free reactive thiol (using DTT). The thiol functionalised nanoparticles were shown to be able to undergo a further Michael addition reaction with a maleimide functionalised hexasaccharide, to give oligosaccharide functionalised nanoparticles. However, the D-PEG ligand and, thus, the ligand capped nanoparticles appeared to acquire a negative charge with time. This prevented the separation of nanoparticle-oligosaccharide conjugates by anion-exchange chromatography. Moreover, given the large number of extracellular proteins that bind HS, negatively charged nanoparticles would be likely to exhibit considerable non specific binding, e.g., to heparin binding proteins, as has been demonstrated for peptide capped nanoparticles (Jeong *et al.*, 2008).

Therefore, a new approach exploiting copper-free click chemistry was taken. The nanoparticle exploited the exceptional stability to ligand exchange of an existing monolayer, but allowed incorporation of an azide group for click chemistry with strained cyclooctynes (e.g. DIBO-Mal). This allowed the incorporation of maleimide groups at the nanoparticle surface, and the number of these groups was shown to be controllable. Subsequently, the covalent conjugation of both FGF-2 protein and maleimide-modified oligosaccharides, hexa- and dodecasaccharides, was achieved, in a stoichiometric manner (i.e., 1:1). The resulting FGF-2 nanoparticle conjugates were used for some exemplar single molecule experiments with the photothermal

microscope, and were shown to be applicable for such experiments.

5. Probing the organization of the extracellular matrix with FGF nanoparticle conjugates at the single molecule level

Photothermal microscopy has been utilized in a variety of experiments for the detection of single gold nanoparticles *in vitro* and on cells. This technique has allowed high signal-to-noise detection of protein-nanoparticle conjugates. This has led to the beginnings of new single molecule biophysics approaches to analyse complex biological problems. For example, photothermal tracking has been employed to probe the dynamics of number of extracellular proteins, such as AMPA receptors and FGF-2 (Lasne *et al.*, 2006; Duchesne *et al.*, 2012). Recently, a selection of different proteins (both intra- and extracellular) has been targeted through antibody labelled nanoparticles that bind GFP (Leduc *et al.*, 2013). By expressing proteins labelled with GFP, nanoparticle labelling has allowed the imaging of kinesins, integrins and microtubule binding EB3 proteins. These experiments not only revealed the localisation of all the proteins mentioned above, but also allowed accession to previously unknown diffusion behaviour of these proteins.

The rationale for conducting such single molecule experiments to elucidate the full gamut of a biomolecule's function has been discussed in Chapter 1 Section 1.1. In this chapter, we report single molecule experiments performed on members of the FGF family. The two chosen are the most widely studied; FGF-2, which has been observed using photothermal microscopy before (Duchesne *et al.*, 2012) and a member of the same FGF subfamily, FGF-1, imaged here at the single molecule level

for the first time. The experiments use the nanoparticles (Chapter 4 Section 4.2.4) and techniques (Chapter 3 Section 3.8) developed in this thesis to determine the binding behaviour of FGFs to a proxy for heparan sulfate, i.e., a heparin-derived dodecasaccharide oligosaccharide, to try to determine whether binding of FGF-2 is indeed cooperative, as has been suggested (Goodger *et al.*, 2008; Saxena *et al.*, 2010). Then, measurements are made in the more challenging system of the pericellular matrix of cells using PhRICS to determine if PhRICS allows access to a greater range of diffusion behaviour than single particle tracking, since the latter's dynamic range is limited to slower diffusion.

5.1 Binding of FGF-2 to oligosaccharides in solution: Is there evidence for cooperativity?

The binding of FGF-2 molecules to its co-receptor, heparan sulfate, is a mandatory step for the activation of the FGFR and, thus, a biological signalling response. The binding of FGF-2 by HS is thought to be the initial step, whereby the bound FGF-2 is then presented to the receptor at the cell surface (Yayon *et al.*, 1991; Ornitz *et al.*, 1992). A key question is how HS is able to both bind and facilitate the formation of the multimeric receptor complex. One view, supported by recent work, is that the binding and movement of FGF-2 molecules in the extracellular matrix is governed by HS, which may provide means of titrating FGF-2 into the receptor signalling system (Zhu *et al.*, 2010; Duchesne *et al.*, 2012). Previously, the dimerization of the FGFR, a pre-requisite for the activation of its tyrosine kinase, and so signalling (Chapter 1 Section 1.2.1), has been suggested to depend on the dimerization of the FGF ligand by HS. This was first proposed in 1992 in the context of the potential of heparin-derived oligosaccharides to support the dimerization of FGF-2 ligand in solution (Ornitz *et al.*, 1992). It was also shown that conditions that

did not favour the oligomerization of FGF-2 ligand, i.e., an excess of heparin oligosaccharide, in turn led to the loss of receptor activation, presumably by the stabilization of monomeric FGF-2. The addition of more unlabelled FGF-2 ligand was shown to increase the level of labelled FGF-2 binding to the receptor but also compete for binding (Ornitz *et al.*, 1992). The interpretations of these data were that either positive cooperativity existed, or that the oligosaccharide was able to stabilize FGF-2 ligand dimers. The cooperativity of FGF-2 binding to oligosaccharides has been suggested more recently (Goodger *et al.*, 2008; Saxena *et al.*, 2010). Goodger *et al.*, used size-exclusion chromatography to provide evidence that FGF-2 dimers could be formed in the presence of a heparin-derived dodecasaccharides, even in the presence of a molar excess of the oligosaccharide. Saxena *et al.* demonstrated pronounced positive cooperativity *via* a titration of FGF-2 against a smaller oligosaccharide, an octasaccharide, using NMR. It was observed that the measured affinity for the first FGF-2 protein was higher than that required to recruit the second FGF-2 protein into the dimer (K_D 100 nM and 5.8 nM, respectively).

The dimerization of other FGFs, e.g., FGF-1, has also been proposed as a mechanism for the regulation of its signaling. Evidence for this comes from the structure of a co-crystal of FGF-1 with a heparin-derived decasaccharide, in which two FGF-1 proteins were observed to be dimerized by the oligosaccharide *in trans*, with an absence of protein-protein contacts (DiGabriele *et al.*, 1998). However, this proposed structure is different from that seen in the presence of the ectodomain of FGFR2 IIIc. Here, both FGF-1 molecules are again linked by the decasaccharide in the absence of protein contacts, however, their conformation in relation to the saccharide chain is quite different (Pellegrini *et al.*, 2000). The role of cooperativity in the formation of FGF-1 dimers on dodecasaccharides has also been supported by

biochemical evidence (Robinson *et al.*, 2005; Brown *et al.*, 2013). Size-exclusion chromatography of a 2:1 ratio (FGF-1: dodecasaccharide) resulted in a single shifted peak, corresponding to the formation of single complex, i.e. two FGF-1 molecules to one dodecasaccharide. Cooperativity of this interaction was supported by the apparent formation of the dimer complexes in both equimolar and in the presence of a 4 times excess of dodecasaccharide over FGF-1 (Robinson *et al.*, 2005). This has since been further corroborated by isothermal titration calorimetry measurement by the same group, were FGF-1 binding was shown to be facilitated by positive cooperativity to octasaccharides and longer (Brown *et al.*, 2013). The FGF-1 is thought to bind in a displaced *trans*-dimeric manner on a single oligosaccharide, whereby binding to the FGFR can occur to form the signalling complex.

To investigate proposed cooperativity of FGF-2 binding to heparin, a heparin derived dodecasaccharide (a gift from Yassir Ahmed, University of Liverpool) and nanoparticle labelled FGF-2 (Chapter 4 Section 4.2.3) was used as the probe in PhRICS experiments in solution. Here, the molar ratio of FGF-2 nanoparticle to heparin-derived dodecasaccharide was varied; 1:3, 1:1, 1:0.3. For comparison, PhRICS measurements were also taken solely of the FGF-2 nanoparticle conjugate in the absence of any dodecasaccharide. The reactions were carried out in 1xPBS buffer, and then diluted 10 times into a 50 % glycerol solution (v/v, final concentration) in 1xPBS buffer. The final concentration of FGF-2 nanoparticle conjugate in all experiments was 5 nM. This is over 100-fold higher than the FGF-2 concentration required for maximal stimulation of cell growth (~17 pM) (Smith *et al.*, 1984; Fernig *et al.*, 1990; Zhu *et al.*, 2010), but still 10-fold or more lower than concentrations of FGF-2 that elicit a signalling response that does not lead to cell

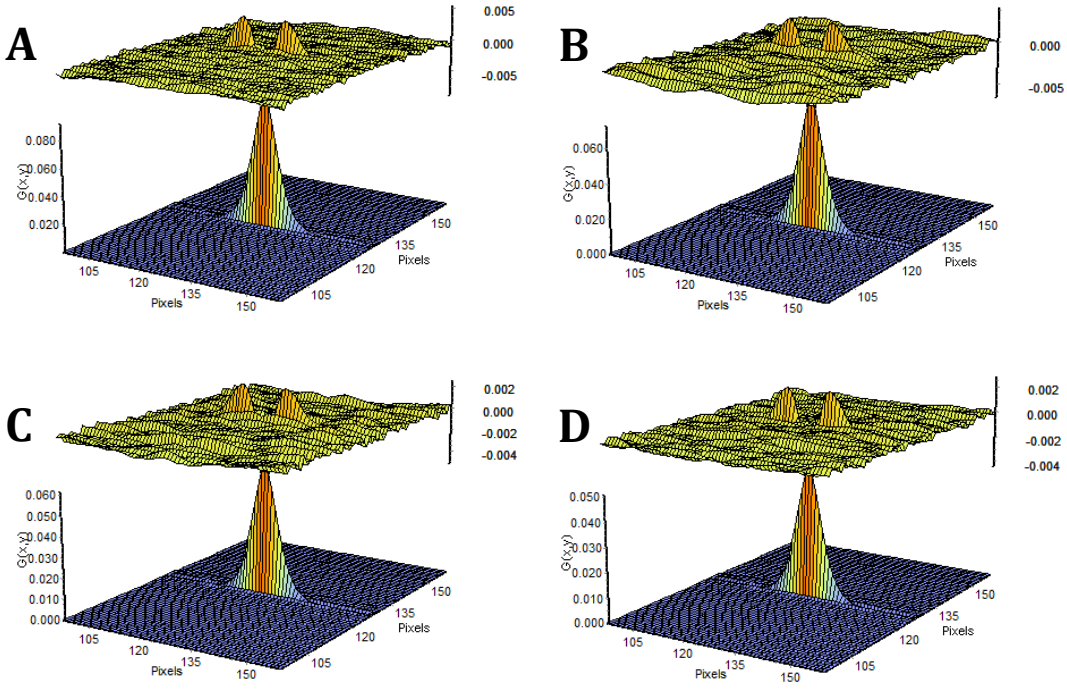

Figure 5.1 Surface plots for PhRICS spatial correlations of 5 nM FGF-2 nanoparticles incubated with a molar ratio of dodecasaccharide (FGF-2:dodecasaccharide). (A) 1:0, (B) 1:3, (C) 1:1 and (D) 1:0.3. The surface plots are fitted with Equations 3.8 and 3.9 with the residuals from fitting of the surface (top axes).

Table 5.1 Diffusion coefficient as measured by PhRICS for FGF-2 nanoparticles in different molar ratios of dodecasaccharide (n = 1)

Molar ratio of FGF-2:dodecasacchride	Diffusion coefficient from PhRICS ($\mu m^2/s$)
1:0	5.6
1:3	5.3
1:1	4.5
1:0.3	4.6

division (Zhu *et al.*, 2010). For the FGF-2 nanoparticle conjugate in 50 % glycerol:1xPBS (v/v) the measured diffusion coefficient was 5.6 $\mu m^2/s$ (spatial correlation is presented in Figure 5.1A, whereas the diffusion coefficient obtained from the fit is found in Table 5.1). This gives a measured hydrodynamic diameter of 13.0 nm (calculated using Equation 3.5). Although the size of the nanoparticle core used to label the FGF-2 is 9.3 nm and has previously been measured by PhRICS to have a hydrodynamic diameter of 9.8 ± 0.5 nm, this increase in diameter is expected for a capped and protein functionalised nanoparticle. The addition of the ligand shell of a nanoparticle will add 1-2 nm to the measured diameter (Octeau *et al.*, 2009). The addition of a single FGF-2 protein (c.a., diameter approximately 3.5 x 4.0 nm), and the likely substantial ion cloud (FGF-2 has a pK_a of 9.6) will too contribute to an increased diameter. This diffusion coefficient will be used as a benchmark for the interaction of FGF-2 with dodecasaccharide.

In an excess of dodecasaccharide, i.e., a molar ratio of three oligosaccharides to one FGF-2, the diffusion coefficient decreased, with a value of 5.3 $\mu m^2/s$ (Figure 5.1B; Table 5.1). It seems unlikely that no FGF-2 nanoparticle:dodecasaccharide complexes were formed, since the K_d is of the order of 10^{-8} to 10^{-7} M (Delehedde *et*

al., 2002), and the excess of dodecasaccharide is likely to drive the binding reaction towards the formation of complexes. Thus, the relatively small effect on the average diffusion constant is slightly puzzling. However, it should be noted that the complex might not have a significantly different hydrodynamic diameter to that of the FGF-2 nanoparticle conjugate for a number of reasons. First, the oligosaccharide is relatively small. If it were a rigid rod, it would be of the order of 1 nm x 1 nm x 5 nm. Thus, is would only add a small amount of "width" to the FGF-2 nanoparticle. Moreover, it is now well established that the interaction of FGFs, including FGF-2 with the sugar increases the protein's rigidity (e.g., Xu *et al*., 2013), which would decrease the hydrodynamic diameter of the protein. Finally, the charge neutralization resulting from the formation of the complex (pK_a will drop from 9.6 to closer to neutral) may reduce the ion cloud around the complex. Therefore, a small change in the diffusion coefficient (~ 7 % decrease) and thus an increase in the hydrodynamic diameter (~ 1 nm), could be counterbalanced by the effects described above, although the increase is certainly indicative of interaction of FGF-2 with the dodecasaccharide.

In contrast, the measurement for an equimolar (1:1) mixture of FGF-2 nanoparticle and dodecasaccharide led to a decrease in the measured diffusion coefficient to 4.5 $\mu m^2/s$ (Figure 5.1C; Table 5.1). This decrease in diffusion speed is unlikely be the result of a greater number of FGF-2 molecules forming complexes with the dodecasaccharides that observed at a 3:1 ratio of sugar to protein. Thus a more likely explanation for the greater decrease in measured diffusion coefficient compared to that seen at the 3:1 ratio is the formation of FGF-2 dimers on the dodecasaccharide, so resulting in a 19 % decrease in the measured diffusion coefficient. When the FGF-2 is in an excess over dodecasaccharide (1:0.3) a slight increase of the diffusion coefficient, to 4.6 $\mu m^2/s$ is seen (Figure 5.1D; Table 5.1).

This would be expected if binding sites on the dodecasaccharide were limited, such as in concentration or by the number of binding sites themselves. FGF-2 requires N-sulfated glucosamine and iduronate-2-sulfate for binding (Ornitz *et al.*, 1992). Thus, FGF-2 is unlikely to bind an oligosaccharide in *trans*, but it could bind *in cis*, due to the disposition of these sulfate groups along the chain, given that a hexasaccharide is sufficient for binding (Faham *et al.*, 1996), then a dodecasaccharide could accommodate at most two FGF-2 *in cis*. Moreover, to produce a dodecasaccharide from heparin heparinase digestion is used, which cleaves sugars at IdoA. This means that there is likely to be enrichment centrally, in terms of the dodecasaccharide structure, of GlcN and GlcNA, which could eliminate the ability of the dodecasaccharide to facilitate the binding of a second FGF-2. This would mean that due to the heterogeneity of the dodecasaccharide structures present than there may be a mixture of single FGF-2 nanoparticle conjugates bound to single sugar as well as dimers of FGF-2 to a single sugar. Therefore, as PhRICS measures all nanoparticles, irrespective of binding/oligomerization state on the dodecasaccharide, then this population of singly bound FGF-2 nanoparticles will contribute to a greater measured diffusion coefficient. The percentage decrease in the diffusion coefficient observed from FGF-2 in the absence or excess of dodecasaccharide (5.6 $\mu m^2/s$) to when the FGF-2 is in an equimolar ratio to dodecasaccharide (4.5 $\mu m^2/s$) is approximately 18 %. The formation of FGF-2 nanoparticle dimers in contact with a dodecasaccharide will most likely give rise to a 'dumbbell' of nanoparticles. However, Equation 3.5 does not hold for objects that are not spherical, and this must be taken into account. If an average diameter is taken of the axial and lateral diameters of a nanoparticle 'dumbbell'; for example, a dumbbell containing two 13 nm nanoparticles, then the average diameter is approximately 17.3 nm (accounting for the major, minor and

transverse axes). When calculating the diffusion coefficient using this value, then the expected decrease for a solution of exclusively dumbbells or dimers is 25 %. Therefore, even when FGF-2 is in an equimolar concentration of dodecasaccharide, the solution is not exclusively populated with dimers. This suggests that either there may be an equilibrium between the free FGF-2 nanoparticles, the monomeric complex and the dimer in solution. Thus, the analysis measures both single FGF-2 nanoparticles unbound and bound to the dodecasaccharide, but also measures the presence of FGF-2 nanoparticle dimers on dodecasaccharide.

In a cooperative interaction, a first binding event results in conformational changes that increase the affinity of the next binding events. If the interaction of FGF-2 with dodecasaccharide were cooperative, one would expect a substantial number of FGF dimers when the FGF-2 was in a 3-fold molar excess, mainly dimers at a ratio of 1:1 and only dimers when the FGF-2 was in 3-fold molar excess. Therefore, cooperativity of FGF-2 binding to the heparin-derived dodecasaccharide is not supported by the present PhRICS measurements. The evidence for the formation of dimers of FGF-1 and FGF-2 on heparin-derived oligosaccharides as short as an octasaccharide and a cooperative mechanism for their formation has been discussed earlier in this section (DiGabriele *et al.*, 1998; Robinson *et al.*, 2005; Saxena *et al.*, 2010; Brown *et al.*, 2013). The formation of FGF-1 dimers shown by X-ray crystallography has been shown in two papers (DiGabriele *et al.*, 1998; Pellegrini *et al.*, 2000), but not in other crystallographic studies (Faham *et al.*, 1996; Schlessinger *et al.*, 2000). The structures of the dimers presented in DiGabriele *et al.* in isolation are different to those identified by Pellegrini *et al.* in the presence of the receptor. There are significant differences in both structures as to the orientation of FGF-1 proteins to the oligosaccharide. Therefore, the formation of the FGF-1 dimer in the

presence of only the oligosaccharide, presented in DiGabriele *at al.*, may be a crystal-packing artefact. Similarly, the dimer observed in the co-crystal with the receptor extracellular domain observed by Pellegrini *et al.* may also be the result of crystal packing. It should be noted that in this structure the receptor has an artefactual *cis-trans* proline isomerization. Moreover, in FGF ligand-receptor extracellular domain-oligosaccharide co-crystals, the two different arrangements of the components asymmetric, Pellegrini *et al.*, and symmetric, Schlessinger *et al*., are present in the same unit cell, suggesting that at least one of these is a crystal packing artefact. Biochemical data have been used to provide evidence for the oligomerization, and positive cooperativity of the binding of FGF-1 and of FGF-2 to dodecasaccharides (Robinson *et al.*, 2005; Goodger *et al.*, 2008; Brown *et al.*, 2013). Here, the formation of dimers of FGF seems to be demonstrated quite conclusively. However, it is worth noting that the concentration of the FGFs and probably the dodecasaccharide are very different from those encountered physiologically. The concentrations used are all of the order of several μM, due in part the detection limit of size-exclusion chromatography and of the necessity in isothermal titration calorimetry to saturate all binding sites. If one considers the situation *in vivo* in, for example, a morphogen gradient, then at high end of the gradient FGF concentrations will be of the order of 10^{-8} M to 10^{-9} M and at the low end 10^{-10} M to 10^{-11} M (Zhu *et al.*, 2010). The concentration of FGF-2 in resting mammary gland (one of the few measurements made *in vivo*) is of the order of 50 ng/mL, or ~ 3 nM (Barraclough *et al.*, 1990). Thus, concentrations in the range of μM are unlikely to be attained physiologically. While HS is abundant on the cell surface and in the extracellular matrix, the concentration of free binding sites for an FGF is also unlikely to reach such high concentrations (Fernig *et al.*, 1992; Duchesne *et al.*, 2012). Therefore, it seems

unlikely that μM concentrations used to observe cooperative effects would be physiologically relevant. However, it should be noted that at the molecular scale, local concentrations might be much higher, as evidenced by the heterogeneity of the distribution of FGF-2 in pericellular matrix at the single molecule level (Duchesne *et al.*, 2012).

A second issue, which is relevant to both the isothermal titration calorimetry and size-exclusion chromatography measurements, is that both FGF-1 and FGF-2 possess three heparin-binding sites (Ori *et al.*, 2009; Xu *et al.*, 2012). The secondary binding sites are of lower affinity (2 to 5 orders of magnitude) than the canonical site (Kinsella *et al.*, 1998), but once the canonical site engages the sugar, the secondary sites clearly do so as well (Ori *et al.*, 2009; Xu *et al.*, 2012). Optical biosensor experiments target just the canonical site and measure affinities of the order of 10^{-8} M (Delehedde *et al.*, 2002; Xu *et al.*, 2012), whereas isothermal titration calorimetry has to saturate all binding sites. Therefore, the interpretation of such experiments and the two phase binding interpreted as cooperativity may instead result simply from complexes re-arranging to release sugars bound to low affinity secondary sites so that they interact with canonical sites in the FGF, as the latter's concentration changes.

In conclusion, the evidence for dimerization of FGFs on oligosaccharides is not entirely secure and cooperativity may be dependent on the experimental conditions and the presence of secondary binding sites for the sugar on the FGFs. The present data, carried out roughly in the middle of the physiological range of FGF concentrations indicate that dimerization and cooperative binding seem unlikely.

5.2 Photothermal imaging of live cells: Label-free imaging of mitochondria

The precise detection and localization of single gold nanoparticles by photothermal imaging is a requisite before any single molecule biophysics can be performed. Such detection relies largely on the signal-to-noise with which a gold nanoparticle is detected (Boyer *et al.*, 2002). This is particularly important when the experiment moves from low background samples, such as purified components in solution (Section 5.1) and films at the surface of a coverslip, to a cell (Cognet *et al.*, 2003). It has been demonstrated previously that photothermal microscopy can detect mitochondria without need for a label (Lasne *et al.*, 2007). Why mitochondria elicit a photothermal signal has been investigated, although no candidate molecular complex or protein could be identified (Lasne *et al.*, 2007).

The background from mitochondria often goes unmentioned in many papers that focus on the detection of single nanoparticles, and hence single proteins on or in cells. This is mainly due to the cell types used for the experiments and the high signal to noise with which the nanoparticle is detected. The cells often have a low profile in in the z-direction, or are, colloquially, "flat". This morphology is convenient from the point of view of photothermal microscopy. The localization of the mitochondria is perinuclear, exemplified by the photothermal image of Rama 27 fibroblasts (Figure 5.2A), and encloses the less bright nucleus. However, not all biology occurs on or within "flat cells", for example, epithelial cells are often columnar and they usually form islands that give the cells a more prolate three-dimensional morphology. Thus, the cells become "tall", extending 3-4 μm in the z-axis, and are characterized by tight

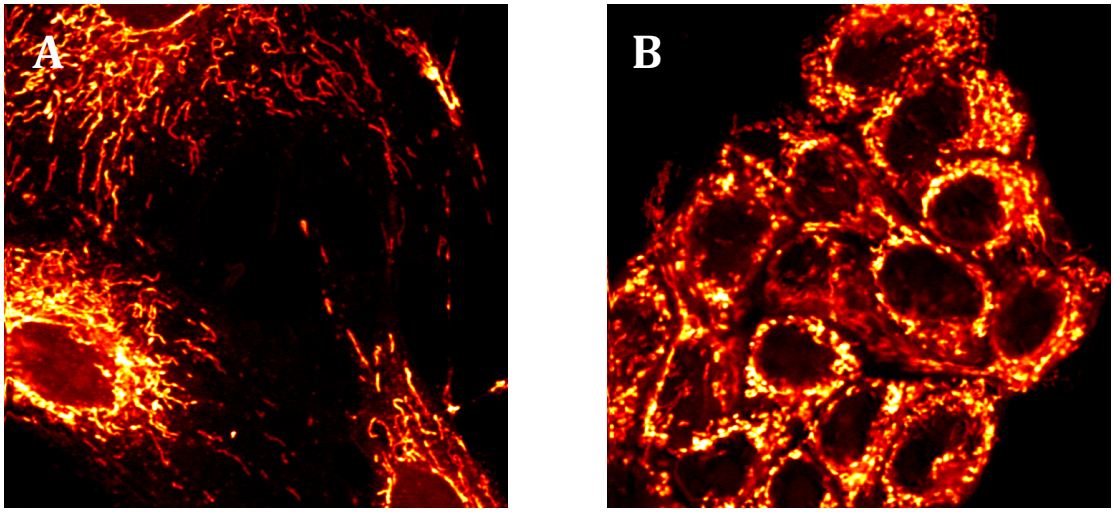

Figure 5.2 Photothermal image of the mitochondrial background in Rama 27 fibroblast cells (A) and compared with MCDK epithelial cells (B).

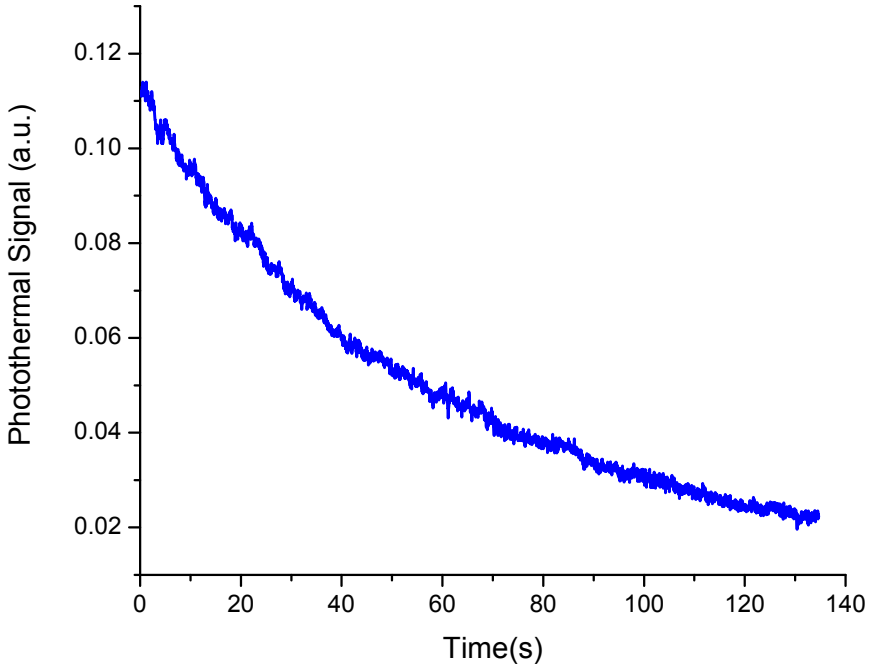

Figure 5.3. Photothermal signal of a single mitochondrion in a Rama 27 fibroblast under continuous photothermal excitation.

extracellular junctions with neighboring cells. A photothermal image of some Madin Darby canine kidney cells (MDCKs; a gift from Bahram Ibrahimi, University of Liverpool) is presented in Figure 5.2B. Almost the entire MDCK cell appears to give a photothermal signal. The only areas where the background is low (appears black) are the nuclei, and at some of the cell-cell junctions (Figure 5.2B). In contrast although the mitochondrial signal is still present, Rama 27 fibroblasts have a large area of cytoplasm that is free of photothermal signal and would be ideal for detection of single nanoparticles. This means that photothermal microscopy may be limited to some cell types. For the remainder of the chapter the experimental work will focus on Rama 27 fibroblast cells.

Even though Rama 27 cells exhibit much less photothermal background due to the cell morphology, and thus the distribution of mitochondria, it is still important to be mindful of the background signal. The photothermal signal from the mitochondria will bleach over time when under constant excitation (Lasne *et al.*, 2007). Therefore, mitochondria from a fixed Rama 27 cell were illuminated using the photothermal set-up, and the signal acquired over time (Figure 5.3). The signal immediately begins to decrease over a few seconds, until it reaches a level almost equal to the background level after 120 seconds. Although the signal is attenuated by the continuous excitation, and, therefore, becomes bleached, this would not be a recommended way to attenuate the signal for imaging, as this occurs on a timescale approximately 3 orders of magnitude greater than the time mitochondria would be under excitation for in a typical photothermal image (i.e., pixel dwell time ~ < 10 ms).

One way to attenuate the signal seen from mitochondria, and to increase the signal-to-noise ratio of nanoparticle detection over this background from the cell is to acquire images at a z-position where nanoparticles would still be detected strongly,

but the mitochondrial signal would be less intense. The mitochondrial signal of some Rama 27 fibroblasts was imaged at various z-positions, and the signal intensity of the mitochondrial signal extracted (Figure 5.4). At a z-position of 0 μm, in effect at the interface between the sample and glass coverslip, the mitochondrial signal appears very intense (Figure 5.4A). This is confirmed when the line profile of some exemplar mitochondria are taken with peaks corresponding to the photothermal signal they elicit (Figure 5.4B). When the detection volume is moved 0.5 μm above the coverslip in the same sample, the mitochondria in the image appear less intense (Figure 5.4C). Again this is further confirmed from the line profile in Figure 5.3D of the same mitochondria seen in Figure 5.4B. The signal has decreased by approximately 3-fold. Similar results are obtained when the images are acquired at 1.0 μm (Figure 5.4E and 5.4F), and although the mitochondrial signal appears slightly higher than in Figure 5.4C and 5.4D it is still lower than the intensity at 0 μm. This increase will be attributed to the three dimensionality of the sample and the distribution of mitochondria. This will not be homogeneous; therefore, some mitochondria at different z-positions may enter the volume, and thus be detected. Further support for this comes from the appearance of new, and broadening of existing, peaks in the line profile at 1.0 μm (Fig. 5.4F). From this point all photothermal images of Rama 27 fibroblast cells were acquired at a z-position of 0.5 μm.

5.3 Single molecule imaging of FGF-1 in the extracellular matrix of Rama 27 fibroblast cells

Unlike FGF-2, FGF-1 is a universal ligand, i.e., it is able to bind to all isoforms of FGFR. Both FGFs are members of the same sub-family, however, FGF-1 has been shown to possess quite different binding kinetics to cellular heparan sulfate

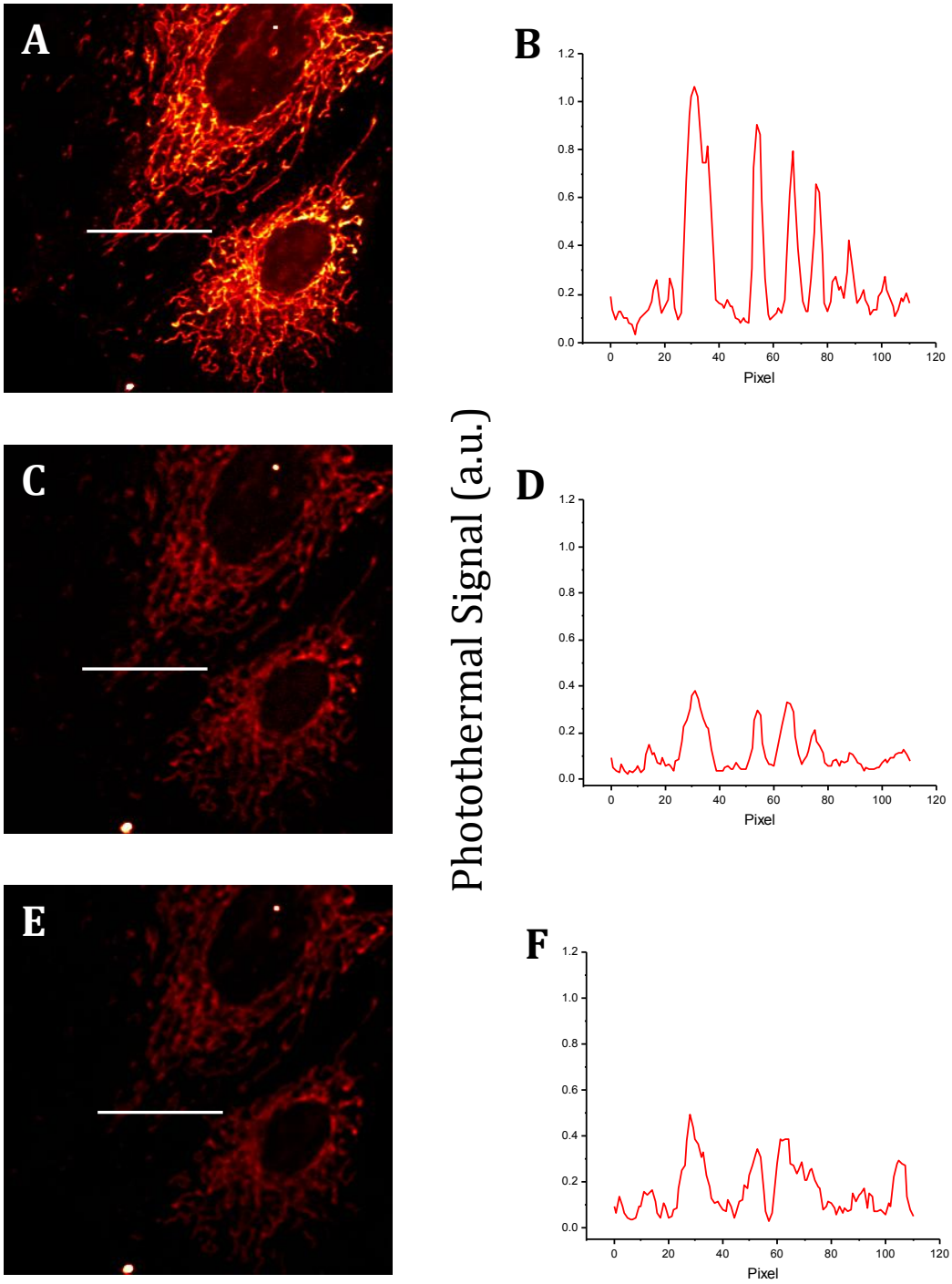

Figure 5.4 Photothermal images of Rama 27 fibroblasts at different z-positions. Images at (A) z = 0 µm, (C) z = 0.5 µm and (E) z = 1.0 µm with corresponding intensity line profiles of the mitochondrial signal denoted by the white line (B), (D) and (F), respectively.

than FGF-2, and thus mitogenic activity (Rahmoune *et al.*, 1998; Fernig *et al.*, 2000; Itoh & Ornitz, 2010). For example, the association rate constants of FGF-1 for HS are much slower than those of FGF-2, or indeed those of both these FGFs for heparin (Delehedde *et al.*, 2002; Xu *et al.*, 2012). The differences in HS binding have been interpreted to suggest that each FGF binds to a different subset of structures within heparan sulfate (Rahmoune *et al.*, 1998). For FGF-1 these sites may not only provide means of controlling FGF-1 activity, but also its diffusion in the pericellular matrix.

Photothermal imaging and tracking of nanoparticle labelled FGF-2 has shown that HS binding sites within the pericellular matrix control the distribution and diffusion behaviour of FGF-2. This will be dealt with in more detail in Section 5.4. However, given that FGF-2 has such distinct binding kinetics compared with FGF-1, is it possible that FGF-1 too also shows similar behaviour? If the binding kinetics of an FGF to HS contribute to regulating its movement in the pericellular matrix, as has been suggested (Duchesne *et al.*, 2012), one would expect that FGF-1 would diffuse differently. Therefore, hexahistidine tagged FGF-1 protein (a gift from Changye Sun and Yong Li, University of Liverpool) was conjugated to monofunctional tris-NTA nanoparticles (Chapter 2 Section 2.4.6). Live Rama 27 fibroblast cells were then incubated with 2 nM FGF-1 nanoparticle conjugate, and, after washing, photothermal images were taken (Figure 5.5). This concentration is higher than required for similar labelling with FGF-2 nanoparticles (~ 220 pM, Duchesne *et al.*, 2012). Firstly, imaging reveals that FGF-1 also diffuses within the pericellular matrix, characterized by 'streaking' within the image (blue boxes, Figure 5.5 Panels 1. and 2.). This movement appears to be quite common, suggesting that indeed the binding of FGF-1 to cellular HS may be weak, allowing most molecules to move. However, it is worth noting that FGF-1 nanoparticles are not detected in solution, therefore, the binding

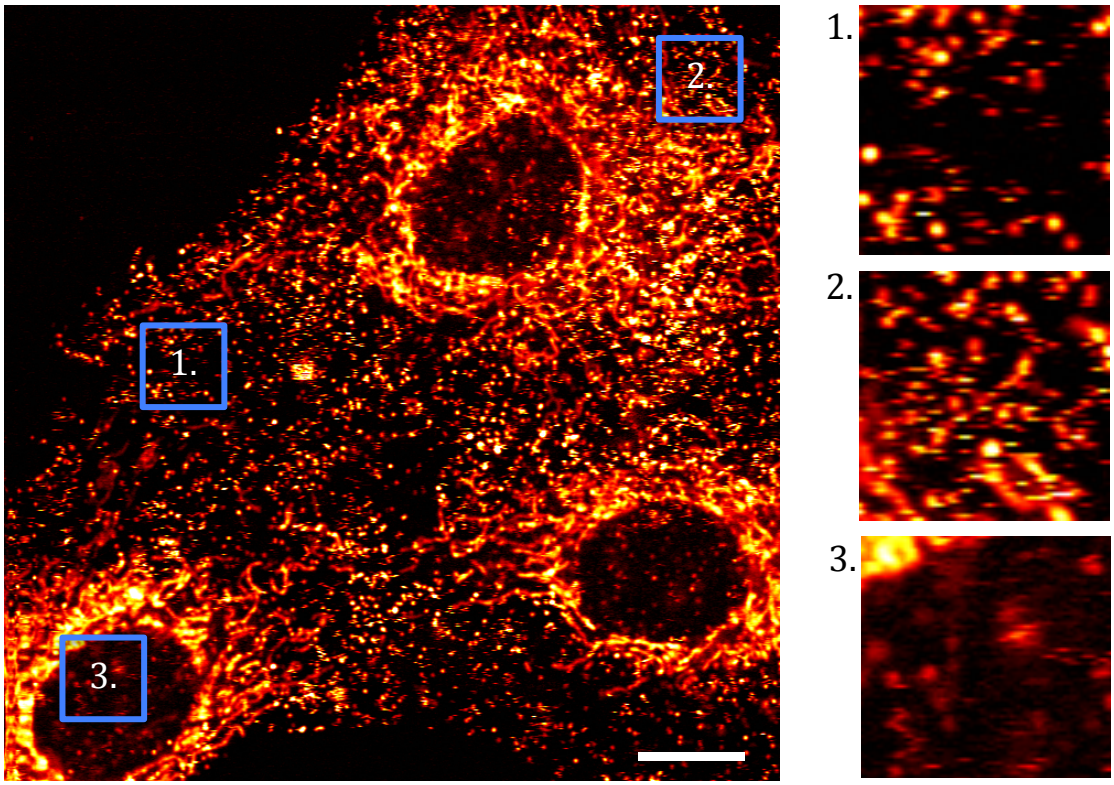

Figure 5.5 Photothermal images of Rama 27 fibroblast cells incubated with 2 nM FGF-1 nanoparticle conjugate (scale bar 10 μm). Boxes 1., 2. and 3. correspond to 7.5 x 7.5 μm areas enlarged in the side panels.

sites, although they may be weak, still retain FGF-1 within the pericellular matrix. There is also signal present in the area where the nucleus is (blue box, Figure 5.5 Panel 3.). This is unlikely to be due to translocation of FGF-1, as the timescale of the experiment from FGF-1 addition (1-2 hours) would not permit nuclear localization. However, this may be more conveniently explained by FGF-1 nanoparticle being able to access the matrix underneath the cell, i.e., between coverslip and the cell membrane. This would certainly be permitted if FGF-1 binding to HS were much weaker, as this would facilitate much longer-range movement of FGF-1. Imaging of the same cell 8 hours later reveals that FGF-1 is not maintained in the matrix over this time (Figure 5.6A and B). In Figure 5.6 (side panel 2.) it can be seen that photothermal signal, very similar to the 'streaking' presented in Figure 5.5, is detected in areas where the cell, and, therefore, pericellular matrix is not present. This signal arises from the diffusion of FGF-1 nanoparticles in the bulk medium. This means that FGF-1 nanoparticles have escaped from the pericellular matrix within this time period. It is difficult in the context of this experiment to determine whether any of this bulk FGF-1 re-binds the matrix.

Thus, the imaging of FGF-1 in the extracellular matrix of live Rama27 cells suggests that the diffusion and binding behaviour of FGF-1 in the pericellular matrix is quite different to that of FGF-2. The movement of FGF-1 appears to be more pronounced, with the possibility that longer-range movement of FGF-1 is facilitated (e.g. to the matrix underneath the cell). The diffusion of FGF-1 into the bulk medium after 8 hours also suggests that FGF-1 can indeed escape the matrix, in contrast to FGF-2 (Flaumenhaft *et al.*, 1990; Vlodavsky *et al.*, 1991; Fernig *et al.*, 1992; Duchesne *et al.*, 2012). This supports the hypothesis that the kinetics of binding of morphogens to heparan sulfate determine their movement in matrix and so the shape

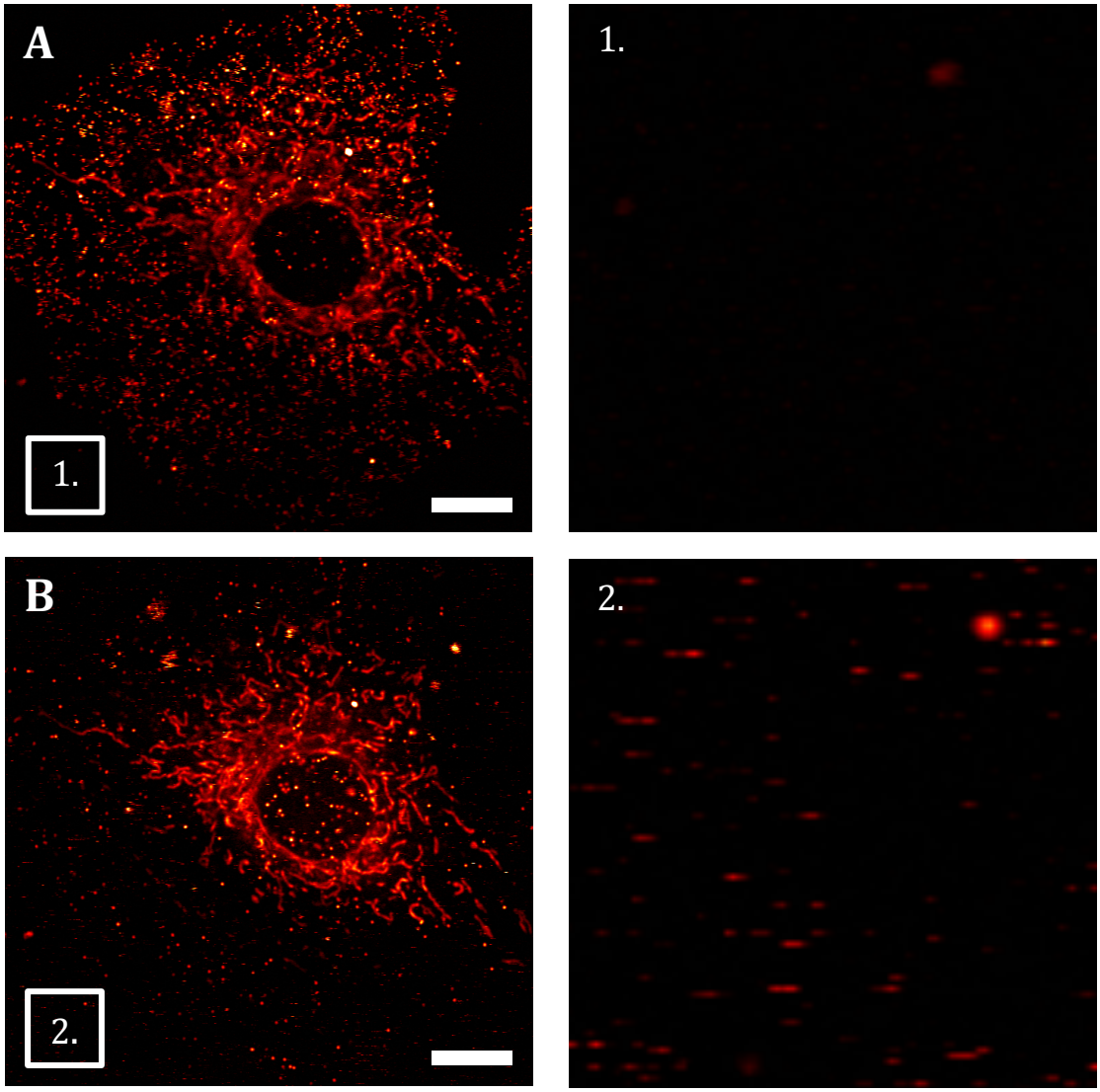

Figure 5.6. Photothermal images of Rama 27 fibroblast cells incubated with 2 nM FGF-1 nanoparticle conjugate at (A) 0 hours and (B) 8 hours (scale bar 10 μm). Boxes 1., 2. correspond to the same area in both images enlarged in the side panels**.**

of morphogen gradients. In the case of FGF-1, the present data suggest that it has a longer range than FGF-2 and would form longer, shallower gradients. The present data may also explain why FGF-1 in cell growth assays typically is 100-fold less active than FGF-2, unless an excess of heparin is present in the culture medium. FGF-2 loads into the matrix, where the interaction with heparan sulfate stabilizes its structure (Uniewicz *et al.*, 2010). In contrast, FGF-1 exchanges between the matrix and the culture medium, so is more susceptible to denaturation, unless polysaccharide is also added to the cultured medium.

5.4 Diffusion dynamics of FGF-2 in the extracellular matrix via PhRICS

The diffusion of FGF-2 in the extracellular matrix has been previously investigated using photothermal tracking (Duchesne *et al.*, 2012). Here, the tracking of single FGF-2 proteins revealed that they spend most of their time in confined motion, governed by binding sites in HS. However, it was also shown that FGF-2 can also escape this confinement and showed a range of diffusion behaviour from slow (< 0.1 $\mu m^2/s$) to fast (< 2 $\mu m^2/s$) and directed diffusion (Duchesne *et al.*, 2012). This movement was non-random, and it was hypothesized that the distribution of HS binding sites (supported by electron microscopy data) can form networks that promote or inhibit FGF-2 movement through the pericellular matrix (Duchesne *et al.*, 2012). However, it is worth noting that photothermal tracking is speed limited (~ 2-3 $\mu m^2/s$). Thus, it is possible that tracking cannot cover the full range of FGF-2 diffusion in the matrix, with faster populations, i.e., greater than 3 $\mu m^2/s$, going unseen or being 'lost' by the tracker. It is too worth considering that although the spatial resolution of photothermal tracking is unparalleled by other photothermal techniques, the coverage of the system under observation is an issue. Tracking experiments will be performed

over hours, as many data sets are required to calculate diffusion constants, and often these tracks are then related back to an image taken many hours previously. Thus, the technique does not afford access to the spatial relationship between an image of the cell and the track. Moreover, even when all the tracks are superimposed on a single cell, the spatial coverage is poor, i.e., the tracks only cover a part of the cell. Therefore, the assumption that the hundreds of tracks are representative of all FGF-2 movement may not hold due to the speed limitation of the tracker and the relatively low spatial coverage of tracking data.

A technique that may provide both the speed of acquisition and coverage required to representatively probe diffusion dynamics is PhRICS (Chapter 3 Section 3.8). Therefore, PhRICS measurements were performed on live Rama 27 cells labelled with 600 pM nanoparticle FGF-2 conjugate (Chapter 4 Section 4.2.4). The PhRICS imaging parameters (i.e., pixel size, scan area and dwell time) are identical to those used in Chapter 3 Section 3.8. Photothermal images of Rama27 cells incubated with 600 pM mix-matrix nanoparticles and 600 pM nanoparticle functionalised with FGF-2 are presented in Figure 5.7A and B, respectively. Here, it is evident that binding to the cell is facilitated by FGF-2, and no detectable nanoparticles are seen in the absence of FGF-2 functionalisation (Figure 5.7A). In contrast to PhRICS experiments in solution (Section 3.8), here PhRICS measurements were taken at different scan areas (boxes, Figure 5.7B). Exemplar PhRICS data acquired for analysis on FGF-2 labelled Rama 27 cells are presented as movies in the accompanying Appendix CD-ROM. Figure 5.8 shows some sequential frames from Movie_4 (Appendix C). There are some striking features of these data. Firstly, there is transient signal in the form of streaking within the images (white box, Figure 5.8

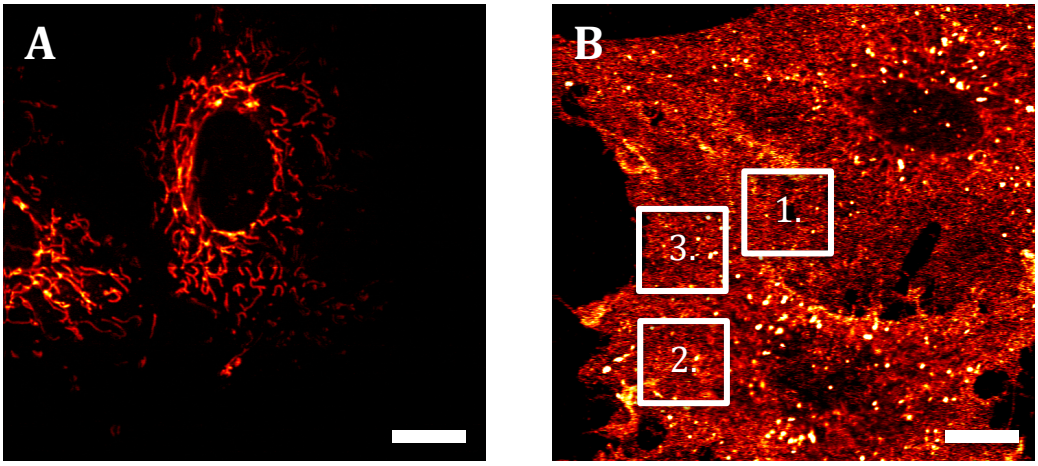

Figure 5.7 Photothermal images of Rama 27 fibroblast cells incubated with 600 pM (A) mix-matrix nanoparticles (B) FGF-2 nanoparticle conjugate (scale bar 10 μm). White boxes indicate position where PhRICS imaging was performed**.**

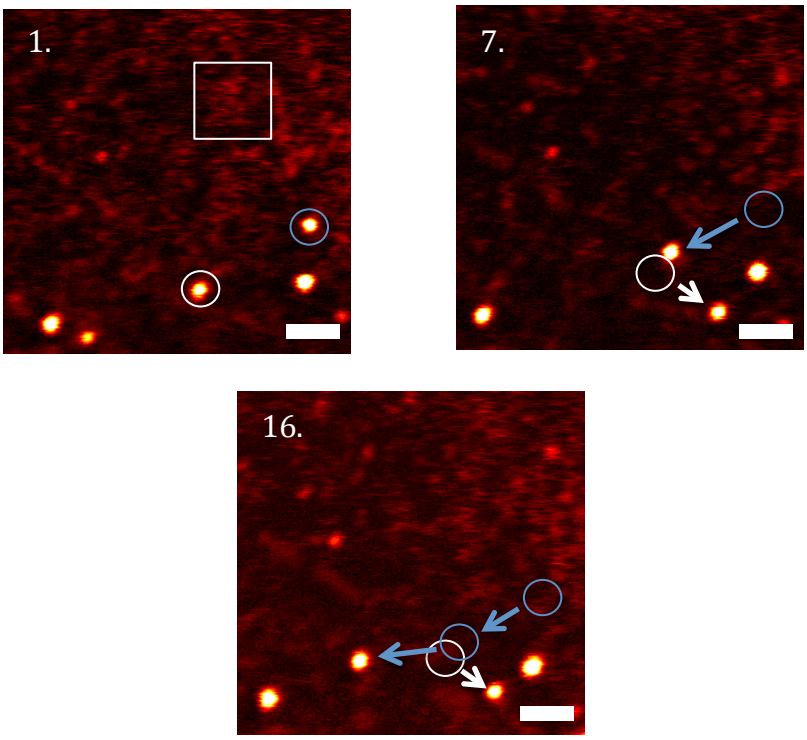

Figure 5.8. Photothermal images of Rama 27 fibroblasts incubated with 600 pM FGF-2 nanoparticle conjugate (scale bar 2 μm). Circles indicate the starting position and arrow indicate the movement of multiple FGF-2 nanoparticles diffusing in the pericellular matrix (Frames 1., 7. and 16. are taken from Appendix C Movie_4).

Frame 1), and secondly more defined intense peaks of signal are seen (circles, Figure 5.8 Frames 1 to 16), that do not move during one image (lasting ~ 30 seconds), but do indeed move from image to image. The reader is also directed to the other movies present within Appendix C, as other remarkable behaviours are observed, such as the separation and recombination of intense peaks, corresponding to several FGF2 nanoparticles. Here, it is obvious that the distribution of all FGF-2 in the pericellular matrix, and in all likelihood the structure of the matrix itself, is changing on time scales much shorter than required to track a single FGF-2. Such changes were used in a limited fashion in Duchesne *et al.*, (2012) to argue that the FGF-2 was actually moving, before performing the analysis by single particle tracking. Within the PhRICS data, areas that were relatively free from intense peaks were chosen for analysis. This is because the stability of the optical signal (no bleaching, c.f., fluorescent RICS; Chapter 3 Section 3.8) results in a substantial "immobile component" within the image that would thus dominate the analysis. The spatial correlation output from the PhRICS for Area 3 (Figure 5.7B) is shown in Figure 5.9 as an example. The PhRICS analysis on live cells gave an average diffusion coefficient for nanoparticle labelled FGF-2 of 0.13 ± 0.03 $\mu m^2/s$. For comparison of the diffusion coefficient to the photothermal tracking data already published on FGF-2, the diffusion coefficient values of the Group 3 (simple diffusion) and Group 4 (slow directed diffusion) and Group 5 (long/fast directed diffusion) were averaged (Duchesne *et al.*, 2012). These groups of movement are those that will be measured by PhRICS, since confined (below diffraction limit) and "immobile" components are removed from the analysis. The average diffusion coefficient for these groups is 0.09 $\mu m^2/s$. This value is approximately 30 % of that seen by PhRICS. This, therefore, suggests that not only does photothermal tracking not give full coverage of the range

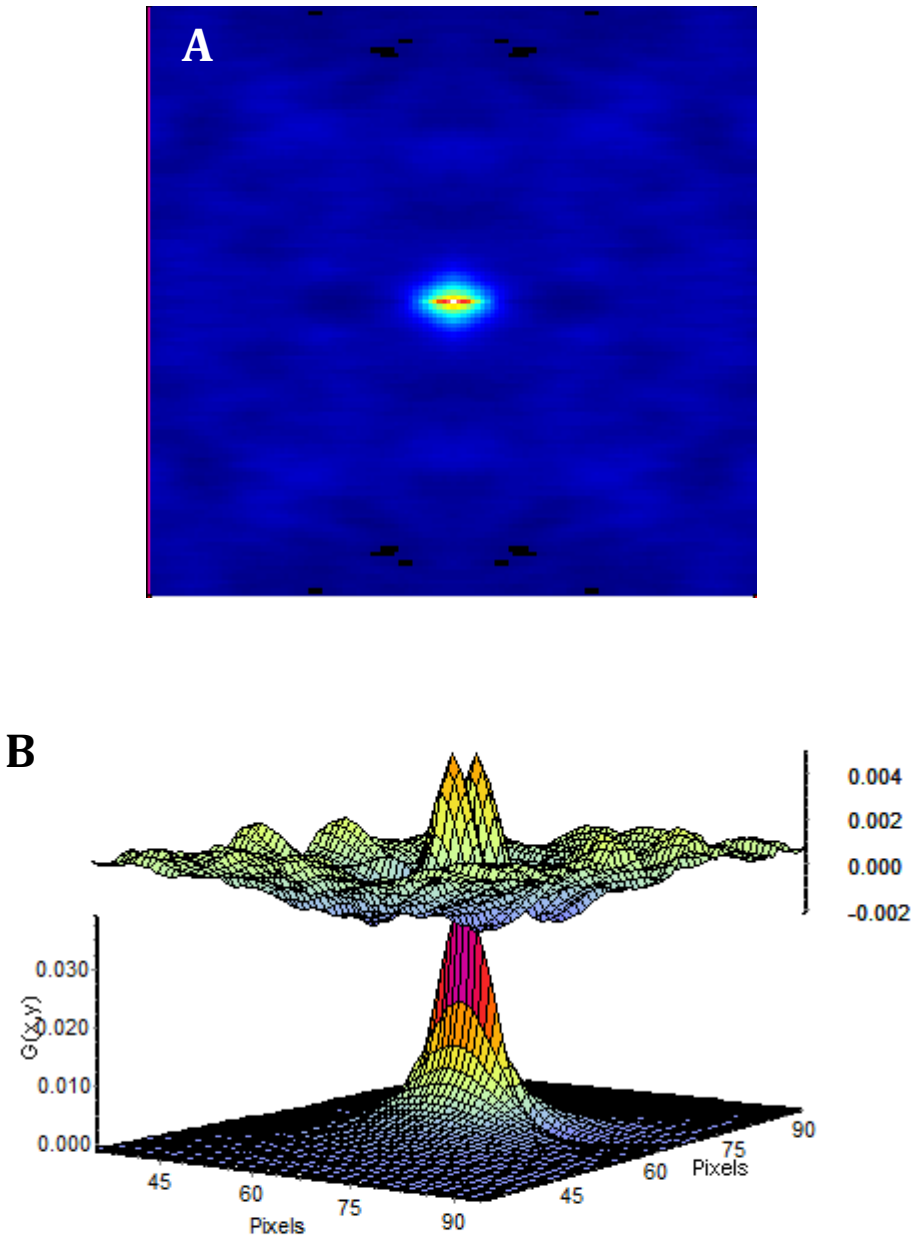

Fig 5.9 Spatial correlation and fitting result from PhRICS imaging of Area 3 of Figure 5.7. (A) Average spatial correlation from RICS analysis of 15 images. (B) Surface fitting result for spatial correlation in (A).

of FGF-2 diffusion behaviour, but also that some diffusion speeds of FGF-2 are higher than first thought.

5.5 Conclusions from Chapter 5

The photothermal measurements made on FGF nanoparticle conjugates *in vitro*, both in solution and on cells, have provided new insights into their interactions. The binding mode of FGF-2 to oligosaccharides, as a proxy for HS, has been of considerable interest. One model is that FGF-2 (and also FGF-1) binds with pronounced positive cooperativity to oligosaccharides whose length is sufficient for optimal generation of a cellular growth response, i.e., octasaccharides and above (Delehedde *et al.*, 2002; Goodger *et al.*, 2008), and that this underpins the initiation of the formation of a receptor complex (Robinson *et al.*, 2005; Saxena *et al.*, 2010; Brown *et al.*, 2013). However, the measurements made here using a new technique, PhRICS, do not support such a mechanism. The results suggest that indeed higher order complexes of FGF-2 and dodecasaccharide may be formed in solution, but these are driven by mass action rather than cooperativity, because they are apparent only when the components are at an equimolar ratio or the protein is in excess. Moreover, it appears that at physiological concentrations, i.e., nM, cooperativity is unlikely to play a significant role. The high sensitivity of this technique, therefore, provides new insights into the mechanism of FGF:HS interactions at physiologically relevant concentrations and greater understanding of the formation of receptor complexes.

Photothermal imaging of FGF nanoparticle conjugates in the extracellular matrix of live cells has proven to be a valuable tool for the observation of the heterogeneous interactions of FGFs with HS. The first photothermal imaging of FGF-1 has been performed, and has revealed that its behaviour (both diffusion and binding) in the pericellular matrix is somewhat different to the other studied member of its subfamily, FGF-2. Previous work on FGF-2 led to the conclusion that the kinetics of its binding to heparan sulfate, its specificity for particular sugar structures and the

spatial distribution of these structures in matrix determined its movement in matrix. The present work on FGF-1 provides the first data to test the idea that this may be a general feature for many heparin-binding proteins. The results strongly suggest that this is indeed the case. Clearly a greater amount of data, acquired on live and fixed cells (where cellular biochemistry can no longer influence protein movement) will be required to strengthen this conclusion. Moreover, performing similar experiments with, for example, FGFs from other subfamilies that have more distinct heparan sulfate binding properties would test the idea more robustly.

The use of PhRICS to measure the diffusion coefficient of FGF-2 in the extracellular matrix has revealed the power of this new approach for the investigation of the dynamics of biological molecules. PhRICS showed that the average diffusion coefficient for mobile FGF-2 in the pericellular matrix was approximately 30 % higher than that seen by photothermal tracking. The ability to get large spatial coverage of the system (μm) while still acquiring data at biologically relevant times (μs) has also identified new behaviour of FGF-2 protein in the matrix. The analysis of the movement of multiple FGF-2 proteins in the matrix in unison over the time for an image stack to be acquired will require other analyses, as they are not compatible with the present with the current PhRICS analyses, and thus lost.

6. Conclusions and future perspectives

The observation of single biomolecules is a requisite for understanding the heterogeneity that governs biological function. In this Thesis the system that embodied such heterogeneity was the FGF signalling molecules, and the interactions of FGFs with a ubiquitous component of pericellular matrix, HS. Currently, existing optical techniques that allow observation of single biomolecules, such as SPT, SMT and correlation spectroscopy were discussed briefly in Chapter 1 Section 1.1. The use of scattering labels, which underlies SPT, allows the potential for tracking single molecules at fast acquisition rates. However, the labels themselves undermine this observation, as they are often large and suffer from multivalent interactions with the molecules they label. The development of fluorescent labels for SMT and FCS has circumvented this problem, but also brought new issues, such as observation time (on the order of ms to s) due to photobleaching.

The development of photothermal microscopy has exploited the exceptional stability of a gold nanoparticle under excitation at its plasmon resonance. The signal generated, the photothermal signal, is completely stable over time and has allowed the detection of gold nanoparticles at a high signal-to-noise ratio. This has been exploited for the development of analogous techniques to those described above, such as photothermal tracking and PhACS. The development of the second photothermal microscope at the University of Liverpool is described in Chapter 3. The detection of single gold nanoparticles at a high signal-to-noise ratio with moderate heating power was achieved, and served as a platform for the implementation of PhACS. The use of

PhACS to measure the diffusion coefficient of gold nanoparticles in solution led to an erroneous measurement of nanoparticle diffusion coefficients. This is likely to result from an aftefact in the acquisition of the photothermal signal data from the Nanonis SC4 by our custom written program. If this issue can be resolved then the potential for this technique to probe the diffusion of biological molecules labelled with gold nanoparticles both in solution and on cells can be realised. The development of a novel technique, PhRICS (Chapter 3 Section 3.8), has also been described. PhRICS, like PhACS, is able to measure the diffusion coefficient of gold nanoparticles in solution; however, it also has the added advantage of a wider spatial coverage of the sample as well. This technique showed great potential for the observation of nanoparticle labelled biomolecules at all diffusion speeds (Chapter 5 Section 5.4).

Chapter 4 outlined the development of new ligand shells for gold nanoparticles to allow the incorporation of a maleimide group. This group is particularly versatile due to the ability of the group to undergo Michael addition reactions with thiol groups. Initially, a "one-step" capping reaction using ligands containing a disulphide bond was described (Chapter 4 Section 4.1.1). The protection of the thiol required for binding to the gold surface, allowed the use of a similar disulphide ligand terminated with a single maleimide. This approach initially showed substantial promise, with much of the experimental work being completed, for conjugation of both FGF-2 protein and oligosaccharides (Chapter 4 Section 4.1.2). However, the ligand, and thus ligand shell, began to show some negative charge, characterized by binding to DEAE-Sepharose (Chapter 4 Section 4.1.3). This rendered the ligand shell useless for biological applications. This provides a warning of the care that must be taken when using a disulphide ligand. Therefore, a second approach was taken that exploiting copper-free click chemistry (Chapter 4 Section

4.2). Here, nanoparticles with a single azide group in their monolayer were reacted with a strained cyclooctyne functionalised with a maleimide group (DIBO-Mal). This approach was shown to be very successful for conjugation to both FGF-2 protein and both MBPH hexa- and dodecasaccharides. The FGF-2 nanoparticle conjugate was shown to be applicable for single molecule experiments (Chapter 4 Section 4.3; Chapter 5 Section 5.1 and 5.4). In the context of current approaches for the labelling of single biomolecules with gold nanoparticles, this method is promising. The use of NTA bearing nanoparticles has been used previously to label hexahistidine tagged FGF-2 proteins, but this conjugation is not covalent (Duchesne *et al.*, 2008). The development of a covalent linkage alleviates any risk of exchange of the nanoparticle with histidine patches occurring naturally in other proteins. The adoption of genetically encoded covalent conjugation approaches is of increasing interest, for example, the use of genetically modified cell lines to express a HaloTag fusion (a 'snap tag' developed by Promega) with a protein of interest. The ability to conjugate any thiol-bearing molecule, e.g., a chloroalkane that would covalently link with a HaloTag protein, to the particles described here offers a great potential for the labelling of biomolecules both *in vitro* and *in vivo* with gold nanoparticles.

The interaction of FGF-2 with HS has been investigated in depth by numerous investigators (Delehedde *et al.*, 2002; Goodger *et al.*, 2008; Saxena *et al.*, 2010). While oligomerization of FGF-2 is a universal theme in the presence of a limited concentration of heparin-derived oligosaccharides (Yayon *et al.*, 1991; Ornitz *et al.*, 1992), the existence of cooperativity at concentrations where the oligosaccharide is equimolar or in excess of FGF-2 has also been demonstrated (Goodger *et al.*, 2008; Saxena *et al.*, 2010). In Chapter 5 Section 5.1, PhRICS experiments were performed with nanoparticle labelled FGF-2. Here, oligomerization of FGF-2 was observed

when dodecasaccharide concentration decreased, but cooperativity was not. This suggests that even in the presence of limiting concentrations of dodecasaccharide not all of FGF-2 is present within oligomers, and there may be an equilibrium between unbound, singularly bound and dimerized FGF-2 on dodecasaccharide. This measurement was carried out at concentrations that are nearer to the measured concentration of FGF-2 in the extracellular matrix (i.e., nM) and around the K_d of the FGF-2 for the sugar. Therefore, binding of FGF-2 to HS seems to be governed solely by mass action and affinity. At physiological concentrations oligomerization/cooperative binding is not observed, thus, this may potentiate mobility and allow the formation of morphogen gradients by allowing diffusion. However, it is entirely possible that HS structure may also provide the means of locally concentrating FGF-2, e.g., by providing, at molecular scales, a number of closely spaced FGF-2 binding sites. The increase in local concentration could initiate the cooperativity seen at μM concentrations, thus, leading to a biological function. This model, therefore, places HS as the master regulator of FGF function whereby structure is key to the titration (or inhibition) of FGF-2 into the signalling system. This type of study could once again be applied to other FGFs from different subfamilies. The subfamilies have largely varied binding kinetics and would lead to further understanding of whether cooperativity/oligomerization is a common pathway in the regulation of FGF biological function.

One interesting feature of the FGFs is that they often possess secondary heparin binding sites (Ori *et al.*, 2009; Xu *et al.*, 2012). The location of these sites on the FGF surface appears to follow the evolutionary relationships of the FGF subfamilies (Xu *et al.*, 2012). In the one instance, where an attempt to measure the affinity of the secondary sites, it was found to be at least 3 orders of magnitude lower

than that of the canonical site (Kinsella *et al.*, 1998). However, given that the canonical site is sufficient to bring the FGF-2 into the matrix, perhaps these secondary sites play an important role in governing the movement of the FGF-2 and they may even be involved in cross-linking heparan sulfate chains. Such a scenario might explain why some of the FGF-2 is immobile and also the existence of foci of FGF-2 molecules, that appear to move in concert. To test this idea, PhRICS should be performed on FGFs where the secondary heparin binding sites are mutated.

The spatiotemporal organization of FGF molecules in the pericellular matrix is key to their biological function. In Chapter 5 photothermal imaging of nanoparticle labelled FGF-2 and FGF-1 (for the first time) was used to investigate their diffusion behaviour in the pericellular matrix. Imaging of FGF-1 revealed that not only does it appear to be more mobile than FGF-2 in the matrix, but also that it is not retained in the matrix over time. This suggests that FGF-1 may have a quite different range over which it exerts its activity, which would involve long-range action and the formation of gradients that have a much shallower concentration than those of FGF-2. In this respect it is noteworthy that in the FGF family, FGF-1 is the "universal ligand", i.e., it is the only FGF that can bind and activate all isoforms of the four FGFRs (Beenken *et al.*, 2012). The apparently lower restrictions on FGF-1 diffusion would therefore result in a broad activation of FGFRs over a larger distance than possible by, for example, FGF-2.

The diffusion of FGF-2 has been shown to depend on binding to cellular HS, and that the diffusion behaviours seen were heterogeneous (Duchesne *et al.*, 2012). However, the technique used to observe FGF-2 diffusion, photothermal tracking, is speed limited (fastest speed of 2-3 $\mu m^2/s$), therefore, it is possible that FGF-2 may move faster in the matrix than first thought. Indeed, this issue is alluded to in

Duchesne *et al.*, (2012). The diffusion of FGF-2 nanoparticle conjugates on live fibroblasts was investigated using PhRICS (Chapter 5 Section 5.4). The PhRICS method revealed that the movement of the mobile FGF-2 was indeed faster than suggested by photothermal tracking, though the conclusion that it is trapped in the pericellular matrix still stands. The PhRICS imaging also revealed that the matrix might actually be remodelling constantly evidenced by the movement of many FGF molecules in unison on a single HSPG or a group of connected HSPGs. This, therefore, demonstrates the potential of PhRICS imaging to investigate the organization of the pericellular matrix at the single molecule level. There is also further potential to extend PhRICS to turn the observed diffusion behaviour into a "map". In its original implementation, RICS is performed with both a fixed scan speed over a fixed scanning area. It has been has shown that uncoupling the sampling of the scanning area from the scan speed provides access to variable diffusion speeds over a fixed sample area (Groner *et al.*, 2010). This will identify subpopulations of molecules with distinct diffusion coefficients. The data could then be used to generate the diffusion mapping analysis described in Groner *et al*. The diffusion maps can then be used to identify specific areas of matrix where the movement, owing to reaction diffusion, is 'fast' or 'slow'. The data could, therefore, directly test the hypothesis that the kinetics of binding of FGFs the HS control their movement in extracellular matrix and whether this is a likely general mechanism for regulating gradients of heparan sulfate binding effectors, such as the majority of morphogens.

Diffusion mapping and PhRICS imaging could also be applied to investigate other components in the matrix. The observation of multiple bright 'spots' (containing multiple FGF-2 labelled nanoparticles), *via* PhRICS, moving in/on the membrane suggests restructuring of the extracellular matrix. These 'spots' are likely

to contain many FGF proteins bound to a single HS chain of the proteoglycan, multiple chains of the proteoglycan, or even cross-linking of multiple chains from different proteoglycans. Currently, due to the observation of just the FGF protein it is not possible to distinguish between these possibilities. However, labelling and observation of the HS polysaccharide or core protein would allow these possibilities to be distinguished, at least in part. Therefore, a significant challenge would be to observe/investigate the dynamics of HS structures and HSPGs themselves. One approach would be to use a protein or peptide with a very 'restricted menu' of heparan sulphate structure binding specificity. Examples could include antithrombin III and the HappY peptide (Yabe *et al.*, 2011), which both bind to a well characterised pentasaccharide structure or 'phage display antibodies (Thompson *et al.*, 2009). The caveat is that specificity is not always as high as it might seem and the notion of selectivity is probably better. This has been demonstrated with phage display antibodies, which are clearly selective, but not for a single structure. Even with antithrombin III and in all likelihood with the HappY peptide, variations in sequence are well documented. Thus, whereas the loss of the 3-OS within the pentasaccharide (GlcNS, 6S-GlcA-GlcNS, 3S(±6S)-IdoA(2S)-GlcNS(±6S)) causes a ~1000-fold loss of antithrombin III activity towards thrombin, loss of the reducing end N-sulfate has a weaker effect (Skidmore *et al.*, 2008a). Thus, such probes would be more selective than and FGF, but not necessarily completely so. Nonetheless, if the antithrombin III or the HappY peptide showed that the distribution of binding sites did indeed change over time, then this would be good evidence for the dynamics of the HSPG. As regards the movement of the core protein in the membrane/matrix, this could be measured directly since genetic labelling is possible. For example the core protein of, e.g., syndecan-1, may be labelled by introducing a HaloTag fusion at its N-terminus,

which could then be labelled directly with nanoparticles carrying a HaloTag ligand. This would provide novel insights into the proteoglycans' diffusion dynamics, and thus the dynamics of matrix structure, at endogenous levels of HSPGs. More ambitious would be a 'dual-labelling' experiment whereby one could actually correlate, in real-time, movements of either HS binding proteins or HS structures with the movement of the core proteins in the membrane. This would demonstrate directly if movement/positioning of effectors in the matrix were achieved solely by free/reaction diffusion on binding sites that are 'non randomly distributed', as described above and previously observed (Yu *et al.*, 2009; Duchesne *et al.*, 2012), or whether a contiguous mechanism such as the 'movement of the matrix' is also required. This mechanism could be involved in the formation of signalling platforms that require the orchestrated presence of many matrix proteins/components, e.g., focal adhesions or endocytic buds, or processes that require these components act at high concentration in a short space of time, e.g., wound healing.

Appendices

All appendices are located on the CD-ROM accompanying this thesis.

Appendix A

Photographs of sample chamber prepared by thermal sealing using parafilm, and the PSA macro for sizing of gold nanoparticles from TEM micrographs.

Appendix B

Custom written program (LabView) for acquisition of PhACS (known as "ACS_3"), plus the custom written fitting functions used to fit PhACS data within Origin 8.5.

Appendix C

Movies 1-4 (.avi and quick time) of PhRICS imaging on live Rama 27 fibroblasts labelled with 600 pM FGF-2 nanoparticle conjugate. The frame rates of the movies are 8 fps.

Bibliography

Absil, E., Tessier, G., Gross, M., Atlan, M., Warnasooriya, N., Suck, S., Coppey-Moisan, M., & Fournier, D. (2010). Photothermal heterodyne holography of gold nanoparticles. *Opt Express, 18*(2), 780-786.

Aebersold, R., & Mann, M. (2003). Mass spectrometry-based proteomics. *Nature, 422*(6928), 198-207.

Allen, B. L., Filla, M. S., & Rapraeger, A. C. (2001). Role of heparan sulfate as a tissue-specific regulator of FGF-4 and FGF receptor recognition. *J Cell Biol, 155*(5), 845-858.

Azmi, N. (2012). *Doctoral thesis, University of Liverpool*.

Ba, H., Rodriguez-Fernandez, J., Stefani, F. D., & Feldmann, J. (2010). Immobilization of gold nanoparticles on living cell membranes upon controlled lipid binding. *Nano Lett, 10*(8), 3006-3012.

Barraclough, R., Fernig, D. G., Rudland, P. S., & Smith, J. A. (1990). Synthesis of basic fibroblast growth factor upon differentiation of rat mammary epithelial to myoepithelial-like cells in culture. *J Cell Physiol, 144*(2), 333-344.

Baskin, J. M., Dehnert, K. W., Laughlin, S. T., Amacher, S. L., & Bertozzi, C. R. (2010). Visualizing enveloping layer glycans during zebrafish early embryogenesis. *Proc Natl Acad Sci U S A, 107*(23), 10360-10365.

Beenken, A., Eliseenkova, A. V., Ibrahimi, O. A., Olsen, S. K., & Mohammadi, M. (2012). Plasticity in interactions of fibroblast growth factor 1 (FGF1) N terminus with FGF receptors underlies promiscuity of FGF1. *J Biol Chem, 287*(5), 3067-3078.

Berciaud, S., Cognet, L., Blab, G. A., & Lounis, B. (2004). Photothermal heterodyne imaging of individual nonfluorescent nanoclusters and nanocrystals. *Phys Rev Lett, 93*(25), 257402.

Berciaud, S., Lasne, D., Blab, G. A., Cognet, L., & Lounis, B. (2006). Photothermal heterodyne imaging of individual metallic nanoparticles: Theory versus experiment. *Phys Rev B, 73*(4), 045424.

Bernardin, A., Cazet, A., Guyon, L., Delannoy, P., Vinet, F., Bonnaffe, D., & Texier, I. (2010). Copper-Free Click Chemistry for Highly Luminescent Quantum Dot Conjugates: Application to in Vivo Metabolic Imaging. *Bioconjugate Chem, 21*(4), 583-588.

Birrell, G. B., Hedberg, K. K., & Griffith, O. H. (1987). Pitfalls of immunogold labeling: analysis by light microscopy, transmission electron microscopy, and photoelectron microscopy. *J Histochem Cytochem, 35*(8), 843-853.

Borgdorff, A. J., & Choquet, D. (2002). Regulation of AMPA receptor lateral movements. *Nature, 417*(6889), 649-653.

Boyer, D., Tamarat, P., Maali, A., Lounis, B., & Orrit, M. (2002). Photothermal imaging of nanometer-sized metal particles among scatterers. *Science, 297*(5584), 1160-1163.

Brennan, J. L., Hatzakis, N. S., Tshikhudo, T. R., Dirvianskyte, N., Razumas, V., Patkar, S., Vind, J., Svendsen, A., Nolte, R. J. M., Rowan, A. E., & Brust, M. (2006). Bionanoconjugation via click chemistry: The creation of functional hybrids of lipases and gold nanoparticles. *Bioconjugate Chem, 17*(6), 1373-1375.

Bibliography

Brovchenko, I., Krukau, A., Smolin, N., Oleinikova, A., Geiger, A., & Winter, R. (2005). Thermal breaking of spanning water networks in the hydration shell of proteins. *J Chem Phys, 123*(22), 224905.

Brown, A., Robinson, C. J., Gallagher, J. T., & Blundell, T. L. (2013). Cooperative Heparin-Mediated Oligomerization of Fibroblast Growth Factor-1 (FGF1) Precedes Recruitment of FGFR2 to Ternary Complexes. *Biophys J, 104*(8), 1720-1730.

Brown, C. M., Dalal, R. B., Hebert, B., Digman, M. A., Horwitz, A. R., & Gratton, E. (2008). Raster image correlation spectroscopy (RICS) for measuring fast protein dynamics and concentrations with a commercial laser scanning confocal microscope. *J Microsc, 229*(Pt 1), 78-91.

Chen, X. Y., Qoutah, W. W., Free, P., Hobley, J., Fernig, D. G., & Paramelle, D. (2012). Features of Thiolated Ligands Promoting Resistance to Ligand Exchange in Self-Assembled Monolayers on Gold Nanoparticles. *Aust J Chem, 65*(3), 266-274.

Clevenger, C. V., & Epstein, A. L. (1984). Identification of a nuclear protein component of interchromatin granules using a monoclonal antibody and immunogold electron microscopy. *Exp Cell Res, 151*(1), 194-207.

Cognet, L., Tardin, C., Boyer, D., Choquet, D., Tamarat, P., & Lounis, B. (2003). Single metallic nanoparticle imaging for protein detection in cells. *Proc Natl Acad Sci U S A, 100*(20), 11350-11355.

Cohn, M. J., Izpisua-Belmonte, J. C., Abud, H., Heath, J. K., & Tickle, C. (1995). Fibroblast growth factors induce additional limb development from the flank of chick embryos. *Cell, 80*(5), 739-746.

Corbierre, M. K., Cameron, N. S., Sutton, M., Mochrie, S. G., Lurio, L. B., Ruhm, A., & Lennox, R. B. (2001). Polymer-stabilized gold nanoparticles and their incorporation into polymer matrices. *J Am Chem Soc, 123*(42), 10411-10412.

Crick, S. L., Jayaraman, M., Frieden, C., Wetzel, R., & Pappu, R. V. (2006). Fluorescence correlation spectroscopy shows that monomeric polyglutamine molecules form collapsed structures in aqueous solutions. *Proc Natl Acad Sci U S A, 103*(45), 16764-16769.

Dahan, M., Levi, S., Luccardini, C., Rostaing, P., Riveau, B., & Triller, A. (2003). Diffusion dynamics of glycine receptors revealed by single-quantum dot tracking. *Science, 302*, 442-445.

De, M., Ghosh, P. S., & Rotello, V. M. (2008). Applications of Nanoparticles in Biology. *Adv Mater, 20*(22), 4225-4241.

Delehedde, M., Lyon, M., Gallagher, J. T., Rudland, P. S., & Fernig, D. G. (2002). Fibroblast growth factor-2 binds to small heparin-derived oligosaccharides and stimulates a sustained phosphorylation of p42/44 mitogen-activated protein kinase and proliferation of rat mammary fibroblasts. *Biochem J, 366*(Pt 1), 235-244.

DiGabriele, A. D., Lax, I., Chen, D. I., Svahn, C. M., Jaye, M., Schlessinger, J., & Hendrickson, W. A. (1998). Structure of a heparin-linked biologically active dimer of fibroblast growth factor. *Nature, 393*(6687), 812-817.

Digman, M. A., Brown, C. M., Sengupta, P., Wiseman, P. W., Horwitz, A. R., & Gratton, E. (2005). Measuring fast dynamics in solutions and cells with a laser scanning microscope. *Biophys J, 89*(2), 1317-1327.

Digman, M. A., & Gratton, E. (2009). Analysis of diffusion and binding in cells using the RICS approach. *Microsc Res Tech, 72*(4), 323-332.

Digman, M. A., Wiseman, P. W., Choi, C., Horwitz, A. R., & Gratton, E. (2009). Stoichiometry of molecular complexes at adhesions in living cells. *Proc Natl Acad Sci U S A, 106*(7), 2170-2175.

Dill, K. A., & Shortle, D. (1991). Denatured states of proteins. *Annu Rev Biochem, 60*, 795-825.

Doty, R. C., Fernig, D. G., & Levy, R. (2004). Nanoscale science: a big step towards the Holy Grail of single molecule biochemistry and molecular biology. *Cell Mol Life Sci, 61*(15), 1843-1849.

Duchesne, L., Gentili, D., Comes-Franchini, M., & Fernig, D. G. (2008). Robust Ligand Shells for Biological Applications of Gold Nanoparticles. *Langmuir, 24*(23), 13572-13580.

Duchesne, L., Octeau, V., Bearon, R. N., Beckett, A., Prior, I. A., Lounis, B., & Fernig, D. G. (2012). Transport of Fibroblast Growth Factor 2 in the Pericellular Matrix Is Controlled by the Spatial Distribution of Its Binding Sites in Heparan Sulfate. *Plos Biol, 10*(7).

Elf, J., Li, G. W., & Xie, X. S. (2007). Probing transcription factor dynamics at the single-molecule level in a living cell. *Science, 316*, 1191-1194.

Esko, J. D., & Lindahl, U. (2001). Molecular diversity of heparan sulfate. *J Clin Invest, 108*(2), 169-173.

Faham, S., Hileman, R. E., Fromm, J. R., Linhardt, R. J., & Rees, D. C. (1996). Heparin structure and interactions with basic fibroblast growth factor. *Science, 271*(5252), 1116-1120.

Fernig, D. G., Chen, H. L., Rahmoune, H., Descamps, S., Boilly, B., & Hondermarck, H. (2000). Differential regulation of FGF-1 and -2 mitogenic activity is related to their kinetics of binding to heparan sulfate in MDA-MB-231 human breast cancer cells. *Biochem Biophys Res Commun, 267*(3), 770-776.

Fernig, D. G., & Gallagher, J. T. (1994). Fibroblast growth factors and their receptors: an information network controlling tissue growth, morphogenesis and repair. *Prog Growth Factor Res, 5*(4), 353-377.

Fernig, D. G., Rudland, P. S., & Smith, J. A. (1992). Rat mammary myoepithelial-like cells in culture possess kinetically distinct low-affinity receptors for fibroblast growth factor that modulate growth stimulatory responses. *Growth Factors, 7*(1), 27-39.

Fernig, D. G., Smith, J. A., & Rudland, P. S. (1990). Appearance of basic fibroblast growth factor receptors upon differentiation of rat mammary epithelial to myoepithelial-like cells in culture. *J Cell Physiol, 142*, 108-116.

Flaumenhaft, R., Moscatelli, D., Saksela, O., & Rifkin, D. B. (1989). Role of extracellular matrix in the action of basic fibroblast growth factor: matrix as a source of growth factor for long-term stimulation of plasminogen activator production and DNA synthesis. *J Cell Physiol, 140*(1), 75-81.

Freese, C., Gibson, M. I., Klok, H. A., Unger, R. E., & Kirkpatrick, C. J. (2012). Size- and coating-dependent uptake of polymer-coated gold nanoparticles in primary human dermal microvascular endothelial cells. *Biomacromolecules, 13*(5), 1533-1543.

Gaiduk, A., Ruijgrok, P. V., Yorulmaz, M., & Orrit, M. (2010). Detection limits in photothermal microscopy. *Chem Sci, 1*(3), 343.

Gallagher, J. T. (2001). Heparan sulfate: growth control with a restricted sequence menu. *Journal of Clinical Investigation, 108*(3), 357-361.

Gobbo, P., & Workentin, M. S. (2012). Improved Methodology for the Preparation of Water-Soluble Maleimide-Functionalized Small Gold Nanoparticles. *Langmuir, 28*(33), 12357-12363.

Goodger, S. J., Robinson, C. J., Murphy, K. J., Gasiunas, N., Harmer, N. J., Blundell, T. L., Pye, D. A., & Gallagher, J. T. (2008). Evidence that heparin saccharides promote FGF2 mitogenesis through two distinct mechanisms. *J Biol Chem, 283*(19), 13001-13008.

Gospodarowicz, D. (1974). Localisation of a fibroblast growth factor and its effect alone and with hydrocortisone on 3T3 cell growth. *Nature*, 249, 123-127.

Gregory, J. D. (1955). The Stability of N-Ethylmaleimide and Its Reaction with Sulfhydryl Groups. *J Am Chem Soc, 77*(14), 3922-3923.

Groner, N., Capoulade, J., Cremer, C., & Wachsmuth, M. (2010). Measuring and imaging diffusion with multiple scan speed image correlation spectroscopy. *Opt Express, 18*(20), 21225-21237.

Guimond, S. E., & Turnbull, J. E. (1999). Fibroblast growth factor receptor signalling is dictated by specific heparan sulphate saccharides. *Curr Biol, 9*(22), 1343-1346.

Harms, G. S., Cognet, L., Lommerse, P. H. M., Blab, G. A., Kahr, H., Gamsjager, R., Spaink, H. P., Soldatov, N. M., Romanin, C., & Schmidt, T. (2001). Single-molecule imaging of L-type Ca2+ channels in live cells. *Biophys. J., 81*, 2639-2646.

Houseman, B. T., Gawalt, E. S., & Mrksich, M. (2003). Maleimide-functionalized self-assembled monolayers for the preparation of peptide and carbohydrate biochips. *Langmuir, 19*(5), 1522-1531.

Iino, R., Koyama, I., & Kusumi, A. (2001). Single molecule imaging of green fluorescent proteins in living cells: E-cadherin forms oligomers on the free cell surface. *Biophys J, 80*(6), 2667-2677.

Itoh, N., & Ornitz, D. M. (2010). Fibroblast growth factors: from molecular evolution to roles in development, metabolism and disease. *J Biochem, 149*(2), 121-130.

Jeong, K. J., Butterfield, K., & Panitch, A. (2008). A novel assay to probe heparin-peptide interactions using pentapeptide-stabilized gold nanoparticles. *Langmuir, 24*(16), 8794-8800.

Jewett, J. C., Sletten, E. M., & Bertozzi, C. R. (2010). Rapid Cu-Free Click Chemistry with Readily Synthesized Biarylazacyclooctynones. *J Am Chem Soc, 132*(11), 3688-+.

Johnsson, N., & Johnsson, K. (2007). Chemical tools for biomolecular imaging. *ACS Chem Biol, 2*(1), 31-38.

Kelly, K. L., Coronado, E., Zhao, L. L., & Schatz, G. C. (2003). The optical properties of metal nanoparticles: The influence of size, shape, and dielectric environment. *J Phys Chem B, 107*(3), 668-677.

Kerszberg, M., & Wolpert, L. (1998). Mechanisms for positional signalling by morphogen transport: a theoretical study. *J Theor Biol, 191*(1), 103-114.

Kinsella, L., Chen, H. L., Smith, J. A., Rudland, P. S., & Fernig, D. G. (1998). Interactions of putative heparin-binding domains of basic fibroblast growth factor and its receptor, FGFR-1, with heparin using synthetic peptides. *Glycoconj J, 15*(4), 419-422.

Kulzer, F., Laurens, N., Besser, J., Schmidt, T., Orrit, M., & Spaink, H. P. (2008). Photothermal detection of individual gold nanoparticles: Perspectives for high-throughput screening. *Chemphyschem, 9*(12), 1761-1766.

Kusumi, A., Sako, Y., & Yamamoto, M. (1993). Confined lateral diffusion of membrane receptors as studied by single particle tracking (nanovid microscopy). Effects of calcium-induced differentiation in cultured epithelial cells. *Biophys J, 65*(5), 2021-2040.

Lander, A. D. (1998). Proteoglycans: master regulators of molrcular encounter. *Matrix Biol, 17*, 465-472.

Lander, A. D. (2007). Morpheus unbound: Reimagining the morphogen gradient. *Cell, 128*(2), 245-256.

Lasne, D., Blab, G., De Giorgi, F., Ichas, F., Lounis, B., & Cognet, L. (2007). Label-free optical imaging of mitochondria in live cells. *Opt Express, 15*(21), 14184-14193.

Lasne, D., Blab, G. A., Berciaud, S., Heine, M., Groc, L., Choquet, D., Cognet, L., & Lounis, B. (2006). Single Nanoparticle Photothermal Tracking (SNaPT) of 5-nm Gold Beads in Live Cells. *Biophys J, 91*(12), 4598-4604.

Leduc, C., Si, S., Gautier, J., Soto-Ribeiro, M., Wehrle-Haller, B., Gautreau, A., Giannone, G., Cognet, L., & Lounis, B. (2013). A Highly Specific Gold Nanoprobe for Live-Cell Single-Molecule Imaging. *Nano Lett, 13*(4), 1489-1494.

Levy, R., Thanh, N. T. K., Doty, R. C., Hussain, I., Nichols, R. J., Schiffrin, D. J., Brust, M., & Fernig, D. G. (2004). Rational and combinatorial design of peptide capping Ligands for gold nanoparticles. *J Am Chem Soc, 126*(32), 10076-10084.

Levy, R., Wang, Z. X., Duchesne, L., Doty, R. C., Cooper, A. I., Brust, M., & Fernig, D. G. (2006). A generic approach to monofunctionalized protein-like gold nanoparticles based on immobilized metal ion affinity chromatography. *Chembiochem, 7*(4), 592-594.

Livet, J., Weissman, T. A., Kang, H., Draft, R. W., Lu, J., Bennis, R. A., Sanes, J. R., & Lichtman, J. W. (2007). Transgenic strategies for combinatorial expression of fluorescent proteins in the nervous system. *Nature, 450*(7166), 56-62.

Lloyd, D. R., & Phillips, D. H. (1999). Oxidative DNA damage mediated by copper(II), iron(II) and nickel(II) Fenton reactions: evidence for site-specific mechanisms in the formation of double-strand breaks, 8-hydroxydeoxyguanosine and putative intrastrand cross-links. *Mutat Res-Fund Mol M, 424*(1-2), 23-36.

Lloyd, R. V., Hanna, P. M., & Mason, R. P. (1997). The origin of the hydroxyl radical oxygen in the Fenton reaction. *Free Rad Biol Med, 22*(5), 885-888.

Lu, H. P., Xun, L., & Xie, X. S. (1998). Single-molecule enzymatic dynamics. *Science, 282*, 1877-1882.

Lutz, J. F., & Zarafshani, Z. (2008). Efficient construction of therapeutics, bioconjugates, biomaterials and bioactive surfaces using azide-alkyne "click" chemistry. *Adv Drug Deliver Rev, 60*(9), 958-970.

Lyon, M., Deakin, J. A., & Gallagher, J. T. (1994). Liver heparan sulfate structure. A novel molecular design. *J Biol Chem, 269*(15), 11208-11215.

Maiti, S., Haupts, U., & Webb, W. W. (1997). Fluorescence correlation spectroscopy: diagnostics for sparse molecules. *Proc Natl Acad Sci U S A, 94*(22), 11753-11757.

Maus, L., Spatz, J. P., & Fiammengo, R. (2009). Quantification and Reactivity of Functional Groups in the Ligand Shell of PEGylated Gold Nanoparticles via a Fluorescence-Based Assay. *Langmuir, 25*(14), 7910-7917.

Mie, G. (1908). Articles on the optical characteristics of turbid tubes, especially colloidal metal solutions. *Annalen Der Physik, 25*(3), 377-445.

Moerner, W. E., & Orrit, M. (1999). Illuminating single molecules in condensed matter. *Science, 283*(5408), 1670-1676.

Murphy, K. J., Merry, C. L., Lyon, M., Thompson, J. E., Roberts, I. S., & Gallagher, J. T. (2004). A new model for the domain structure of heparan sulfate based on the novel specificity of K5 lyase. *J Biol Chem, 279*(26), 27239-27245.

Octeau, V., Cognet, L., Duchesne, L., Lasne, D., Schaeffer, N., Fernig, D. G., & Lounis, B. (2009). Photothermal Absorption Correlation Spectroscopy. *ACS Nano, 3*(2), 345-350.

Oh, E., Susumu, K., Blanco-Canosa, J. B., Medintz, I. L., Dawson, P. E., & Mattoussi, H. (2010). Preparation of Stable Maleimide-Functionalized Au Nanoparticles and Their Use in Counting Surface Ligands. *Small, 6*(12), 1273-1278.

Ong, S. E., Blagoev, B., Kratchmarova, I., Kristensen, D. B., Steen, H., Pandey, A., & Mann, M. (2002). Stable isotope labeling by amino acids in cell culture, SILAC, as a simple and accurate approach to expression proteomics. *Mol Cell Proteomics, 1*(5), 376-386.

Ori, A., Free, P., Courty, J., Wilkinson, M. C., & Fernig, D. G. (2009). Identification of heparin-binding sites in proteins by selective labeling. *Mol Cell Proteomics, 8*(10), 2256-2265.

Ori, A., Wilkinson, M. C., & Fernig, D. G. (2008). The heparanome and regulation of cell function: structures, functions and challenges. *Front Biosci, 13*, 4309-4338.

Ori, A., Wilkinson, M. C., & Fernig, D. G. (2011). A systems biology approach for the investigation of the heparin/heparan sulfate interactome. *J Biol Chem, 286*(22), 19892-19904.

Ornitz, D. M. (2000). FGFs, heparan sulfate and FGFRs: complex interactions essential for development. *Bioessays, 22*(2), 108-112.

Ornitz, D. M., Xu, J., Colvin, J. S., McEwen, D. G., MacArthur, C. A., Coulier, F., Gao, G., & Goldfarb, M. (1996). Receptor specificity of the fibroblast growth factor family. *J Biol Chem, 271*(25), 15292-15297.

Ornitz, D. M., Yayon, A., Flanagan, J. G., Svahn, C. M., Levi, E., & Leder, P. (1992). Heparin is required for cell-free binding of basic fibroblast growth factor to a soluble receptor and for mitogenesis in whole cells. *Mol Cell Biol, 12*(1), 240-247.

Ostrovsky, O., Berman, B., Gallagher, J., Mulloy, B., Fernig, D. G., Delehedde, M., & Ron, D. (2002). Differential effects of heparin saccharides on the formation of specific fibroblast growth factor (FGF) and FGF receptor complexes. *J Biol Chem, 277*(4), 2444-2453.

Pantoliano, M. W., Horlick, R. A., Springer, B. A., Vandyk, D. E., Tobery, T., Wetmore, D. R., Lear, J. D., Nahapetian, A. T., Bradley, J. D., & Sisk, W. P. (1994). Multivalent ligand-receptor binding interactions in the fibroblast growth factor system produce a cooperative growth factor and heparin mechanism for receptor dimerization. *Biochemistry, 33*, 10229-10248.

Parak, W. J., Pellegrino, T., & Plank, C. (2005). Labelling of cells with quantum dots. *Nanotechnology, 16*(2), R9-R25.

Paulo, P. M. R., Gaiduk, A., Kulzer, F., Krens, S. F. G., Spaink, H. P., Schmidt, T., & Orrit, M. (2009). Photothermal Correlation Spectroscopy of Gold Nanoparticles in Solution. *J Phys Chem C, 113*(27), 11451-11457.

Peach, R. J., Day, W. A., Ellingsen, P. J., & McGiven, A. R. (1988). Ultrastructural localization of Tamm-Horsfall protein in human kidney using immunogold electron microscopy. *Histochem J, 20*(3), 156-164.

Pellegrini, L., Burke, D. F., von Delft, F., Mulloy, B., & Blundell, T. L. (2000). Crystal structure of Fibroblast growth factor receptor ectodomain bound to ligand and heparin. *Nature*, *407*(6807), 1029-1034.

Polanska, U. M., Fernig, D. G., & Kinnunen, T. (2009). Extracellular interactome of the FGF receptor-ligand system: Complexities and the relative simplicity of the worm. *Dev Dynam, 238*(2), 277-293.

Prescher, J. A., & Bertozzi, C. R. (2005). Chemistry in living systems. *Nat Chem Biol, 1*(1), 13-21.

Presta, M., Maier, J. A., Rusnati, M., & Ragnotti, G. (1989). Basic fibroblast growth factor: production, mitogenic response, and post-receptor signal transduction in cultured normal and transformed fetal bovine aortic endothelial cells. *J Cell Physiol, 141*(3), 517-526.

Proudfoot, A. E., Handel, T. M., Johnson, Z., Lau, E. K., LiWang, P., Clark-Lewis, I., Borlat, F., Wells, T. N., & Kosco-Vilbois, M. H. (2003). Glycosaminoglycan binding and oligomerization are essential for the in vivo activity of certain chemokines. *Proc Natl Acad Sci U S A, 100*(4), 1885-1890.

Radunz, R., Rings, D., Kroy, K., & Cichos, F. (2009). Hot Brownian Particles and Photothermal Correlation Spectroscopy. *J Phys Chem A Lett, 113*, 1674-1677.

Rahmoune, H., Chen, H. L., Gallagher, J. T., Rudland, P. S., & Fernig, D. G. (1998). Interaction of heparan sulfate from mammary cells with acidic fibroblast growth factor (FGF) and basic FGF. Regulation of the activity of basic FGF by high and low affinity binding sites in heparan sulfate. *J Biol Chem, 273*(13), 7303-7310.

Rapraeger, A. C., Krufka, A., & Olwin, B. B. (1991). Requirement of Heparan Sulfate for bFGF-Mediated Fibroblast Growth and Myoblast Differentiation. *Science, 252*, 1705-1708.

Rigler, R., & Mets, U. (1993). Diffusion of Single Molecules through a Gaussian Laser-Beam. *P Soc Photo-Opt Ins, 1921*, 239-248.

Robinson, C. J., Harmer, N. J., Goodger, S. J., Blundell, T. L., & Gallagher, J. T. (2005). Cooperative dimerization of fibroblast growth factor 1 (FGF1) upon a single heparin saccharide may drive the formation of 2 : 2 : 1 FGF1 center dot FGFR2c center dot heparin ternary complexes. *J Biol Chem, 280*(51), 42274-42282.

Rossier, O., Octeau, V., Sibarita, J. B., Leduc, C., Tessier, B., Nair, D., Gatterdam, V., Destaing, O., Albiges-Rizo, C., Tampe, R., Cognet, L., Choquet, D., Lounis, B., & Giannone, G. (2012). Integrins beta(1) and beta(3) exhibit distinct dynamic nanoscale organizations inside focal adhesions. *Nat Cell Biol, 14*, 1057-+.

Rudland, P. S., Twiston Davies, A. C., & Tsao, S. W. (1984). Rat mammary preadipocytes in culture produce a trophic agent for mammary epithelia-prostaglandin E2. *J Cell Physiol, 120*, 364-376.

Ruoslahti, E., & Yamaguchi, Y. (1991). Proteoglycans as modulators of growth factor activities. *Cell, 64*(5), 867-869.

Ruttinger, S., Buschmann, V., Kramer, B., Erdmann, R., Macdonald, R., & Koberling, F. (2007). Determination of the confocal volume for quantitative fluorescence correlation spectroscopy - art. no. 66300D. *Confocal, Multiphoton, and Nonlinear Microscopic Imaging III, 6630*, D6300-D6300.

Sagar, D. M., Aoudjane, S., Gaudet, M., Aeppli, G., & Dalby, P. A. (2013). Optically induced thermal gradients for protein characterization in nanolitre-scale samples in microfluidic devices. *Sci Rep, 3*, 2130.

Sako, Y., & Kusumi, A. (1994). Compartmentalized structure of the plasma membrane for receptor movements as revealed by a nanometer-level motion analysis. *J Cell Biol, 125*(6), 1251-1264.

Sako, Y., Minoghchi, S., & Yanagida, T. (2000). Single-molecule imaging of EGFR signalling on the surface of living cells. *Nat Cell Biol, 2*(3), 168-172.

Saxena, K., Schieborr, U., Anderka, O., Duchardt-Ferner, E., Elshorst, B., Gande, S. L., Janzon, J., Kudlinzki, D., Sreeramulu, S., Dreyer, M. K., Wendt, K. U., Herbert, C., Duchaussoy, P., Bianciotto, M., Driguez, P. A., Lassalle, G., Savi, P., Mohammadi, M., Bono, F., & Schwalbe, H. (2010). Influence of heparin mimetics on assembly of the FGF.FGFR4 signaling complex. *J Biol Chem, 285*(34), 26628-26640.

Schutz, G. J., Kada, G., Pastushenko, V. P., & Schindler, H. (2000). Properties of lipid microdomains in a muscle cell membrane visualized by single molecule microscopy. *Embo J., 19*(5), 892-901.

Seisenberger, G., Ried, M. U., Endress, T., Buning, H., Hallek, M., & Brauchle, C. (2001). Real-time single-molecule imaging of the infection pathway of an adeno-associated virus. *Science, 294*, 1929-1932.

Selmke, M., Braun, M., & Cichos, F. (2012a). Nano-lens diffraction around a single heated nano particle. *Opt Express, 20*(7), 8055-8070.

Selmke, M., Braun, M., & Cichos, F. (2012b). Photothermal single-particle microscopy: detection of a nanolens. *ACS Nano, 6*(3), 2741-2749.

Selmke, M., Schachoff, R., Braun, M., & Cichos, F. (2013). Twin-focus photothermal correlation spectroscopy. *Rsc Advances, 3*(2), 394-400.

Serls, A. E., Doherty, S., Parvatiyar, P., Wells, J. M., & Deutsch, G. H. (2005). Different thresholds of fibroblast growth factors pattern the ventral foregut into liver and lung. *Development, 132*(1), 35-47.

Sher, I., Weizman, A., Lubinsky-Mink, S., Lang, T., Adir, N., Schomburg, D., & Ron, D. (1999). Mutations uncouple human fibroblast growth factor (FGF)-7 biological activity and receptor binding and support broad specificity in the secondary receptor binding site of FGFs. *J Biol Chem, 274*, 35016-35022.

Shimizu, K., Neuhauser, R., Leatherdale, C., Empedocles, S., Woo, W., & Bawendi, M. (2001). Blinking statistics in single semiconductor nanocrystal quantum dots. *Phys Rev B, 63*(20).

Skidmore, M. A., Dumax-Vorzet, A. F., Guimond, S. E., Rudd, T. R., Edwards, E. A., Turnbull, J. E., Craig, A. G., & Yates, E. A. (2008a). Disruption of rosetting in Plasmodium falciparum malaria with chemically modified heparin and low molecular weight derivatives possessing reduced anticoagulant and other serine protease inhibition activities. *J Med Chem, 51*(5), 1453-1458.

Skidmore, M. A., Guimond, S. E., Rudd, T. R., Fernig, D. G., Turnbull, J. E., & Yates, E. A. (2008b). The Activities of Heparan Sulfate and its Analogue Heparin are Dictated by Biosynthesis, Sequence, and Conformation. *Connect Tissue Res, 49*(3-4), 140-144.

Smith, J. A., Winslow, D. P., & Rudland, P. S. (1984). Different growth factors stimulate cell division of rat mammary epithelial, myoepithelial and stromal cell lines in culture. *J Cell Physiol, 119*, 120-126.

Special issue. (1999). *Science, 283*.

Thompson, S. M., Connell, M. G., van Kuppevelt, T. H., Xu, R., Turnbull, J. E., Losty, P. D., Fernig, D. G., & Jesudason, E. C. (2011). Structure and epitope distribution of heparan sulfate is disrupted in experimental lung hypoplasia: a glycobiological epigenetic cause for malformation? *Bmc Dev Biol, 11*, 38.

Thompson, S. M., Fernig, D. G., Jesudason, E. C., Losty, P. D., van de Westerlo, E. M., van Kuppevelt, T. H., & Turnbull, J. E. (2009). Heparan sulfate phage display antibodies identify distinct epitopes with complex binding characteristics: insights into protein binding specificities. *J Biol Chem, 284*(51), 35621-35631.

Thompson, S. M., Jesudason, E. C., Turnbull, J. E., & Fernig, D. G. (2010). Heparan sulfate in lung morphogenesis: The elephant in the room. *Birth Defects Res, Part C, 90*(1), 32-44.

Tokeshi, M., Uchida, M., Hibara, A., Sawada, T., & Kitamori, T. (2001). Determination of subyoctomole amounts of nonfluorescent molecules using a thermal lens microscope: subsingle-molecule determination. *Anal Chem, 73*(9), 2112-2116.

Uniewicz, K. A., Ori, A., Xu, R., Ahmed, Y., Wilkinson, M. C., Fernig, D. G., & Yates, E. A. (2010). Differential scanning fluorimetry measurement of protein stability changes upon binding to glycosaminoglycans: a screening test for binding specificity. *Anal Chem, 82*, 3796-3802.

Velinov, T. (1995). On Analsysis of Signals from a Photothermal Microscope. *Meas Sci Technol, 6*(1), 28-32.

Vemuri, S., Beylin, I., Sluzky, V., Stratton, P., Eberlein, G., & Wang, Y. J. (1994). The stability of bFGF against thermal denaturation. *J Pharm Pharmacol, 46*(6), 481-486.

Vlodavsky, I., Bar-Shavit, R., Ishai-Michaeli, R., Bashkin, P., & Fuks, Z. (1991). Extracellular sequestration and release of fibroblast growth factor: a regulatory mechanism? *Trends Biochem Sci, 16*(7), 268-271.

Volkin, D. B., & Klibanov, A. M. (1987). Thermal destruction processes in proteins involving cystine residues. *J Biol Chem, 262*(7), 2945-2950.

Waugh, D. S. (2005). Making the most of affinity tags. *Trends Biotechnol, 23*(6), 316-320.

Wilson, Katie (2012) Development of ultra-stable nanomaterials for biological imaging applications. *Doctoral thesis, University of Liverpool*.

Wuelfing, W. P., Gross, S. M., Miles, D. T., & Murray, R. W. (1998). Nanometer gold clusters protected by surface-bound monolayers of thiolated poly (ethylene glycol) polymer electrolyte. *J Am Chem Sci, 120*(48), 12696-12697.

Xie, X. S., Choi, P. J., Li, G. W., Lee, N. K., & Lia, G. (2008). Single-molecule approach to molecular biology in living bacterial cells. *Annu Rev Biophys, 37*, 417-444.

Xu, R., Ori, A., Rudd, T. R., Uniewicz, K. A., Ahmed, Y. A., Guimond, S. E., Skidmore, M. A., Siligardi, G., Yates, E. A., & Fernig, D. G. (2012). Diversification of the structural determinants of fibroblast growth factor-heparin interactions: implications for binding specificity. *J Biol Chem, 287*(47), 40061-40073.

Xu, R., Rudd, T. R., Hughes, A. J., Siligardi, G., Fernig, D. G., & Yates, E. A. (2013). Analysis of the fibroblast growth factor receptor (FGFR) signalling network with heparin as coreceptor: evidence for the expansion of the core FGFR signalling network. *FEBS J, 280*(10), 2260-2270.

Yabe, T., Hosoda-Yabe, R., Kanamaru, Y., & Kiso, M. (2011). A Peptide Found by Phage Display Discriminates a Specific Structure of a Trisaccharide in Heparin. *J Biol Chem, 286*(14).

Yayon, A., Klagsbrun, M., Esko, J. D., Leder, P., & Ornitz, D. M. (1991). Cell surface, heparin-like molecules are required for binding of basic fibroblast growth factor to its high affinity receptor. *Cell, 64*(4), 841-848.

Yu, S. R., Burkhardt, M., Nowak, M., Ries, J., Petrášek, Z., Scholpp, S., Schwille, P., & Brand, M. (2009). Fgf8 morphogen gradient forms by a source-sink mechanism with freely diffusing molecules. *Nature, 461*(7263), 533-536.

Zhang, X. (2006). Receptor Specificity of the Fibroblast Growth Factor Family: THE COMPLETE MAMMALIAN FGF FAMILY. *J Biol Chem, 281*(23), 15694-15700.

Zhang, X., Ibrahimi, O. A., Olsen, S. K., Umemori, H., Mohammadi, M., & Ornitz, D. M. (2006). Receptor specificity of the fibroblast growth factor family. The complete mammalian FGF family. *J Biol Chem, 281*(23), 15694-15700.

Zhu, H., Duchesne, L., Rudland, P. S., & Fernig, D. G. (2010). The heparan sulfate co-receptor and the concentration of fibroblast growth factor-2 independently elicit different signalling patterns from the fibroblast growth factor receptor. *Cell Comm Signal, 8*(1), 14.

Zhu, J., Kell, A. J., & Workentin, M. S. (2006). A retro-Diels-Alder reaction to uncover maleimide-modified surfaces on monolayer-protected nanoparticles for reversible covalent assembly. *Org Lett, 8*(22), 4993-4996.